5

A two-dimensional multibody model of the human knee joint

The knee is the largest and one of the most complex synovial joint in the human body. It is comprised of many elements including articular cartilage, menisci, muscles and ligaments, which are capable of bearing and transferring load during daily activities. The knee joint bears a majority of body weight, and, hence, is quite susceptible to trauma and overuse injuries (Hirokawa, 1993; McGinty *et al.*, 2000). Mechanical loading, particularly dynamic loading, is believed to play a major role in the development and progression of knee joint Osteoarthritis (OA), which is characterized by cartilage degeneration (Tetsworth and Paley, 1994). Motion and loads are also important in artificial knees, influencing wear, which can lead to osteolysis and, ultimately, implant failure (Bei and Fregly, 2004). Therefore, knowledge of *in vivo* joint contact forces during dynamic activities would be valuable for preventing and treating joint injuries and for improving the longevity of joint replacements (Lin *et al.*, 2010). While dynamic X-ray imaging advances permit accurate measurement of *in vivo* knee joint motion (Lu *et al.*, 2008), a non-invasive and clinically feasible approach for

experimental measuring *in vivo* knee joint loading does not exist (Lin *et al.*, 2010). Thus, joint contact loads must be predicted by computational models (Lin *et al.*, 2010).

In this Chapter, a two-dimensional multibody model of the knee joint for predicting the articular contact forces is presented. Firstly, the techniques utilized to define the geometric features of the knee joint are depicted. The contact methodologies adopted to develop this model are described. The mathematical formulation utilized to characterize the nonlinear behavior of the ligaments is also expounded. Computational simulations were performed using the proposed knee model, being their results also discussed. A study about the influence of contact modeling features, such as the geometric conformality, the constitutive contact force law and the contact materials, on the dynamic response of the knee joint is also included in this Chapter.

5.1   Multibody knee model

A two-dimensional model of the human knee joint developed under the framework of multibody system dynamics is presented in this Section. Figure 5.1 shows a generic configuration of this system, which consists of two rigid bodies, i and j, that represent femur and tibia, respectively. Body-fixed coordinate frames $\xi\eta$ are attached to each body, while xy-coordinate frame represents the global coordinate system. The femur coordinate system is located at the femoral intercondylar notch and is coincident with the global reference frame. The tibia coordinate system is located at the center of mass of the tibia, with the local ξ-axis directed proximally and η-axis directed posteriorly. The rotation angles of the local frames of bodies i and j are denoted by ϕ_i and ϕ_j, respectively. The absolute coordinates of centers of mass and inertia properties of the femur and tibia are listed in Table 5.1, which are assigned to the segments on values derived for a similar model of a 76 kg, 1.8 m tall male by Yamaguchi (2001).

Table 5.1   Absolute coordinates and inertia properties of the femur and tibia bodies.

Body name	x [mm]	y [mm]	ϕ [rad]	Mass [kg]	Moment of inertia [kg.m^2]
Femur	0.0	0.0	0.0000	7.58	0.126
Tibia	-201.6	-174.9	0.6145	3.75	0.065

In the present work, the femur and tibia are modeled as two contacting bodies, being their dynamics affected by the contact forces. Thus, the equations of motion that govern the dynamic response of this multibody system incorporate these contact forces. The knee joint elements are considered to be rigid and describe a general planar motion

in the sagittal plane. The femur is considered to be stationary, while the tibia does not have any kinematic constraint. The tibia is connected to the femur by four knee ligaments, namely anterior cruciate ligament (ACL), posterior cruciate ligament (PCL), lateral collateral ligament (LCL) and medial collateral ligament (MCL). These ligaments are represented in Figure 5.1.
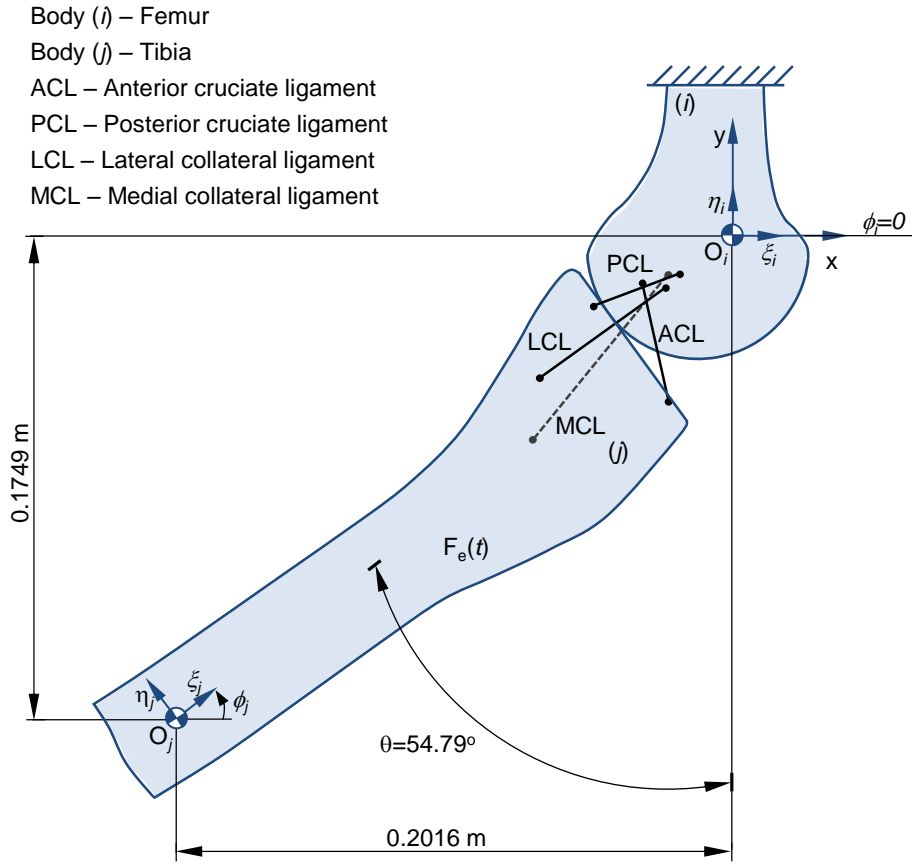

Figure 5.1 Two-dimensional multibody model of the human knee joint.

Since the knee kinematics is not prescribed, a force constraint is to be introduced into the system in order to avoid the separation of the tibia due gravitational action. Thus, an external force is applied at the center-of-mass of the tibia directed proximally, as illustrated in Figure 5.1. The aim of this force is to promote the tibiofemoral contact and also to provide the knee motion on the anterior–posterior direction, from an initial position of 54.79 degrees of flexion to a final position of -5.00 degrees of extension (hyperextension). The external applied force, F_e, is expressed as

$$F_e = Ae^{-4.73\left(\frac{t}{t_d}\right)^2} \sin\left(\frac{\pi t}{t_d}\right) \tag{5.1}$$

which is an exponentially decaying sinusoidal pulsed function with a duration t_d and an amplitude *A* (Machado *et al.*, 2010). The same type of applied external force has been used in computational simulations of other biomechanical models, such as in modeling and simulation of the force of the quadriceps muscle group in knee extension (Moeinzadeh *et al.*, 1983; Abdel-Rahman and Hefzy, 1998) and of human head neck studies (Engin and Akkas, 1978).

5.1.1 Geometric description

With the intent to develop a dynamic model of the human knee joint that allows the performance of contact analysis, it is necessary to accurately define the shapes of the femur and tibia profiles. In this work, a magnetic resonance imaging (MRI) of the knee articulation, online available at the DICOM sample image sets (DICOM, 2009), is utilized to obtain those profiles. Based on this MRI, two sets of points were considered on the articular cartilages of the femur and tibia bones. The outlines were discretized and described in polar coordinates at the selected points, as depicted in Figure 5.2. The points were selected by manual segmentation, 28 from the femur and 18 from the tibia.
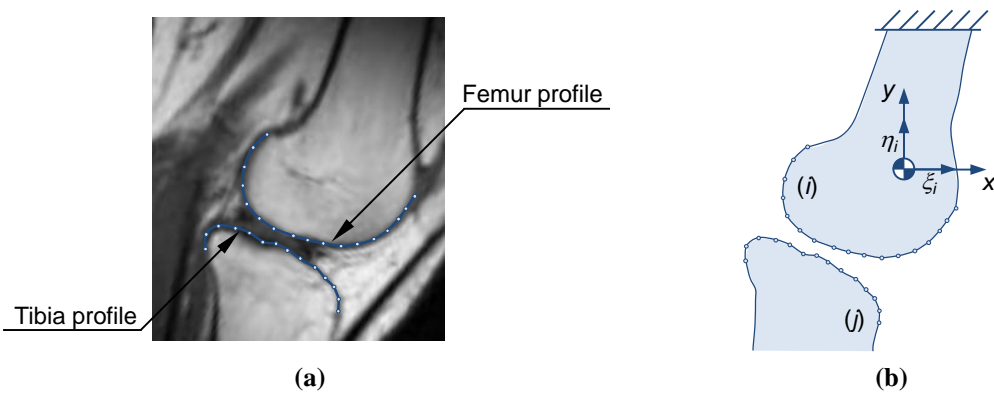

| (a) | (b) |

Figure 5.2   Knee contact profiles within a: (a) MRI at the sagittal plane; (b) Knee joint model.

In order to mathematically describe the geometric outlines of the bodies, the use of curve fitting techniques based on interpolation schemes is required. There are many types of interpolation methods, being popular the Lagrange interpolation and the Hermite interpolation (Chapra and Canale, 1989). The Lagrange interpolation fits a polynomial, with the lowest possible degree, through a set of given points. In turn, the Hermite interpolation forces the interpolant to fit not only the function at each point, but the derivative as well. Therefore, the Hermite approach is employed when smoothness greater than that provided by Lagrange interpolation is required. Nonetheless, some limitations of the Lagrange and Hermite interpolation techniques can be pointed out: (*i*)

these methods can be difficult to compute when the number of data points is large; (*ii*) they are rather inflexible in the measure that adding points requires recomputing everything; (*iii*) the piecewise versions may have discontinuous derivatives at the knots depending on their multiplicity. Hence, these interpolation schemes are useful for deriving numerical methods, but are not appropriate for the type of curve fitting required in this work. As a result, cubic spline interpolation techniques were applied, which consist of polynomial pieces on subintervals joined together according to certain smoothness conditions (Chapra and Canale, 1989; Ferziger, 1998).

A cubic spline interpolating function relies on three fundamentals: (*i*) the curve is piecewise cubic, that is, the coefficients are different on each interval (x_i, x_{i+1}); (*ii*) the curve passes through the given data points; (*iii*) the first and second derivatives are continuous at the node points x_i. Thus, these methods construct curves that consist of polynomial pieces of the same degree and that are of a prescribed overall smoothness. The advantage of this type of interpolating procedures is that they exhibit local geometric control, *i.e.*, the variation of the position of a control point only affects the neighborhood of that point maintaining the rest of the curve unchanged. Their drawback is that they still present some unwanted oscillations in regions where the curve concavity varies (Pombo and Ambrósio, 2008). For a detailed discussion of spline interpolation, the reader is referred to Chapra and Canale (1989) and De Boor (2001).

To address the femur-tibia contact interaction, it is important to develop an effective strategy to determine the accurate location of the contact points on the femur and tibia profiles. The methodology proposed here requires that the profiles be convex or flat curves. Figure 5.3 shows the general configuration of a portion of the contacting bodies, in which the relative distance between them is exaggerated in order to represent all the necessary vectors utilized on the contact detection formulation. Let the contact points on bodies *i* and *j* be represented by P_i and P_j, respectively. It is considered that the segment of curve between points *A* and *B* on bodies *i* and *j* are defined by two cubic spline functions s_i and s_j as

$$s_i = a_3\theta_i^3 + a_2\theta_i^2 + a_1\theta_i + a_0 \tag{5.2}$$

$$s_j = b_3\theta_j^3 + b_2\theta_j^2 + b_1\theta_j + b_0 \tag{5.3}$$

where a_0, a_1, a_2, a_3, b_0, b_1, b_2 and b_3 are the cubic spline polynomial coefficients and θ_i and θ_j represent the polar parameters that define the splines employed (De Boor, 2001). These angles θ_i and θ_j are measured relative to the local ξ-axes, as shown in Figure 5.3.

Figure 5.3   Two contacting bodies, in which the distance between them is exaggerated with the purpose to represent all the necessary vectors.

The first derivative of Equations (5.2) and (5.3) with respect to θ_i and θ_j result

$$\dot{s}_i = 3a_3\theta_i^2 + 2a_2\theta_i + a_1 \tag{5.4}$$

$$\dot{s}_j = 3b_3\theta_j^2 + 2b_2\theta_j + b_1 \tag{5.5}$$

In a similar way, the second derivative of Equations (5.2) and (5.3) yield

$$\ddot{s}_i = 6a_3\theta_i + 2a_2 \tag{5.6}$$

$$\ddot{s}_j = 6b_3\theta_j + 2b_2 \tag{5.7}$$

It is worth noting that with this approach it is ensured that polynomial functions used to define the femur and tibia profiles are continuous for each interval considered.

5.1.2   Contact modeling formulation

The contact detection between freeform profiles consists of a two-step procedure, as described in Chapter 4. The first step comprises the identification of the coordinates of the potential contact points. Thus, the second step consists of calculating the distance

between the potential contact points and evaluating the indentation condition in order to check whether the points are in contact or not (Pombo, 2004). The local coordinates of potential contact points can be expressed in terms of polar coordinates as,

$$\xi_k^P = s_k \cos \theta_k \quad (k = i, j) \tag{5.8}$$

$$\eta_k^P = s_k \sin \theta_k \quad (k = i, j) \tag{5.9}$$

The global position of the potential contact points, $\mathbf{r}_k^P$, can be given by

$$\mathbf{r}_k^P = \mathbf{r}_k + \mathbf{A}_k \mathbf{s}_k'^P \quad (k = i, j) \tag{5.10}$$

where $\mathbf{A}_i$ and $\mathbf{A}_j$ denote the rotational transformation matrices of bodies i and j, $\mathbf{r}_i$ and $\mathbf{r}_j$ are the global coordinates of points O_i and O_j, and $\mathbf{s}_i'^P$ and $\mathbf{s}_j'^P$ are the local components of points P_i and P_j with respect to $\xi\eta$ coordinate system.

The velocities of the potential contact points, P_i and P_j, expressed in terms of the global coordinate system are evaluated by differentiating Equation (5.10) with respect to time, yielding

$$\dot{\mathbf{r}}_k^P = \dot{\mathbf{r}}_k + \dot{\mathbf{A}}_k \mathbf{s}_k'^P \quad (k = i, j) \tag{5.11}$$

The relative normal and tangential velocities are determined by projecting the relative contact velocities onto the respective directions

$$v_N = \left(\dot{\mathbf{r}}_i^P - \dot{\mathbf{r}}_j^P \right)^T \mathbf{n} \tag{5.12}$$

$$v_T = \left(\dot{\mathbf{r}}_i^P - \dot{\mathbf{r}}_j^P \right)^T \mathbf{t} \tag{5.13}$$

where $\mathbf{n}$ is the normal vector to the direction of contact and $\mathbf{t}$ is the tangential vector obtained by rotating vector $\mathbf{n}$ by 90° clockwise direction, as shown in Figure 5.3. Since the contacting bodies have been defined by polynomial functions, the first problem that arises is the accurate prediction of the location of the potential contact points. This problem has to be solved at every time step during the dynamic analysis.

From Figure 5.3, it can be observed that the distance between the potential contact points on bodies i and j is given by vector $\mathbf{d}$, and can be written as

$$\mathbf{d} = \mathbf{r}_i + \mathbf{A}_i \mathbf{s}_i'^P - \mathbf{r}_j - \mathbf{A}_j \mathbf{s}_j'^P \tag{5.14}$$

The first geometric condition, commonly known as proximity query, for contact between points P_i and P_j is that the vector $\mathbf{d}$ corresponds to the minimum distance. Another geometric contact condition is that the vector $\mathbf{d}$ and normal vectors of the curves, $\mathbf{n}_i$ and $\mathbf{n}_j$, have to be collinear. The first derivatives of Equations (5.8) and (5.9), which correspond to the local coordinates of potential contact points with respect to θ_i and θ_j, give the local components of the tangent vectors to the curves s_i and s_j at points P_i and P_j, respectively, as illustrated in Figure 5.3. Therefore, these tangent vectors can be expressed in local coordinates as

$$\mathbf{t}_i^P = \left\{ \frac{d\xi_i^P}{d\theta_i} \quad \frac{d\eta_i^P}{d\theta_i} \right\}^T \tag{5.15}$$

$$\mathbf{t}_j^P = \left\{ \frac{d\xi_j^P}{d\theta_j} \quad \frac{d\eta_j^P}{d\theta_j} \right\}^T \tag{5.16}$$

For points P_i and P_j, the normal vectors can be expressed in local coordinates as

$$\mathbf{n}_i^P = \left\{ \frac{d\eta_i^P}{d\theta_i} \quad -\frac{d\xi_i^P}{d\theta_i} \right\}^T \tag{5.17}$$

$$\mathbf{n}_j^P = \left\{ \frac{d\eta_j^P}{d\theta_j} \quad -\frac{d\xi_j^P}{d\theta_j} \right\}^T \tag{5.18}$$

The tangent and normal vectors can be easily expressed in the global form by multiplying the local coordinates, given by Equations (5.15) - (5.18), by the respective rotational transformation matrix. Figure 5.4 illustrates the two possible scenarios that may occur in the contact problem: (*i*) contact at a single point without indentation, and (*ii*) contact at a multiple points with indentation.

(a)   **(b)**

Figure 5.4   Two possible contact scenarios: (a) Contact at a single point without indentation; (b) Contact at a multiple points with indentation.

The minimum distance condition given by (5.14) is not enough to find the possible contact points between the two contact profiles, since it does not cover all contact scenarios, as Figure 5.4 shows. Therefore, the contact points are defined as those that correspond to maximum indentation, *i.e.*, the points of maximum elastic deformation, measured along the normal direction. The geometric condition equations for contact rely on the common-normal concept and are defined as

(*i*)   The distance between the potential contact points, P_i and P_j, given by vector **d** corresponds to the minimum distance;

(*ii*)   The vector **d** has to be collinear with the normal vector $\mathbf{n}_i$;

(*iii*) The normal vectors $\mathbf{n}_i$ and $\mathbf{n}_j$ at the potential contact points, P_i and P_j, have to be collinear, which means that $\mathbf{n}_j$ has null projection onto the tangent vector $\mathbf{t}_i$.

Conditions (*ii*) and (*iii*) can be written as

$$\mathbf{n}_i \times \mathbf{n}_j = 0 \quad \text{or} \quad \mathbf{n}_j^T \mathbf{t}_i = 0 \tag{5.19}$$

$$\mathbf{d} \times \mathbf{n}_i = 0 \quad \text{or} \quad \mathbf{d}^T \mathbf{t}_i = 0 \tag{5.20}$$

The geometric conditions given by Equations (5.19) and (5.20) are two nonlinear equations with two unknowns, namely the two profile curve parameters θ_i and θ_j, which can be solved using a Newton-Raphson iterative procedure. These equations provide the solution for the location of the potential contact points. Once the potential contact points are found, the next step is the evaluation of the contact indentation given by

$$d = \sqrt{\mathbf{d}^T \mathbf{d}} \tag{5.21}$$

The indentation condition states that the contact between the profiles of the bodies exists and, the potential contact points are real contact points when the following relation is verified

$$\mathbf{d}^T \mathbf{n}_j \leq 0 \tag{5.22}$$

By introducing the curve parameters that describe the geometry of the contact profiles, the components of the contact points can be predicted during the dynamic

analysis. Since the profiles of the bodies have complex geometries, the position of the contact points cannot be predicted *a priori*. Therefore, during simulations, the calculation of the curve parameters requires the solution of a preliminary system of nonlinear equations. The computational implementation of this methodology is quite efficient since the information of the previous time step is used as initial guess or estimate to find the solution of the nonlinear Equations (5.19) and (5.20).

When a contact is detected, a continuous contact force law is applied which allow for the calculation of the contact forces developed at the interface as a function of the relative indentation between the two contacting bodies. The external applied force F_e and the forces produced in the ligaments, together with the contact forces, are introduced into the system equations of motion as external generalized forces. The proposed contact methodology is implemented in a computational algorithm, presented in Figure 5.5. This computational algorithm, developed under the framework of multibody system dynamics, can be summarized as

1. Start at instant of time t^0 with given initial conditions for positions $\mathbf{q}^0$ and velocities $\dot{\mathbf{q}}^0$;
2. Define initial guess for the curve parameters θ_i and θ_j of the contacting outlines;
3. Solve a system of nonlinear equations to obtain the curve parameters that define the components of the potential contact points, P_i and P_j;
4. Compute the local coordinates of the potential contact points, P_i and P_j;
5. Check for contact. If there is contact, evaluate the contact forces;
6. Add the contact forces to the generalized force vector of the equations of motion;
7. Obtain the new generalized positions and velocities of the system for time step $t + \Delta t$;
8. Update the system time variable;
9. Go to step 3 and proceed with the whole process for the new time step, until the final time for the analysis is reached.
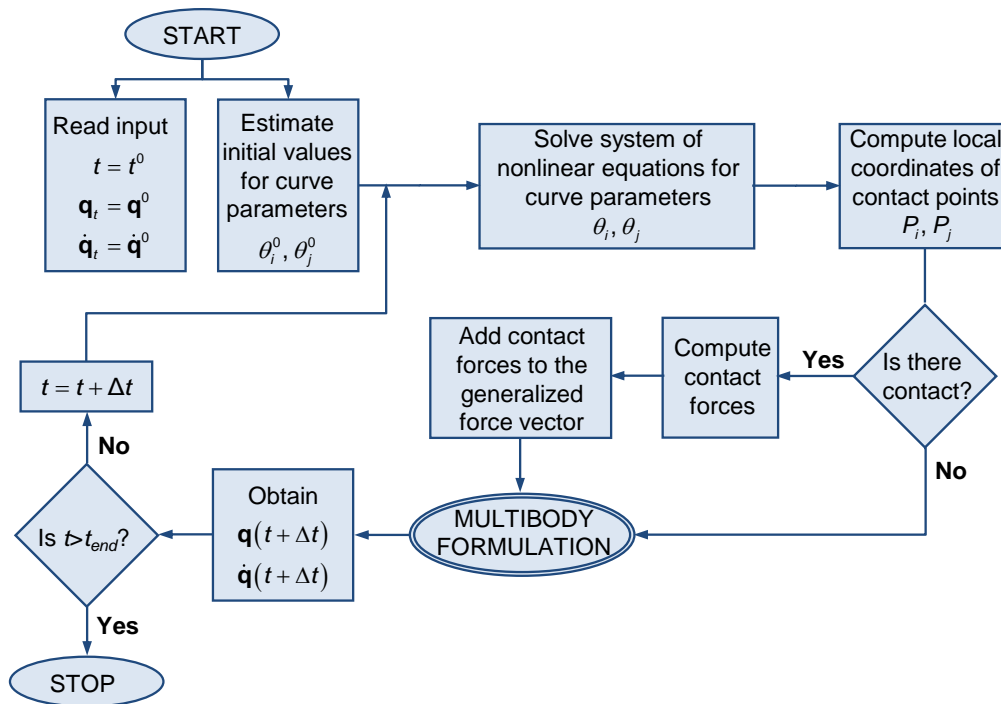
Figure 5.5 Flowchart of the developed algorithm for contact dynamics of planar multibody systems, which was implemented in a multibody code named MUBODYNA (Flores, 2010).

It should be noted that the identification of the contact point at the time that the indentation is null is of importance. Numerically, the control of the time step that ensures the identification of the time of contact for which an acceptable indentation is verified is fundamental. For a practical discussion of this issue, which is taken into account in this work, see the reference by Flores and Ambrósio (2010).

5.1.3   Physical models for ligaments and cartilage

It is known that ligaments are composite and anisotropic structures exhibiting a time-dependent behavior, characteristic of a viscoelastic solid, and are nonlinear in their stress–strain response. The time-dependent behavior means that, during daily activities, ligaments are subjected to a variety of load conditions that influence their physical properties. Thus, ligaments become softer and less resistant after some minutes of running, returning to normal hardness when the exercise is interrupted. The history dependence, in turn, means that frequent intense activities changes the tissue properties in a medium term basis. For example, the ligaments of an athlete, after 6 months of daily training, become softer and thus more adapted to the intense exercise, even when the athlete is not training. Likewise, if the activities are interrupted for some months, the ligament properties go back to normal levels of hardness (Hawkins and Bey, 1997).

A typical stress-strain relation for a general ligament is illustrated in Figure 5.6. This stress-strain curve is typically divided in three different zones, which can be analyzed and understood in terms of microarchitecture of ligament (Butler *et al.*, 1978). Zone I corresponds to the geometric rearrangement of microstructural network, that is, uncoiling of the coiled collagen fibers. At this zone, with initial lengthening of ligamentous tissue, the stress-strain curve is hardening. This portion of the curve is named "toe-in region" and is often described as having the shape of an exponential or polynomial relation (Wismans, 1980; Moeinzadeh, 1981). The elongation reflected at this zone is believed to be the result of a change in the wavy pattern of the relaxed collagen fibers. The tissue stretches easily, without much force, and the collagen fibers become straight and lose their wavy appearance as the loading progresses (Nordin *et al.*, 2001). In zone I, the ligament stiffness is determined mainly by the stiffness of the elastin network. As loading continues, additional fibrils were recruited, being greater force required to produce equivalent amounts of elongation. At higher loads, all the fibrils are loaded and the ligament stress–strain curve becomes linear (Weiss *et al.*, 2005). At this stage, *i.e.*, at the end of the zone I, all collageneous fibers are assumed to be fully uncoiled. In zone II, also called linear region, the stiffness of ligaments is reported to correspond mainly to the stiffness of the collagen fibers and is found to be almost constant. Finally, in zone III, the rupture of some collagen fibers is observed. In this region, at large strains, the stress-strain curve can end abruptly or curve downward as a result of irreversible changes, *i.e.*, a complete failure of the ligament itself (Nordin *et al.*, 2001; Weiss and Gardiner, 2001).
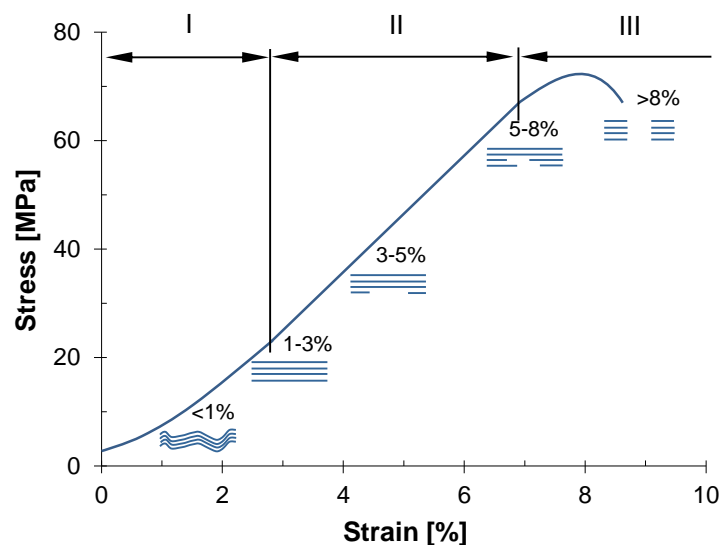

Figure 5.6   Typical ligament stress-strain relationship (Butler *et al.*, 1978).

Crowninshield *et al.* (1976) tested human knee ligaments and observed that a quadratic stress-strain relation is a good approximation for the elastic behavior of the ligaments. Therefore, in the present study, the following quadratic force-elongation relation is considered for each knee ligament

$$F_l = k_l \left(l - l^0 \right)^2, \qquad \text{if } l > l^0 \tag{5.23}$$

where k_l is the ligament stiffness, l and l^0 are the actual and the unstrained lengths of the ligament, respectively (Moeinzadeh *et al.*, 1983; Abdel-Rahman and Hefzy, 1993; Engin and Tumer, 1993; Abdel-Rahman and Hefzy, 1998). Furthermore, it is assumed that ligaments cannot carry any compressive force, that is,

$$F_l = 0, \qquad \text{if } l \leq l^0 \tag{5.24}$$

The direction of the force exerted by ligament on the articulating body coincides with the direction of the line segment through the insertion points of the ligaments. These insertion points represent the end points of the ligaments and are connected to the femur and tibia articular surfaces. The distance between the insertion points defines the length of the ligament. All ligaments carry force if their actual lengths are longer than their unstrained lengths. The unstrained lengths were determined when femur and tibia are positioned at about 55 degrees of knee flexion, since this value corresponds to a particular position where the ligaments are in a relaxed condition, and therefore the knee contact forces can be neglected (Moeinzadeh *et al.*, 1983). The local coordinates of the ligament insertion points, as well as their physical properties, *i.e.* the unstrained length and stiffness, are listed in Table 5.2. These values are determined from the information available in literature and are similar to a anatomical study of human knee joint (Wismans, 1980; Engin and Tumer, 1993).

Table 5.2 Local coordinates of the insertion points and physical properties of the ligaments.

Ligament	ACL	PCL	MCL	LCL
ξ_f [mm]	-33.0	-19.0	-23.0	-25.0
η_f [mm]	-17.0	-14.0	-14.0	-19.0
ξ_t [mm]	213.0	210.0	163.0	178.0
η_t [mm]	-9.0	35.0	8.0	25.0
l^0 [mm]	43.8	33.2	78.4	56.2
k_l [N/mm^2]	35	30	15	15

In this study, the bone portions of the distal femur and proximal tibia are considered as perfectly rigid, due to their higher stiffness when compared with the hyaline cartilage, which is considered to be a deformable material. The hyaline cartilage is structurally non-homogeneous and presents anisotropic and nonlinear mechanical behavior. However, for sake of simplicity, in the present study, as in other analytical models (Korhonen *et al.*, 2002), the hyaline cartilage is modeled as an homogeneous and isotropic material.

5.2   Global dynamic results

Computational simulations were carried out in order to validate the developed 2D-model of the human knee and the proposed contact methodology. The purely elastic Hertz contact law was applied to compute the normal contact forces, being considered a generalized contact stiffness of 3260513 N/m$^{1.5}$. It is worth noting that this parameter was calculated based on the material properties of the articular cartilage, namely a Young's modulus of 24 MPa and Poisson's ratio of 0.38 (Herman, 2007). In this computational study, the amplitude of external force was set to 50 N. The simulations were performed for 0.4 s of duration with a time step of 1×10^{-4} s. For the contact detection process, the contacting profiles obtained by interpolation were considered.

With the purpose of determining which spline interpolation technique is more appropriate and accurate to define the geometry of contacting profiles, three different interpolation approaches were investigated, namely cubic splines, Akima splines and shape preserving splines. These three spline interpolation methods are available in the IMSL Fortran numerical libraries, being their acronyms, respectively, CSINT, CSAKM and CSCON. The CSAKM and CSCON were selected because they impose the matching of the data and therefore are considered to be appropriate methods to define geometric shapes. The Akima splines (CSAKM) are characterized by attempting to minimize oscillations, being the shape preserving schemes (CSCON) known for preserving the convexity of the data. The CSINT is a simple cubic spline interpolation scheme based on the "not-a-knot" condition that was chosen for sake of comparison with the other two interpolation methods (Akima, 1970; Visual Numerics, 1997; Kvasov, 2000). Figure 5.7 depicts the *xy*-coordinates of the tibia center of mass and the tibia contact points obtained by using each spline interpolation scheme. Other numerical results are plotted in Figure 5.8.
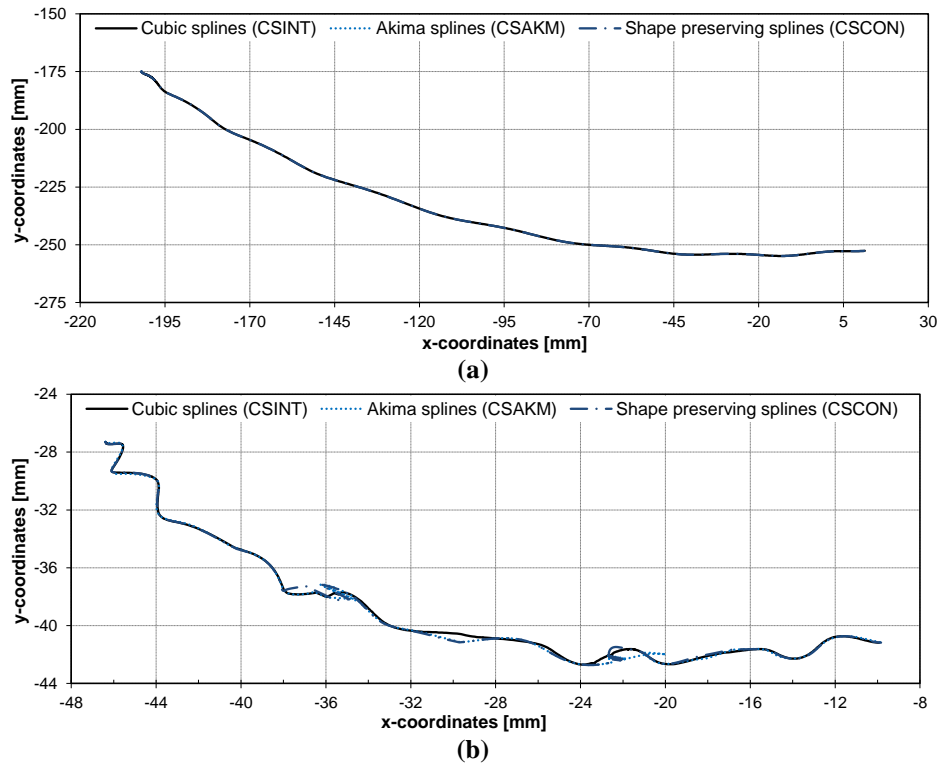
Figure 5.7 *xy*-Coordinates of the Tibia obtained using different spline interpolation techniques: (a) Tibia center of mass; (b) Tibia contact points.
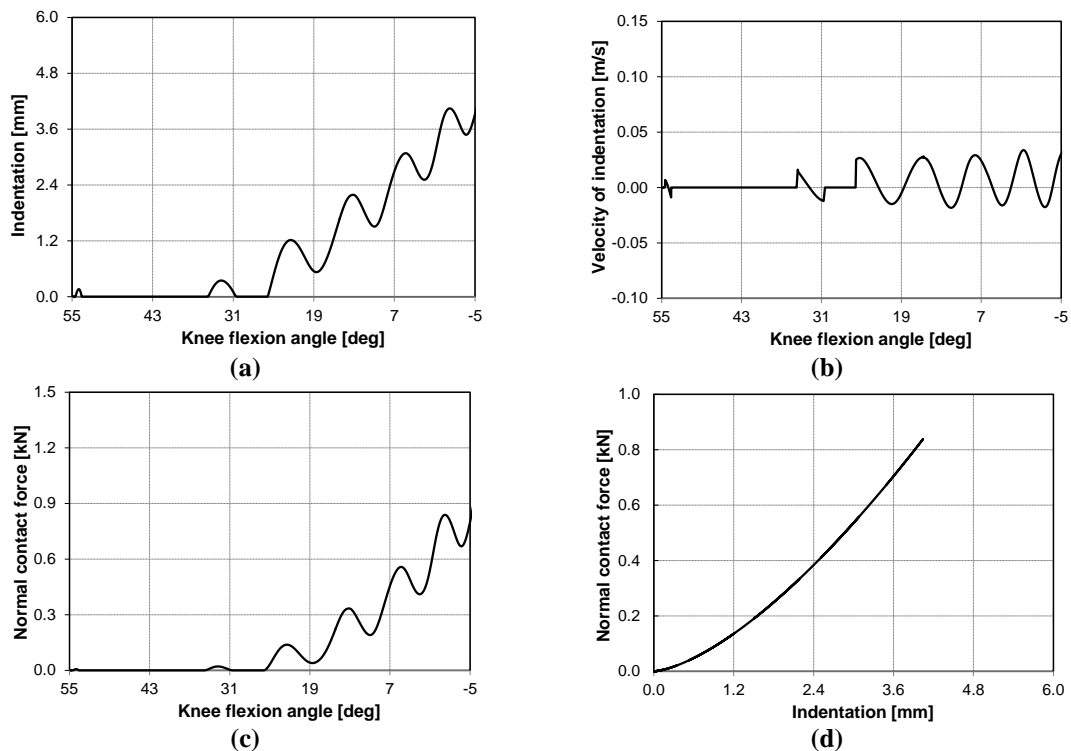

Figure 5.8 Knee contact response using shape preserving splines: (a) Indentation *versus* knee flexion angle; (b) Velocity of indentation *versus* knee flexion angle; (c) Normal contact force *versus* knee flexion angle; (d) Force-indentation relation.

From the analysis of Figure 5.7, it can be observed that the choice for the spline interpolation scheme does not have significant influence on the resulting motion.

However, it is possible that such differences arise when the profile geometries are more complex. According to Pombo and Ambrósio (2008), the shape preserving cubic splines are more appropriate for defining the shape of the body outlines compared with other two interpolating curves, because this approach do not introduce spurious oscillations on the curves and is consistent with the concavity of the data. Based on these observations, the shape preserving splines were selected as interpolation technique for the description of the contacting bodies within the proposed methodology. For more information, the reader is referred to Micchelli *et al.* (1985) and Irvine *et al.* (1986).

The evolution of the relative indentation, velocity of indentation and normal contact forces along the knee flexion angle is reported in Figure 5.8. Moreover, the force-indentation relation is plotted in Figure 5.8d. The curves of the relative indentation and the normal contact force present similar shapes. This is a reliable result since the Hertz law does not take into account the energy dissipation during impact, which strongly depends on impact velocities. Figure 5.8 reveal also the continuous nature of the knee motion in the sense in which the contact indentation of the knee joint after the second impact takes always positive values. This outcome means that from a position of 26 to -5 degrees of flexion, the tibia and the femur are in continuous contact.

5.3   Influence of the geometric conformality

According to Koo and Andriacchi (2007), the femoral condyles present convex curvatures in medial and lateral compartments and the tibial plateaus have concave curvatures in medial compartment and convex curvature in lateral compartment. The MRI images of the human knee joint presented in Figure 5.9 support these observations. Figure 5.9a shows a knee lateral compartment, where it is possible to fit both bones to convex spheres. Figure 5.9b illustrates a knee medial compartment. In this case, the femoral condyle assumes a convex spherical configuration and the tibial plateau is fitted to a concave sphere. Figure 5.9c depicts the knee at the intercondylar notch, where the femur exhibits a convex spherical shape and the tibia is planar.

In order to investigate if the geometric conformality has or not a significant influence on the knee contact problem, particularly in what concerns with the contact detection process, three geometric configurations were considered for dynamic simulations. Since three distinct geometric models are used, different methodologies to

deal with the contact detection have to be also applied. Figure 5.10 shows a representation of each contact scenario.
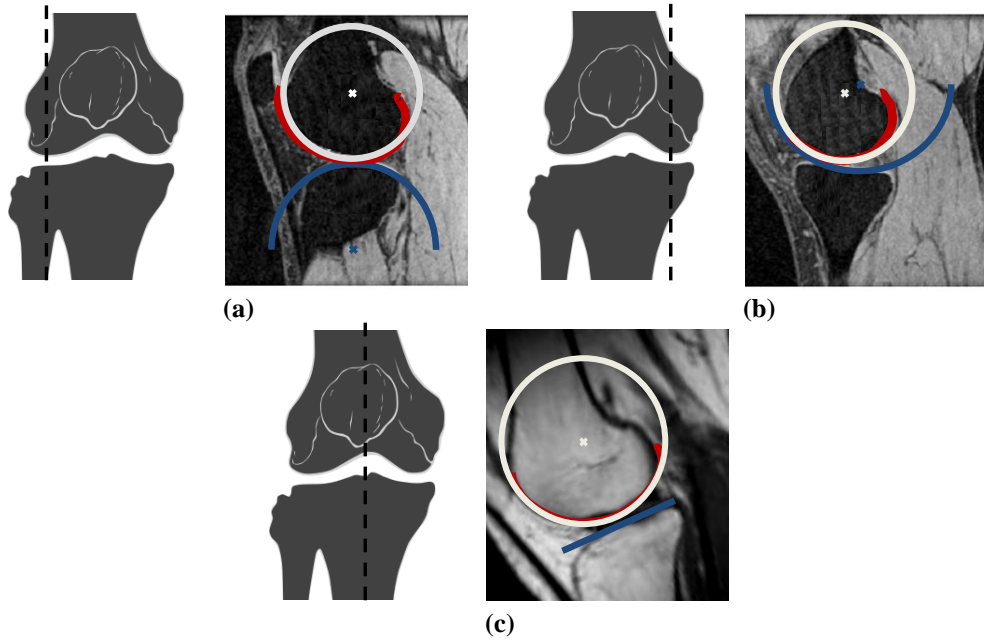

Figure 5.9 Knee MRI images: (a) lateral, (b) medial and (c) intercondylar views {Adapted from Koo *et al.*, (2005) with Elsevier permission}.
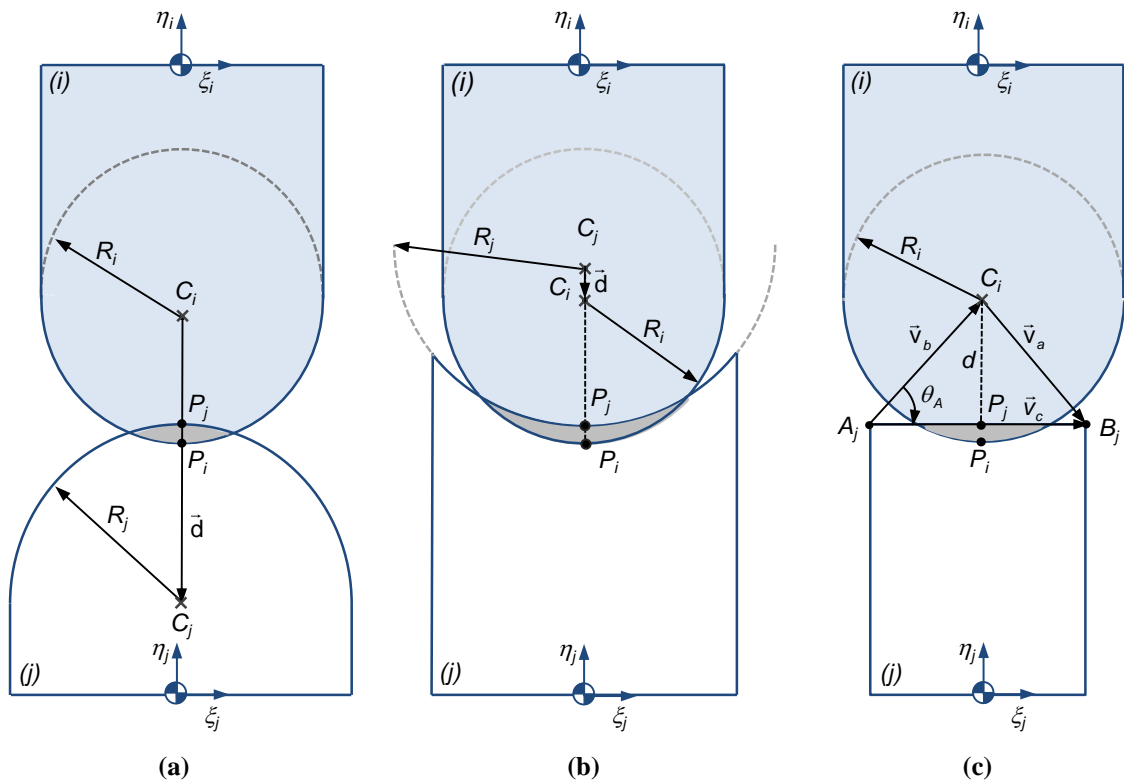

Figure 5.10 Representation of the different contact scenarios: (a) convex-convex spheres, (b) convex-concave spheres and (c) convex sphere-plane.

The computational simulations are performed for 0.4 s of duration with a time step of 1×10^{-4} s, and with an amplitude of external force equal to 50 N. For sake of comparison, the contact forces are evaluated by employing the Hertz contact law. The values of the adopted radii for femur and tibia as well as the generalized stiffness for each contact scenario are listed in Table 5.3.

Table 5.3   Femur (R_i) and tibia (R_j) radii as well as the generalized stiffness parameter (K) used in each contact scenario, namely convex-convex spheres, convex-concave spheres and convex sphere-plane (Martelli *et al.*, 2006; Koo and Andriacchi, 2007).

	Convex-convex spheres	Convex-concave spheres	Convex sphere-plane
R_i [mm]	26.40	30.40	30.40
R_j [mm]	36.02	75.00	∞
K [N/m$^{1.5}$]	2750403	5879434	3260513

In what concerns with the convex-convex spheres model of Figure 5.10a and the convex-concave spheres model of Figure 5.10b, the first step consists of determining the vector **d** that connects the centers of the spheres. Vector **d** for the convex-convex spheres model and the convex-concave spheres model is, respectively, expressed as

$$\mathbf{d} = \mathbf{r}_j^C - \mathbf{r}_i^C \tag{5.25}$$

$$\mathbf{d} = \mathbf{r}_i^C - \mathbf{r}_j^C \tag{5.26}$$

where $\mathbf{r}_i^C$ and $\mathbf{r}_j^C$ are the global coordinate vectors of center points C_i and C_j. For both models, the magnitude of the vector **d** can be computed as

$$d = \sqrt{\mathbf{d}^T \mathbf{d}} \tag{5.27}$$

To check if the bodies are in contact or not, it is necessary to evaluate the indentation condition. For the contact scenario in which the femoral condyle and the tibial plateau are considered as convex spheres, as seen in Figure 5.10a, the indentation condition is expressed as

$$\delta = \begin{cases} 0 & \text{if } d > R_i \\ \left(R_i + R_j \right) - d & \text{if } d \leq \left(R_i + R_j \right) \end{cases} \tag{5.28}$$

For the contact between a spherical convex femoral condyle and a spherical concave tibial plateau (Figure 5.10b), the indentation condition is given by

$$\delta = \begin{cases} 0 & \text{if } d < \left(R_j - R_i \right) \\ d - \left(R_j - R_i \right) & \text{if } d \geq \left(R_j - R_i \right) \end{cases} \qquad (5.29)$$

Regarding to the contact between a spherical femoral condyle and a planar tibial plateau (see Figure 5.10c), the first step of the contact detection procedure deals with the evaluation of the minimal distance between the bodies. Since the location of the points A_j, B_j and C_i is known, the vectors $\mathbf{v_b}$ and $\mathbf{v_c}$ can be defined, as well as the angle θ_A between these two vectors. Thus, the distance between the plane and the center of the sphere can be given by

$$d = v_b \sin \theta_A \qquad (5.30)$$

The second and last step is to check if the bodies are in contact by evaluating the indentation δ by

$$\delta = \begin{cases} 0 & \text{if} \quad d > R_i \\ R_i - d & \text{if} \quad d \leq R_i \end{cases} \qquad (5.31)$$

The results obtained are reported in Figures 5.11 and 5.12. Figure 5.11 depicts the evolution of the contact indentation and forces along the knee extension. Figure 5.12 presents the force-indentation relations for the first impact and for the whole simulation (*i.e.* from an initial position of 55 degrees flexion to a final pose of hyperextension).

(a)   **(b)**
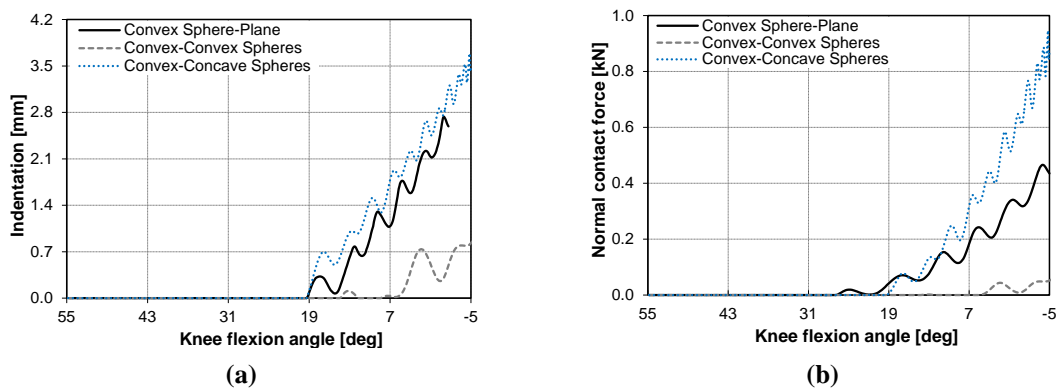
Figure 5.11 (a) Indentation *versus* knee flexion angle using three different geometric models; (b) Normal contact force *versus* knee flexion angle using three different geometric models.
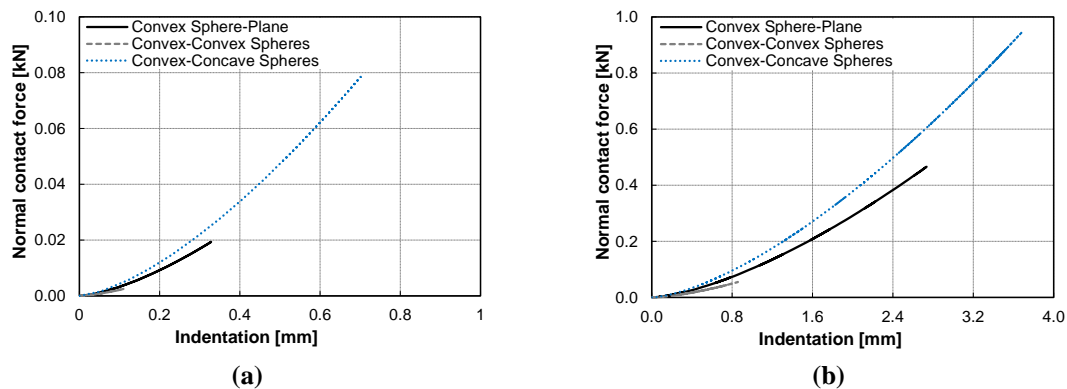
Figure 5.12 Normal contact force *versus* indentation using three different geometric models: (a) First impact; (b) Whole simulation.

Analyzing Figures 5.11 and 5.12, it can be observed that the conformality of the contacting bodies has a significant influence on the global contact results, namely in terms of indentation and, hence, on the contact force. Figure 5.12 depicts that the convex-concave spheres model exhibits the highest level of indentation and contact force. This observation can be explained by the dynamic nature of the formulation used in this work, in which the contact force is an explicit function of the system configuration and the contact properties. In particular, the higher radius of the medial femur ($R_i = 30.4$ mm) compared with the radius of the lateral femur ($R_i = 22.0$ mm) also contribute for this result. This outcome is also visible in Figure 5.12, where the highest and the lowest slopes of the force-indentation relations correspond to the convex-concave spheres and convex-convex spheres models, respectively. These results can help to understand the major incidence of OA at the medial compartment of the knee joint, which exhibits a conformal contact scenario in the anterior-posterior direction (Koo and Andriacchi, 2007). It should be highlighted that other relevant parameters, neglected in the present study, may also contribute to the knee OA evolution, such as menisci and muscles. In addition, the general gait parameters (stride length, cadence, etc.) and daily activities, such as labour tasks and sport practice, can also influence the knee joint dynamic response (Andriacchi and Dyrby, 2005).

In brief, the influence of the geometrical configuration of the contacting bodies on the dynamics of the knee joint system is depicted and the importance of the use of an appropriate geometrical representation to describe the contacting bodies is confirmed. However, it is not possible to elect the geometrical configuration that best fits the tibiofemoral joint, because it depends on the application purposes. Nevertheless, this study served to highlight the significance of geometrical configuration of the tibia and the femur on the contact dynamics of the knee joint.

5.4   Influence of the constitutive contact force law

With the intention to assess the influence of the contact force law on the dynamic response of the knee joint model, computational simulations were performed using different contact force laws, which are listed in Table 5.4. Figures 5.13 and 5.14 depict the contact indentations and forces as a function of the knee flexion angle for the first impact and for the whole simulation, respectively. The force-indentation relations for the first impact and for the whole simulation are plotted in Figure 5.15.

Table 5.4   Some contact force laws and its correspondent mathematical expressions.

Authors	Expression
Hertz (1881)	$F_N = K\delta^n$
Hunt and Crossley (1975)	$F_N = K\delta^n \left[1 + \dfrac{3(1-c_r)}{2} \dfrac{\dot{\delta}}{\dot{\delta}^{(-)}} \right]$
Herbert and McWhannell (1977)	$F_N = K\delta^n \left[1 + \dfrac{6(1-c_r)}{[(2c_r-1)^2+3]} \dfrac{\dot{\delta}}{\dot{\delta}^{(-)}} \right]$
Lee and Wang (1983)	$F_N = K\delta^n \left[1 + \dfrac{3(1-c_r)}{4} \dfrac{\dot{\delta}}{\dot{\delta}^{(-)}} \right]$
Lankarani and Nikravesh (1990)	$F_N = K\delta^n \left[1 + \dfrac{3(1-c_r^2)}{4} \dfrac{\dot{\delta}}{\dot{\delta}^{(-)}} \right]$
Gonthier *et al.* (2004)	$F_N = K\delta^n \left[1 + \dfrac{1-c_r^2}{c_r} \dfrac{\dot{\delta}}{\dot{\delta}^{(-)}} \right]$
Zhiying and Qishao (2006)	$F_N = K\delta^n \left[1 + \dfrac{3(1-c_r^2)e^{2(1-c_r)}}{4} \dfrac{\dot{\delta}}{\dot{\delta}^{(-)}} \right]$
Flores *et al.* (2011)	$F_N = K\delta^n \left[1 + \dfrac{8(1-c_r)}{5c_r} \dfrac{\dot{\delta}}{\dot{\delta}^{(-)}} \right]$
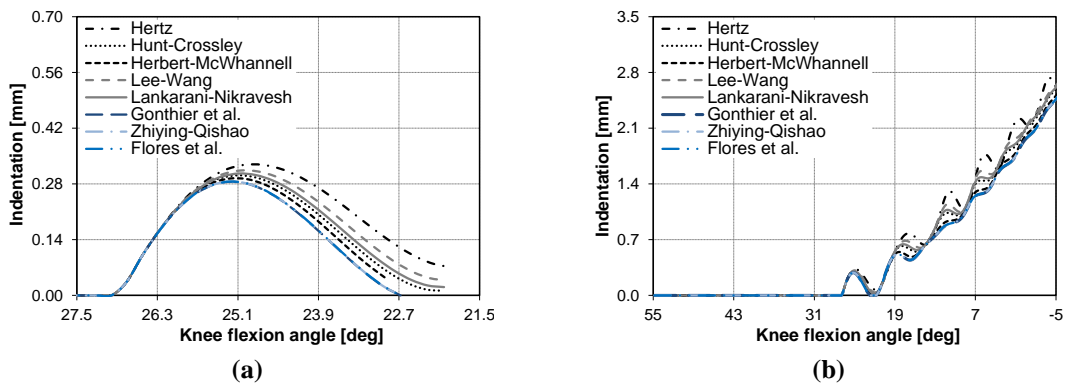
Figure 5.13 Indentation *versus* knee flexion angle of a healthy knee model analyzed by different contact force laws: (a) First impact; (b) Whole simulation.
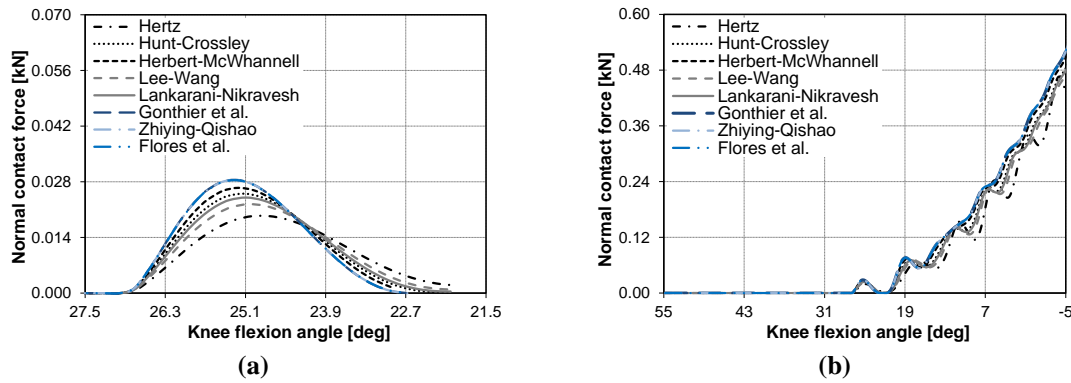
Figure 5.14 Normal contact force *versus* knee flexion angle of a healthy knee model analyzed by different contact force laws: (a) First impact; (b) Whole simulation.
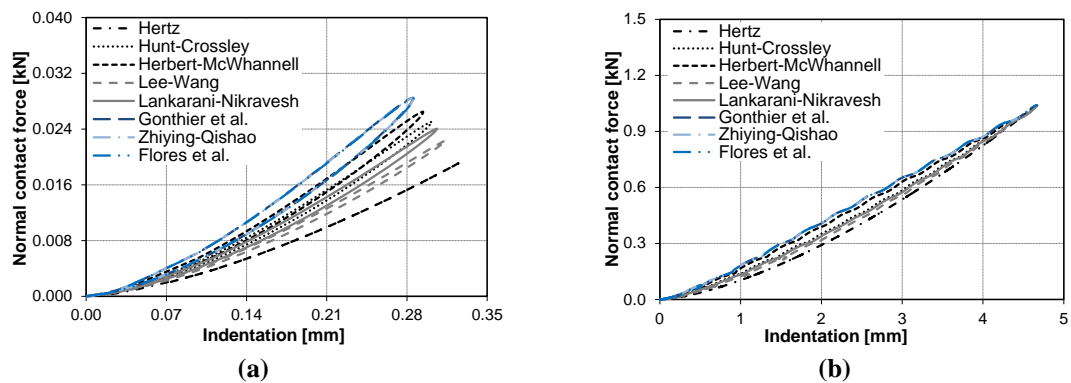

Figure 5.15 Force-indentation relation of a healthy knee model analyzed by different contact force laws: (a) First impact; (b) Whole simulation.

The use of Hertz contact law produces the higher indentations, as it can be seen in Figure 5.13. This fact is logical because the Hertz law is a pure elastic force model that does not account for any energy dissipation during the contact process. This observation is also visible in the diagram of Figure 5.15, where the curve for the Hertz law does not present a hysteresis loop, meaning that the energy stored during the loading phase is exactly the same that is restored during the unloading phase.

By observing the plots of Figures 5.13-5.15, it can be concluded that the use of the model proposed by Flores *et al.* (2011) gives a contact response similar to the application of the Gonthier *et al.* (2004) model or the Zhiying and Qishao (2006) approach. Figure 5.15a depicts that these models allow higher values of energy dissipation during the impact, because their hysteresis loops exhibit the largest area.

Herbert and McWhannell (1977) model is the contact force law that produces a contact response closer to the Flores *et al.* (2011) model, among the Gonthier *et al.* (2004) and Zhiying and Qishao (2006) approaches. In turn, Lee and Wang (1983) force law is the dissipative model that produces impacts with higher indentation, because the

less amount of energy loss. The smallest hysteresis loop reported for Lee and Wang (1983) model in Figure 5.15a justifies this idea. Lankarani and Nikravesh (1990) model and Hunt and Crossley (1975) approach exhibit intermediate behaviors between Herbert and McWhannell (1977) force model and Lee and Wang (1983) contact laws.

Figure 5.15a shows the force-indentation relations for the first impact of the knee joint that result of the application of each contact force law listed in Table 5.4. Except for the Hertz's law, all the hysteresis curves plotted describe closed-loops, which is typical of the force-indentation relation modeled by a dissipative force model. Indeed, a dissipative force law usually describes the contact phenomenon into two distinct periods, namely the loading phase and the unloading phase. Nevertheless, this characteristic of closed-shape is not observable in the hysteresis loops of Figure 5.15b, which illustrates the same results for the whole simulation. This outcome is due to the continuous motion of knee that leads to long contacts, meaning that the unloading phases do not occur totally. Figure 5.13b confirms also this observation, where it is visible that from the second impact the contact indentation never returns to zero values.

In summary, significant differences were reported on the dynamic response of the knee joint using distinct contact force models. This outcome emphasized the necessity of using a suitable contact force law to evaluate the knee contact forces. As mentioned previously, the distal femur and the proximal tibial are covered by cartilage, which is a biological soft-tissue with nonlinear damping properties. Therefore, a contact force law that characterize in a realistic way this material response should be employed. From these reasons, the Flores *et al.* force model is recommended and used for knee contact analysis because this contact force law is able to provide accurate contact responses for moderate coefficients of restitution as the coefficient of restitution of the cartilage.

5.5   Influence of the contact material properties

The materials properties of the contacting bodies play a crucial role on the dynamic response of the system, since they directly affect the magnitude of the contact forces, the amount of energy dissipated during the contact and, hence, the motion of the bodies. The contact material between the femur and the tibia, in a healthy natural knee articulation, is composed by a hyaline cartilage layer with approximated 4.15 mm of thickness, *i.e.* 2.45 mm on femur and 1.70 mm on tibia (Martelli *et al.*, 2007). However, in several cases, the subject can present a knee pathology that significantly changes the

contact material properties. For example, Osteoarthritis is the most common cause of musculoskeletal pain and disability at the knee joint. In a broad sense, OA can be defined as mechanically induced cartilage loss, which is characterized by a decrease in cartilage volume and thickness that could ultimately lead to the exposition of the underlying bone (Wilson *et al.*, 2005; Moskowitz, 2007). Nevertheless, OA diseases may be initiated by multiple factors, not only mechanical factors, but also biological, genetic, metabolic, and traumatic. The knee OA entails not only cartilage loss, but also bony remodeling, with capsular stretching and weakness of the muscles that surround the knee joint. With a large enough area of cartilage loss or with bony remodeling, the joint becomes tilted, and the misalignment develops, which is the most powerful risk factor for structural deterioration of the joint (Felson, 2006). Therefore, in OA severe stage, the contact material started to be composed by bone, whose mechanical behavior is quite different from the cartilage. In a similar way, for patients with Osteoporosis (OP), which is characterized by the loss of bone mechanical properties, the material properties can vary significantly (Dickenson *et al.*, 1981). In order to examine how the dynamic response of the knee is affected by the intrinsic material properties, five different contact situations are considered: (*i*) a healthy knee with a homogeneous contact interface of hyaline cartilage; (*ii*) an artificial knee with a tibial insert made of ultra-high molecular weight polyethylene (UHMWPE) and a femoral component composed by a chromium-cobalt alloy (Cr-Co); (*iii*) a pathologic knee with a double contact interface composed by hyaline cartilage and normal bone (90%OA knee); (*iv*) a pathologic knee with a double contact interface composed by hyaline cartilage and osteoporotic bone (90%OA+OP knee); (*v*) a pathologic knee with a homogeneous contact interface of osteoporotic bone (100%OA+OP knee). The material properties necessary to characterize these five contact interfaces are listed in Table 5.5.

Table 5.5 Mechanical properties of the contact materials (Dickenson *et al.*, 1981; Piazza and Delp, 2001; Kurtz, 2004; Herman, 2007; Burgin and Aspen, 2008; Heijink *et al.*, 2008).

Material	Young's modulus [MPa]	Poisson's Ratio	Coefficient of restitution
Hyaline cartilage	24	0.38	0.616
Normal bone	17200	0.39	0.620
Osteoporotic bone	12000	0.39	0.620
UHMWPE	800	0.46	0.790
Cr-Co alloy	200000	0.30	0.790

As mentioned above, OA initiation and its progression can be associated with multiple factors, such as mechanical, biological, genetic, among others. Since it is extremely difficult to model a pathologic knee that accounts for all these issues,

simplified models are considered. In this work, only the cartilage loss effect mechanically induced is considered, being the remaining OA factors neglected. To model the cartilage loss a reduction on the original thickness of the cartilage layer is made. This reduction is considered proportional to the percent of OA severity. Thus, the pathologic knee labeled as 90%OA knee simulates a knee joint that had lost 90% of the original cartilage layer. In turn, the knee model referred as 90%OA+OP knee, is similar to the previous one, only has a 10% of the original cartilage layer and furthermore the bony tissue is osteoporotic. The 100%OA+OP knee model represents an osteoporotic knee that lost 100% of the original cartilage layer. It is important to mention that is more difficult to simulate a 90%OA model than the 100%OA model, since the former has a double contact layer. To keep the analysis simple, the first layer of the 90%OA knees is modeled as a layer with uniform thickness that is located along the geometric profile. As far as the contact force model is concerned, a few adjustments have to be done in order to account for two contact layers. Thus, for sake of simplicity, in double layer scenarios the contact force corresponds to the sum of the contact forces in each layer, which can be given by

$$F_N = \begin{cases} F_1 & \text{if } \delta \leq h_{s_1} \\ F_1^{max} + F_2 & \text{if } \delta > h_{s_1} \end{cases} \tag{5.32}$$

where F_N is the total normal contact force, F_1 and F_1^{max} represent the normal contact force resultant from a partial or total indentation of the thickness of the first contact layer, and F_2 is the normal contact force at the second contact layer that is null when the relative indentation is smaller than or equal to the thickness of the first layer, h_{s_1}. For instance, for Hertz contact law the Equation (5.32) can be written as

$$F_N = \begin{cases} K_1 \delta^n \\ K_1 h_{s_1}^n + K_2 \left(\delta - h_{s_1} \right)^n \\ \quad \text{if } \delta \leq h_{s_1} \\ \quad \text{if } \delta > h_{s_1} \end{cases} \tag{5.33}$$

where K_1 and K_2 represent the generalized stiffness of first and second contact layers, respectively, having the remaining parameters the same meaning as described above.

Computational simulations using the five knee models are performed, being the normal contact forces evaluated by employing the Hertz contact law. The results obtained are plotted in in Figures 5.16-5.19. The force-indentation relations of each knee model for the first impact and for the whole simulation are illustrated in Figure 5.16. The evolution of the contact indentation and forces along the knee extension is depicted in Figures 5.17-5.19. By observing the plots of Figures 5.16-5.19, it is visible that the healthy knee model presents the highest values of indentation and the lowest values of normal contact force. This outcome is associated with the material properties of the contact interface, namely its stiffness and damping characteristics. The hyaline cartilage, that the healthy contact interface is made of, is the bearing material with a lower value for the stiffness parameter. Due to the soft nature of the healthy knee, this model extends the contact period for a longer time and allows higher contact indentations than the other knee models. Moreover, the cartilage produces lower contact forces due to its compliance and ability to absorb the impact energy. This observation highlights the key role played by the cartilage as shock absorber and load spreader.
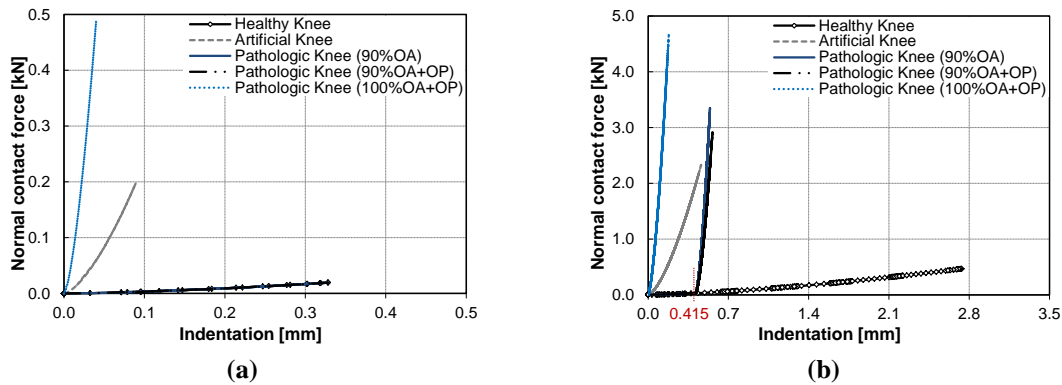
Figure 5.16   Force-indentation relation of the five knee models: (a) First impact; (b) Whole simulation.
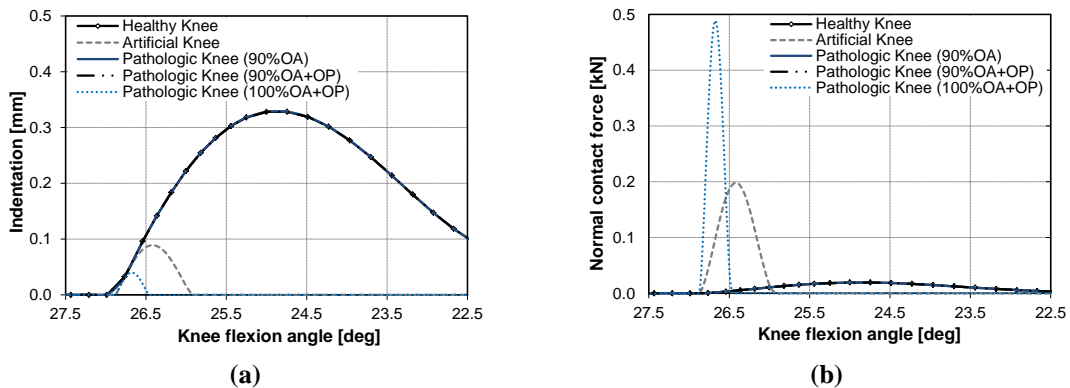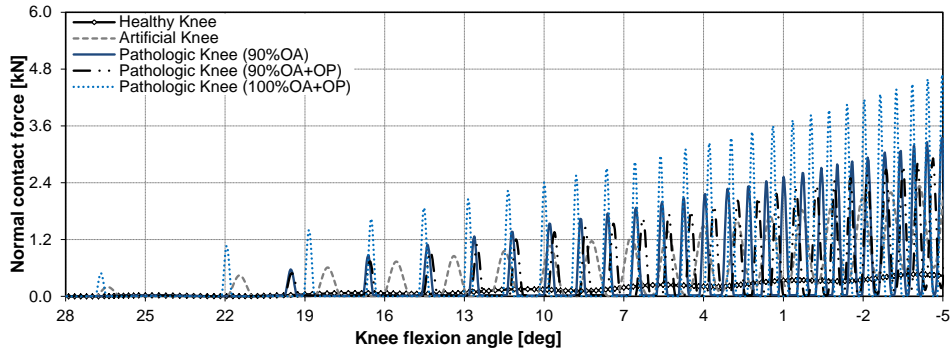

Figure 5.17   Contact response of the five knee models along the knee flexion angle during the first contact (from 27.5 to 22.5 degrees of flexion): (a) Indentation; (b) Normal contact force.
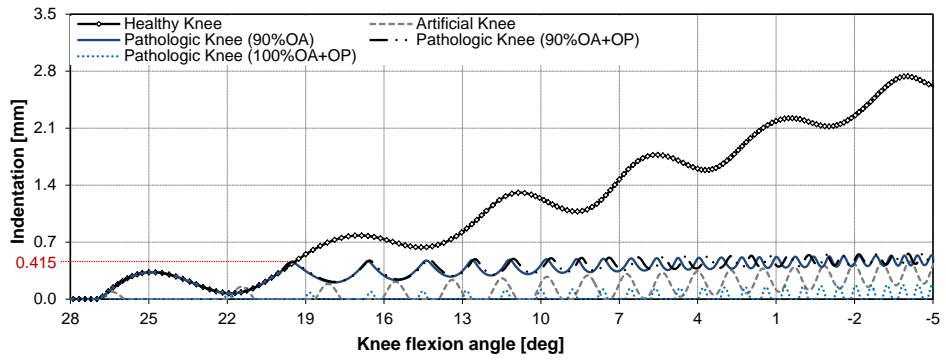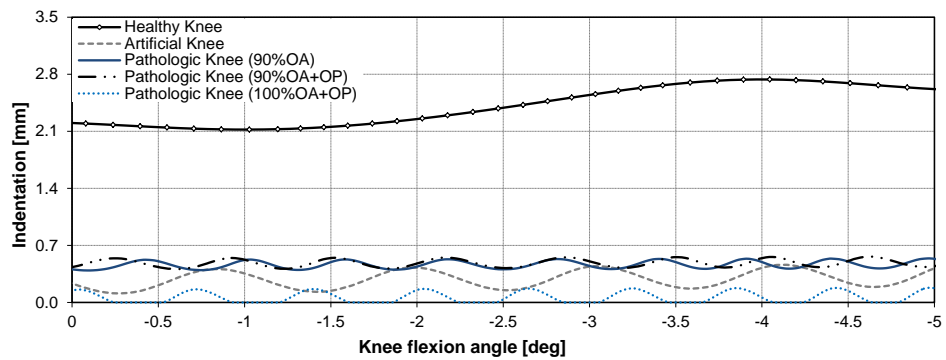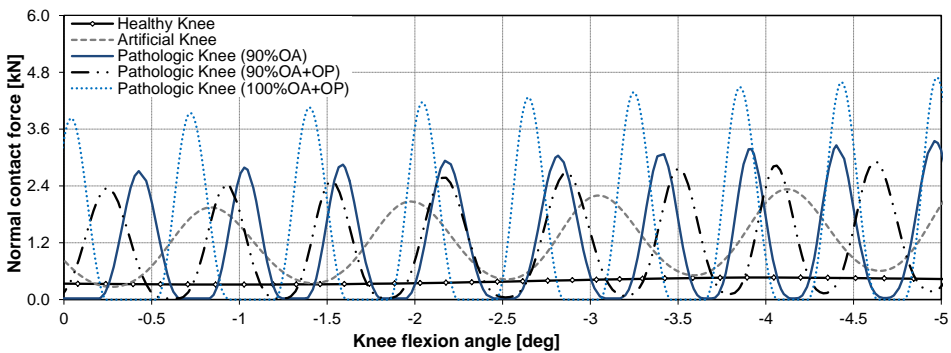
(a)

(b)

Figure 5.18   Contact response of the five knee models along the knee flexion angle during the whole contact period (from 28 to -5 degrees of flexion): (a) Indentation; (b) Normal contact force.

(a)

(b)

Figure 5.19   Dynamic response of the five knee models during the knee hyperextension (from 0 to -5 degrees of flexion): (a) Indentation *versus* knee flexion angle; (b) Normal contact force *versus* knee flexion angle.

Observing Figures 5.16, 5.17 and 5.18a, it can be concluded that the healthy knee model and the pathologic models 90%OA knee and 90%OA+OP knee exhibit the same response for indentation up to 0.415 mm, which corresponds to a 10% of the original thickness of the cartilage. However, when the indentation is greater than 0.415 mm, the contact forces developed in these pathologic models increase significantly. This behavior is associated with the contact material that changes from cartilage to bone, which is stiffer. Analyzing the two pathologic knees with cartilage, namely 90%OA knee and the 90%OA+OP knee, it can be stated that they present a similar behavior. Although, it can be observed that, for the same indentation, the 90%*OA* knee produces higher contact forces when compared to the 90%OA+OP knee case. This outcome, also reported by Dickenson *et al.* (1981), sounds reasonable because OP is a metabolic disease characterized by a general reduction of bone mass, which reduces its stiffness.

As far as the Cr-Co-UHMWPE prosthesis is concerned, the results obtained show that artificial knee model promotes longer contacts and lower contact forces than the pathologic knees, as it can be seen in Figures 5.17b and 5.18b. This outcome can be justified by the moderate stiffness of the artificial contact interface that is due to the UHMWPE, which is a material with elastic properties closer to the hyaline cartilage. This assumption can explain why clinicians prescribe knee arthroplasties, *i.e.*, knee replacements, to patients who present severe Osteoarthritis and practically do not have cartilage coating on their knee bony structures.

In order to study the influence of the contact material interface together with the contact force model, several simulations were performed using different contact force laws. In these simulations, elastic and dissipative force approaches were considered. As a result, the pathologic knee models with cartilage, namely 90%OA and 90%OA+OP, were excluded from the simulations since these models rely on the initial velocity of indentation that is a parameter difficult to predict when a double contact layer is used. The force-indentation relations of the pathologic model (100%OA+OP knee) and the artificial model are shown in Figures 5.20 and 5.21, respectively. Analyzing Figures 5.15, 5.20 and 5.21, it can be concluded that the contact force model affects the knee joint dynamics, regardless the nature of its contact interface. The obtained results revealed that the influence of the contact force law is less noticeable in the artificial knee than in the other two remaining models. This outcome is due to the value of coefficient of restitution that is higher at the artificial knee ($c_r = 0.790$) than at the

pathologic knee ($c_r = 0.620$) and at the healthy knee ($c_r = 0.616$). Some of the applied dissipative laws, such as Lankarani-Nikravesh model, are not able to account for high amounts of energy loss, which are generally associated with low values of coefficient of restitution. Hence, this statement can also be used to justify the obtained results.
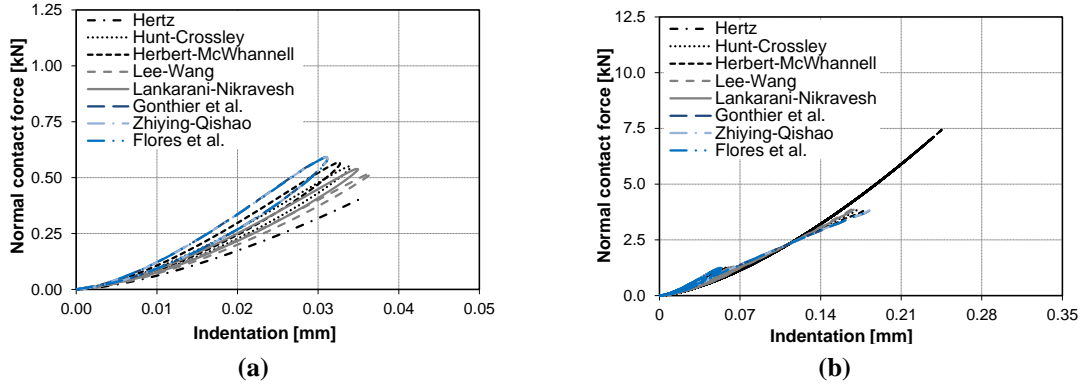

Figure 5.20 Force-indentation relations for the pathologic model (100%OA+OP knee) analyzed by different contact force laws: (a) first impact; (b) whole simulation.
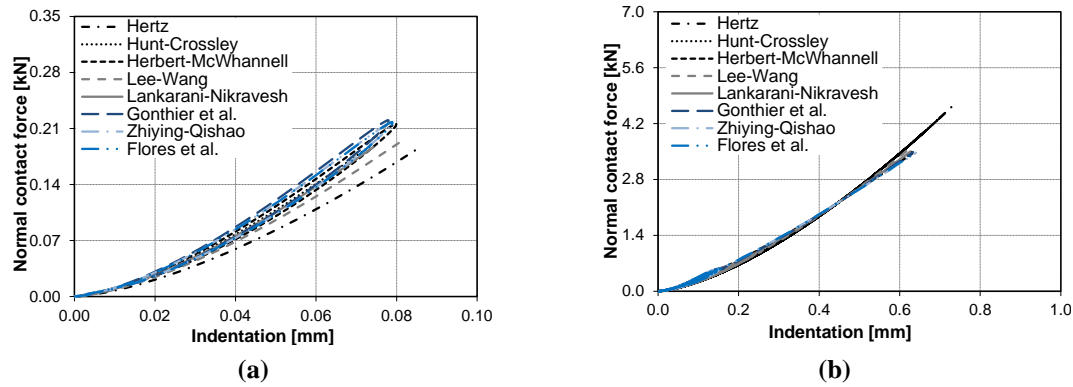
Figure 5.21 Force-indentation relations for the artificial knee model analyzed by different contact force laws: (a) first impact; (b) whole simulation.

5.6   Influence of the amplitude of the external applied force

An external force is applied to the center of mass of the tibia aiming to promote the tibiofemoral contact and also provide a knee extension motion. This force is an exponentially decaying sinusoidal pulsed function with amplitude A. With the purpose of studying the influence of the amplitude of the external applied force on the dynamics of the healthy knee model, computational simulations were carried out using two different values for amplitude A, namely 50 N and 150 N. The shape preserving interpolation technique was employed to define the contact profiles. The purely elastic Hertz law and the dissipative model of Flores *et al.* were used to compute the normal contact forces. Regarding the material properties, a generalized stiffness of 3260513 N/m$^{1.5}$ and a coefficient of restitution of 0.616 were utilized to describe the articular

cartilage. The simulations were performed for 0.4 s of duration with a time step of 1×10^{-4} s. Figures 5.22 and 5.23 depict the ligament forces along the knee flexion angle for two different values of amplitude of the external applied force, respectively, 50 N and 150 N. Figures 5.24, 5.25 and 5.26 show the evolution of the indentation, the velocity of indentation and the normal contact force along knee flexion angle for amplitude *A* of 50 N and 150 N. The tibia contact points for amplitude *A* of 50 N and 150 N are plotted in Figure 5.27. Figures 5.22a-5.27a show the results obtained when the Hertz law is utilized to compute the contact forces, while the plots of Figures 5.22b-5.27b are the result of the use of the Flores *et al.* model on the evaluation of the contact forces. Figure 5.28 illustrates the force-indentation relations obtained using the Flores *et al.* model for amplitude *A* of 50 N and 150 N.

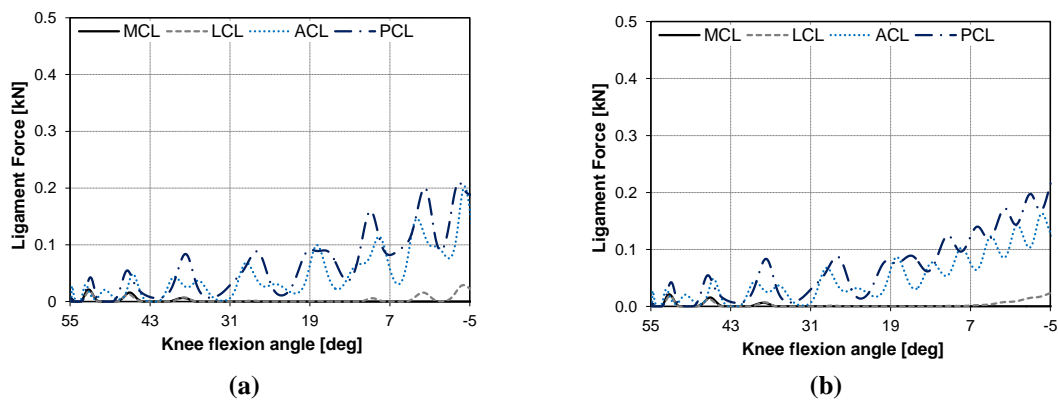(a)   (b)

Figure 5.22   Ligament forces along flexion angle for an amplitude of external force equal to 50 N, when the contact forces are computed by: (a) Hertz law; (b) Flores *et al.* model.
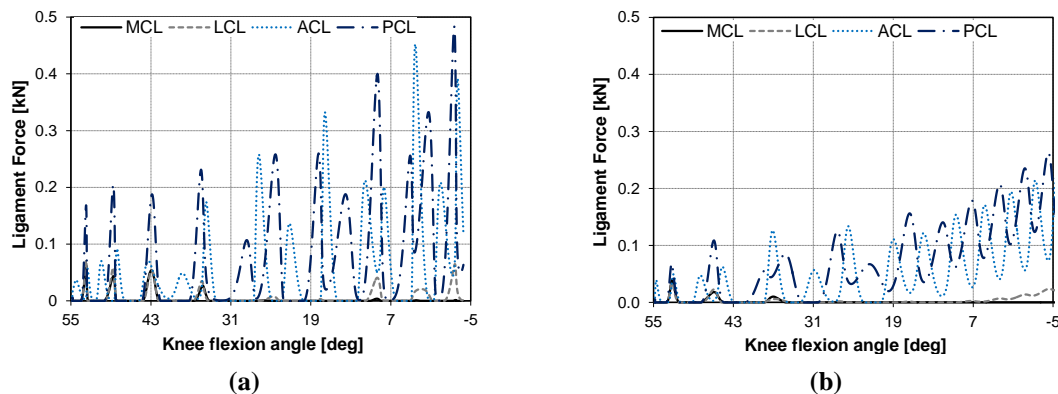

(a)   (b)

Figure 5.23   Ligament forces along flexion angle for an amplitude of external force equal to 150 N, when the contact forces are computed by: (a) Hertz law; (b) Flores *et al.* model.

Figures 5.22 and 5.23 show that the increase of the amplitude of the external force rises the forces on the ligaments. The forces of the collateral ligaments are lower than those for the cruciate ligaments. The smaller resistance of the collateral ligaments was expected since the main function of these two ligaments is to offer varus-valgus and

internal-external rotational stability, which are knee movements that do not occur in sagittal plane, used for this study, but in the frontal and transverse planes, respectively (Hirokawa, 1993). The increase of ACL and PCL forces with the increase of the amplitude of the external force was also predictable since these ligaments have the key role of balancing the knee motion in the sagittal plane. This dynamic response of the cruciate ligaments justifies why these ligaments are commonly injured, especially during sport activities and motor vehicle accidents that generally involve high dynamic forces caused by twisting or hyperextending the knee joint (Limbert *et al.*, 2004).

By analyzing Figures 5.22 and 5.23, it can be concluded that the ligament forces are higher when the contact forces are evaluated using the Hertz contact law. This outcome is explained by the purely elastic nature of the Hertz law that computes the contact forces based only on the generalized stiffness parameter and the relative distance between the femur and the tibia, which is constrained by the ligaments. When the amplitude of external force is set to 50 N, the ligament forces produced when the contact forces are calculated by the Hertz law are similar to the ones obtained when the Flores *et al.* model is applied (see Figure 5.22). Nonetheless, for an amplitude of external force of 150 N, the ligament forces are much higher when the Hertz law is used to compute the contact forces (see Figure 5.23). This outcome emphasizes the dependence of the ligament forces on the contact forces and the importance of taking into account the relative velocity of indentation and the coefficient of restitution of the articular cartilage on the computation of the knee contact forces.
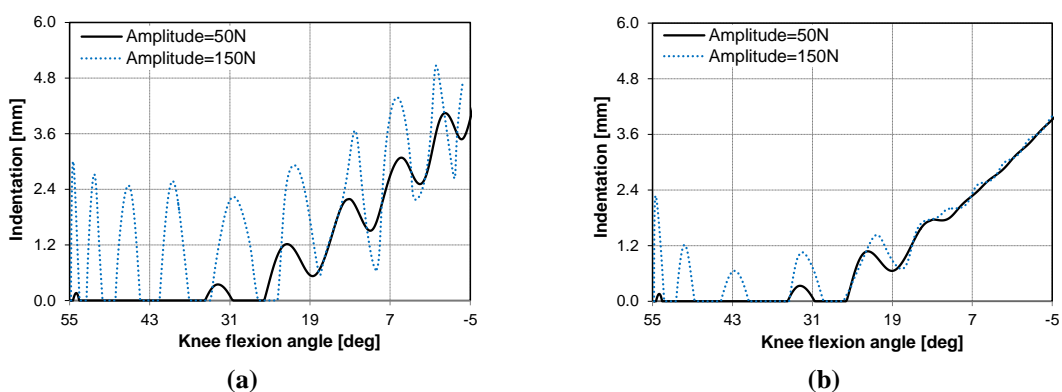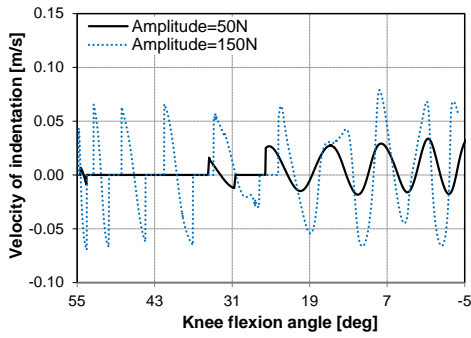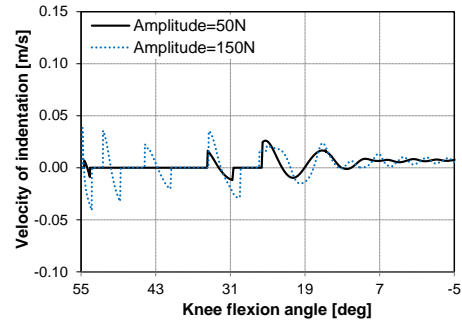

Figure 5.24 Indentation along flexion angle for two different values of amplitude of external force, when the contact forces are computed by: (a) Hertz law; (b) Flores *et al.* model.
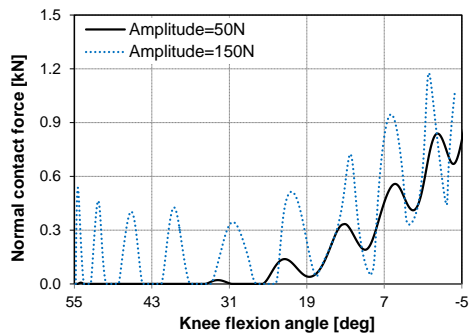
Figure 5.25 Velocity of indentation along flexion angle for two different values of amplitude of external force, when the contact forces are computed by: (a) Hertz law; (b) Flores *et al.* model.
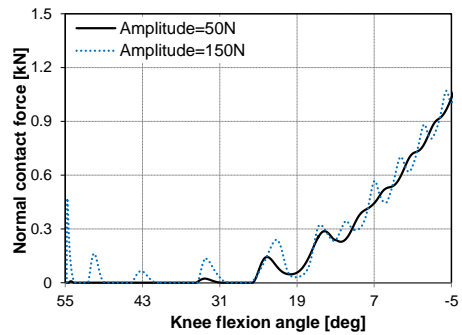

Figure 5.26 Normal contact forces along flexion angle for two different values of amplitude of external force, when the contact forces are calculated by: (a) Hertz law; (b) Flores *et al.* model.
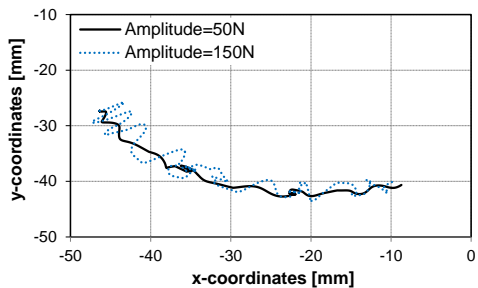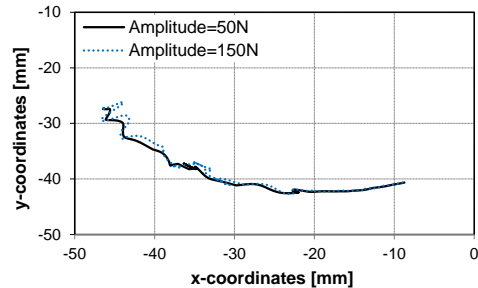

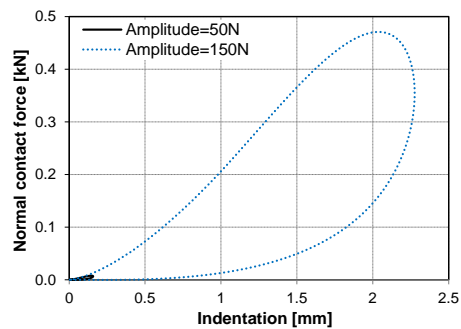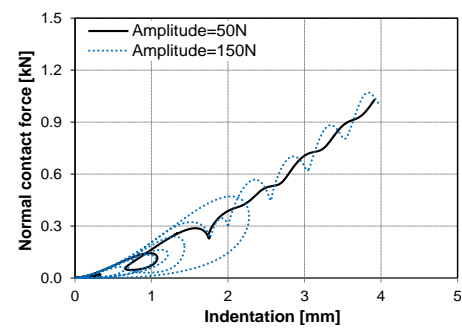**Figure 5.27** Tibia contact points for two different values of amplitude of external force, when the contact forces are computed by: (a) Hertz contact law; (b) Flores *et al.* model.

Figure 5.28 Normal contact force *versus* indentation for two different values of amplitude of external force using the Flores *et al*. contact force model: (a) First impact; (b) Whole simulation.

Figures 5.24a-5.26a show that the increase of the amplitude of the external force has a great influence on the contact response of the system when the contact is considered purely elastic, increasing significantly the indentation, the velocity of indentation and the normal contact force. The higher indentations reported in Figure 5.24a for amplitude of external force of 150 N are also noticeable in Figure 5.27a, where the trajectory of the tibia contact points is plotted.

When the tibiofemoral contact is modeled as inelastic and the Flores *et al.* model is used to compute the normal contact forces, the increase of the amplitude of the external force does not affect significantly the contact response of the system, as it can be seen in Figure 5.24b-5.26b. This behavior is also visible in Figure 5.27b, where the trajectories of the contact points for amplitude A of 50 N and 150 N are practically coincident. In the inelastic contact scenario, the major effect of the increase of amplitude of the external force is on the energy dissipation due to internal damping, as it can be seen in Figure 5.28. The force-indentation relations of the first impact for amplitude A of 50 N and 150 N are depicted in Figure 5.28a. By analyzing Figure 5.28a, it can be concluded that the area of the hysteresis loop for an amplitude A of 150 N is approximately 844 times greater than the hysteresis loop resultant of the use of an external force with an amplitude A of 50 N.

In a broad sense, the computational results presented and discussed in this Section highlight the outstanding damping properties of the cartilage and its key role as shock absorber, as well as the importance of using a nonlinear dissipative contact law to evaluate the contact forces at the human knee.

5.7   Summary and discussion

A two-dimensional model of the knee joint was presented throughout this Chapter. The model was formulated under the framework of multibody dynamics, as a system of two rigid bodies, femur and tibia. The femur was considered to be stationary, while the tibia rolls and slides in relation to the femur in the sagittal plane. The tibia was connected to the femur by four knee ligaments, which were modeled as nonlinear spring elements. The mechanical behavior of the ligaments was described by a quadratic stress-strain relation that is a function of the ligament stiffness and its unstrained length, being considered that the ligaments cannot carry any compressive force. The articular cartilages were considered to be deformable structures with specific material

characteristics. The motion of the tibia relative to the femur was not modeled with conventional kinematic joint (such as a revolute joint), but rather in terms of the action of the knee ligaments and potential contact between the bones. In order to avoid the separation of the tibia due gravitational action and to promote the tibiofemoral contact, an external force was applied to the tibia center of mass, which provides the knee motion from an initial position of flexion to a final pose of hyperextension.

Several methodologies were proposed to model the human knee as a free contact joint. Firstly, an approach to define the knee geometric outlines was presented, which consisted of extracting points from an MRI image and described it using cubic spline interpolation functions. For the contact detection process, a mathematical formulation that relies on the common-normal concept was expounded. This method states that two points are the potential contact points if the normal vectors at these points are collinear to each other and perpendicular with the tangential vector. To guarantee that a pair of points is an actual contact pair, an indentation condition has also to be checked. When a contact is detected and indentation is greater than zero, a continuous force law is applied which allows for calculation of the contact forces generated at the contact interface as a function of the relative indentation between the two bodies. The contact forces, together with the external applied force and the forces produced by the ligaments, were introduced into the system's equations of motion as generalized forces.

Dynamic computational simulations were performed using the developed knee multibody system in order to validate the model and to study the influence of some important parameters on its dynamic response, namely (*i*) the spline interpolation method used to describe the contact geometry of the bodies, (*ii*) the geometric conformality of contacting bodies, (*iii*) the constitutive contact force law, (i*v*) the contact material properties and, (*v*) the amplitude of the external applied force.

The effect of the use of different spline interpolation techniques was evaluated and none significant differences were reported. Even so, the use of shape preserving splines is recommended because it preserves the geometric convexity that is very important for contact detection purposes.

The proximal tibia presents a concave shape in knee medial compartment and a convex shape in knee lateral compartment, while the distal femur have a convex shape in both sides of the knee. Based on this scenario, computational simulations were

performed considering three distinct geometric contact scenarios in order to study the influence of the geometric conformality on the dynamic response of the knee model. The results depicted that the knee medial compartment, which has a conformal configuration, presents higher contact forces when compared with the knee lateral compartment. This observation can explain the major incidence of Osteoarthritis at the medial compartment of the human knee joint.

In what concerns with the constitutive contact force law, the approaches proposed by Gonthier *et al.* (2004), Zhiying and Qishao (2006) and Flores *et al.* (2011) demonstrated to be reasonable options to compute the knee contact forces, since they describe the nonlinear behavior of the hyaline cartilage and also take into account its damping properties typical of soft and inelastic materials. The remaining contact formulations underestimated the contact forces and overestimated the maximal contact indentations and the duration of the contact events. These outcomes highlight the importance of the constitutive contact force methods on the prediction of the dynamic response of multibody biomechanical systems.

Regarding the materials of the knee contact interface, it was shown that the presence of the hyaline cartilage reduces the contact force and extends the period of contact due to its elastic and damping properties that made the cartilage an outstanding shock absorber and load spreader. This cartilage role is of paramount importance during walking, since the ground reaction force typically rises to a peak after heel strikes and during this phase the loads across the human knee joint have been calculated to be about three times the body weight (Andriacchi and Dyrby, 2005). In turn, the presence of Osteoporosis does not increase the knee contact forces, which means that this disease does not contribute to the Osteoarthritis progression.

As far as the artificial knee model is concerned, the results obtained revealed that, for higher contact indentations, the artificial knee model produces lower contact forces than the pathologic models, which are destitute of almost all of the coating of articular cartilage. This suitable dynamic response of the artificial knee model is due to the outstanding elastic and damping properties of the UHMWPE that makes it the most used bearing material in joint replacement systems (Kurtz, 2004).

The ligament forces were also analyzed in this work, being the forces produced by the collateral ligaments lower than those of the cruciate ligaments. The higher forces of

cruciate ligaments are justified by its biomechanical role of stabilizing the knee joint while allowing a very large range of motion. The smaller resistance of the collateral ligaments is due to the fact that the main function of these ligaments is to offer varus-valgus and rotational stability, which are knee movements that do not occur in sagittal plane, used for this study.

Furthermore, the numerical results demonstrated that the increase of the amplitude of the external applied force has a great influence on the contact response of the knee system when the contact is considered purely elastic, increasing significantly the indentation, the velocity of indentation and the normal contact force. This outcome is due to the fact that the evaluation of the contact forces using an elastic contact law, such as Hertz law, is based only on the generalized stiffness parameter and the relative distance between the femur and the tibia, which is constrained by the ligaments. In turn, when a dissipative force law, such as the Flores *et al.* model, is applied to compute the contact forces the relative velocity of indentation and the coefficient of restitution of the cartilage are considered. As a result, an increase of the amplitude of the external force does not affect significantly the contact response of the knee system, but only the amount of energy loss due to internal damping. This study demonstrates the importance of using an appropriate nonlinear dissipative contact law (*i.e.*, able to provide an accurate contact response for moderate coefficients of restitution such as the coefficient of restitution of the cartilage) to evaluate the contact forces at the human knee joint.

References

Abdel-Rahman, E.M., Hefzy, M.S. (1993) A two-dimensional dynamic anatomical model of the human knee joint. *Journal of Biomechanical Engineering*, 115(4A), pp. 357-365.

Abdel-Rahman, E.M., Hefzy, M.S. (1998) Three-dimensional dynamic behaviour of the human knee joint under impact loading. *Medical Engineering & Physics*, 20(4), pp. 276-290.

Akima, H. (1970) A new method of interpolation and smooth curve fitting based on local procedures. *Association for Computing Machinery*, 17(4), pp. 589-602.

Andriacchi, T.P., Dyrby, C.O. (2005) Gait analysis and total knee replacement. In J. Bellemans, M.D. Ries, J. Victor (Eds.), *Total Knee Arthroplasty- A guide to get better performance* (pp. 38-42). Springer: Heidelberg, Germany.

Bei, Y., Fregly, B.J. (2004) Multibody dynamic simulation of knee contact mechanics. *Medical Engineering & Physics*, 26(9), pp. 777-789.

Butler, D.L., Grood, E.S., Noyes, F.R., Zernicke, R.F. (1978) Biomechanics of ligaments and tendons. *Exercise and Sports Science Reviews*, 6, pp. 125-181.

Burgin, L.V., Aspen, R.M. (2008) Impact testing to determine the mechanical properties of articular cartilage in isolation and on bone. *Journal of Materials Science: Materials in Medicine*, 19(2), pp. 703-711.

Chapra, S.C., Canale, R.P. (1989) *Numerical Methods for Engineers*. McGraw-Hill: New York (NY).

Crowninshield, R., Pope, M.H., Johnson, R.J. (1976) An analytical model of the knee. *Journal of Biomechanics*, 9(6), pp. 397-405.

De Boor, C. (2001) *A Practical Guide to Splines*. Springer-Verlag: New York (NY).

Dickenson, R.P., Hutton, W.C., Stott, J.R. (1981) The mechanical properties of bone in Osteoporosis. *The Journal of Bone & Joint Surgery - B*, 63B(2), pp. 233–238.

DICOM sample image sets (URL: http://pubimage.hcuge.ch:8080/, accessed on February 16th 2009).

Engin, A.E., Akkas, N.(1978) Application of a fluid-filled spherical sandwich shell as a biodynamic head injury model for primates. *Aviation, Space, and Environmental Medicine*, 49(1-2), pp. 120-124.

Engin, A.E., Tumer, S.T. (1993) Improved dynamic model of the human knee joint and its response to impact loading on the lower leg. *Journal of Biomechanical Engineering*, 115(2), pp. 137-143.

Felson, D.T. (2006) Osteoarthritis of the knee. *The New England Journal of Medicine*, 354(8), pp. 841-848.

Ferziger, J.H. (1998) *Numerical Methods for Engineering Application*. John Wiley & Sons: New York (NY).

Flores, P. (2010) *MUBODYNA—A FORTRAN Program for Dynamic Analysis of Planar Multibody Systems*, University of Minho, Guimarães, Portugal.

Flores, P., Ambrósio, J. (2010) On the contact detection for contact-impact analysis in multibody systems. *Multibody System Dynamics,* 24(1), pp. 103-122.

Flores, P., Machado, M., Silva, M.T., Martins, J.M. (2011) On the continuous contact force models for soft materials in multibody dynamics. *Multibody System Dynamics*, 25(3), pp. 357-375.

Gonthier, Y., McPhee, J., Lange, C., Piedboeuf, J.-C. (2004) A regularized contact model with asymmetric damping and dwell-time dependent friction. *Multibody System Dynamics*, 11(3), pp. 209-233.

Hawkins, D., Bey, M. (1997) Muscle and tendon force-length properties and their interactions in vivo. *Journal of Biomechanics*, 30(1), pp. 63-70.

Heijink, A., Zobitz, M.E., Nuyts, R., Morrey, B.F., An, K.N. (2008) Prosthesis design and stress profile after hip resurfacing: a finite element analysis. *Journal of Orthopaedic Surgery*, 16(3), pp. 326-332.

Herbert, R.G., McWhannell, D.C. (1977) Shape and frequency composition of pulses from an impact pair. *Journal of Engineering for Industry*, 99(3), pp. 513-518.

Herman, I.P. (2007) *Physics of the human body*. Springer-Verlag: New York (NY).

Hertz, H. (1881) Über die Berührung fester elastischer Körper. *Journal für die reine und angewandte Mathematik*, 92, pp. 156-171.

Hirokawa, S. (1993) Biomechanics of the knee joint: a critical review. *Critical Reviews in Biomedical Engineering*, 21(2), pp. 79-135.

Hunt, K.H., Crossley, F.R.E. (1975) Coefficient of restitution interpreted as damping in vibroimpact. *Journal of Applied Mechanics*, 42(2), pp. 440-445.

Irvine, L.D., Marin, S.P., Smith, P.W. (1986) Constrained interpolation and smoothing. *Constructive Approximation*, 2(1), pp. 129-151.

Koo, S., Andriacchi, T.P. (2007) A comparison of the influence of global functional loads vs. local contact anatomy on articular cartilage thickness at the knee. *Journal of Biomechanics*, 40(13), pp. 2961-2966.

Koo, S., Gold, G., Andriacchi, T.P. (2005) Considerations in measuring cartilage thickness using MRI: factors influencing reproducibility and accuracy. *Osteoarthritis Cartilage*, 13(9), pp. 782-789.

Korhonen, R.K., Laasanen, M.S., Töyräs, J., Rieppo, J., Hirvonen, J., Helminen, H.J., Jurvelin, J.S. (2002) Comparison of the equilibrium response of articular cartilage in unconfined compression, confined compression and indentation. *Journal of Biomechanics*, 35(7), pp. 903-909.

Kurtz, S.M. (2004) *The UHMWPE Handbook – Principles and clinical applications in total joint replacement*. Elsevier Academic Press: San Diego (CA).

Kvasov, B.I. (2000) *Methods of shape-preserving spline approximation*. World Scientific Publishing: Singapore.

Lankarani, H.M., Nikravesh, P.E. (1990) A contact force model with hysteresis damping for impact analysis of multibody systems. *Journal of Mechanical Design*, 112(3), pp. 369-376.

Lee, T.W., Wang, A.C. (1983) On the dynamics of intermittent-motion mechanisms. Part 1 - Dynamic model and response. *Journal of Mechanisms, Transmissions, and Automation in Design*, 105, pp. 534-540.

Limbert, G., Taylor, M., Middleton, J. (2004) Three-dimensional finite element modelling of the human ACL: simulation of passive knee flexion with a stressed and stress-free ACL. *Journal of Biomechanics*, 37(11), pp. 1723-1731.

Lin, Y-C., Walter, J.P., Banks, S.A., Pandy, M.G., Fregly, B.J. (2010) Simultaneous prediction of muscle and contact forces in the knee during gait. *Journal of Biomechanics*, 43(5), pp. 945-952.

Lu, T-W., Tsai T-Y., Kuo, M-Y., Hsu, H-C-, Chen, H-L. (2008) In vivo three-dimensional kinematics of the normal knee during active extension under unloaded and loaded conditions using single-plane fluoroscopy. *Medical Engineering & Physics*, 30(8), pp. 1004-1012.

Machado, M., Flores, P., Ambrósio, J., Completo, A. (2011) Influence of the contact model on the dynamic response of the human knee joint. *Proceedings of the Institution of Mechanical Engineers, Part K: Journal of Multi-body Dynamics*, 225(4), pp. 344-358.

Machado, M., Flores, P., Claro, J.C.P., Ambrósio, J., Silva, M., Completo, A., Lankarani, H.M. (2010) Development of a planar multibody model of the human knee joint. *Nonlinear Dynamics*, 60(3), pp. 459-478.

Martelli, S., Pinskerova, V., Visani, A. (2006) Anatomical investigation on the knee by means of computer-dissection. *Journal of Mechanics in Medicine and Biology*, 6(1), pp. 55-73.

McGinty, G., Irrgang, J.J., Pezzullo, D. (2000) Biomechanical considerations for rehabilitation of the knee. *Clinical Biomechanics*, 15(3), pp. 160-166.

Micchelli, C.A., Smith, P.W., Swetits, J., Ward, J.D. (1985) Constrained Lp Approximation. *Constructive Approximation*, 1(1), pp. 93-102.

Moeinzadeh, M.H. (1981) *Two and three-dimensional dynamic modeling of human joint structures with special application to the knee joint*. PhD Thesis, Ohio State University, Columbus (OH).

Moeinzadeh, M.H., Engin, A.E., Akkas, N. (1983) Two-dimensional dynamic modelling of human knee joint. *Journal of Biomechanics*, 16(4), pp. 253-264.

Moskowitz, R.W. (2007) *Osteoarthritis: diagnosis and medical/surgical management*. Lippincott Williams & Wilkins: Philadelphia (PA).

Nordin, M., Frankel, V.H. (2001) Biomechanics of the knee. In M. Nordin, V.H. Frankel (Eds.), *Basic Biomechanics of the Musculoskeletal System* (pp. 176-201). Lippincott Williams & Wilkins: Baltimore (PA).

Piazza, S.J., Delp, S.L. (2001) Three-dimensional dynamic simulation of total knee replacement motion during a step-up yask. *Journal of Biomechanical Engineering*, 123(6), pp. 599-606.

Pombo, J. (2004) *A multibody methodology for railway dynamics application*. PhD Dissertation, Technical University of Lisbon, Lisbon, Portugal.

Pombo, J., Ambrósio, J. (2008) Application of a wheel-rail contact model to railway dynamics in small radius curved tracks. *Multibody System Dynamics*, 19(1-2), pp. 91-114.

Tetsworth, K., Paley, D. (1994) Malalignment and degenerative arthropathy. *Orthopedic Clinics of North America*, 25(3), pp. 367-77.

Visual Numerics, I. (1997) *IMSL Fortran 90 Math Library 4.0 - Fortran Subroutines for Mathematical Applications*, Houston (TX).

Weiss, J.A., Gardiner, J.C. (2001) Computational modeling of ligament mechanics. *Critical Reviews in Biomedical Engineering*, 29(4), pp. 1-70.

Weiss, J.A., Gardiner, J.C., Ellis, B.J., Lujan, T.J., Phatak, N.S. (2005) Three-dimensional finite element modeling of ligaments - Technical aspects. *Medical Engineering & Physics*, 27(10), pp. 845-861.

Wilson, W., van Donkelaar, C.C., van Rietbergen, R., Huiskes, R. (2005) The role of computational models in the search for the mechanical behavior and damage mechanisms of articular cartilage. *Medical Engineering & Physics*, 27(10), pp. 810-826.

Wismans, J. (1980) *A three-dimensional mathematical model of the human knee joint*. PhD Thesis, Eindhoven University of Technology, Eindhoven, Netherlands.

Yamaguchi, G. (2001) *Dynamic Modeling of Musculoskeletal Motion*. Kluwer Academic Publishers: Dordrecht, Netherlands.

Zhiying, Q., Qishao, L. (2006) Analysis of impact process based on restitution coefficient. *Journal of Dynamics and Control*, 4, pp. 294-298.

6

A three-dimensional multibody model of the human knee joint

The finite element method (FEM) is an accurate approach for modeling and analyzing contact problems and it can calculate unique contact forces in statically indeterminate conditions, such as when contact occurs in two or more regions between the same pair of contacting bodies regardless of any assumption for the distribution of the contact stresses. Nonetheless, the high computational cost of FEM-based contact analyses, particularly due to extensive repeated geometry evaluations, significantly limits their use in dynamic simulations (Lin *et al.*, 2010). The efficiency of the computational models is a primary concern for a contact formulation as it has been recognized by many researchers, who demonstrate that most of the time consumed in simulating contact phenomena is spent on the contact detection phase (Bei and Fregly, 2004; Machado *et al.*, 2010). Multibody system (MBS) methodologies have been widely used to develop dynamic models for contact analysis. The issue related to the computational efficiency motivated this work that aims to develop a contact methodology for the simulation of the dynamic response of multibody systems with freeform contact pairs that have real-time computation demands. The human knee, which is a six degrees-of-freedom joint with complex articular surfaces that has to

withstand high loading forces during dynamic activities, is the motivation/application case used to develop the procedures proposed here in their general form.

In this Chapter, a three-dimensional multibody model of the human knee joint for contact dynamics is proposed. Firstly, a generic methodology to represent and generate freeform contact surfaces is presented. Then, the process of geometric modeling of the knee articular surfaces, namely femoral condyles and tibial plateaus, is explained. A contact modeling procedure to deal with 3D-contact problems is described, giving special emphasis to the contact detection approach. Several computational simulations using the methodology proposed are performed and the results discussed.

6.1   Fundamentals of spatial multibody modeling

An overview of the mathematical formulation and numerical methods used to model and analyze planar multibody systems is presented in Chapter 3. In a broad sense, the equations of motion that govern a multibody system in a 2D-space are the same in the 3D-space. The principal difference between the formulations for spatial and planar kinematics is the set of coordinates. Figure 6.1a illustrates a body k in the 2D-space, which can be located by specifying the global translational coordinates $\mathbf{r}_k = \begin{bmatrix} x & y \end{bmatrix}_k^T$ of the origin of the body-fixed $\xi_k \eta_k$ reference system and the angle ϕ_k of rotation of this system relative to the global xy axes. In turn, six coordinates are required to define the configuration of a body k in the 3D-space, as Figure 6.1b depicts. Three global translational coordinates $\mathbf{r}_k = \begin{bmatrix} x & y & z \end{bmatrix}_k^T$ locate the origin of the body-fixed $\xi_k \eta_k \zeta_k$ reference system relative to the global xyz axes, and three rotational coordinates ϕ_{1k}, ϕ_{2k} and ϕ_{3k} specify the angular orientation of the body (Nikravesh, 1988).
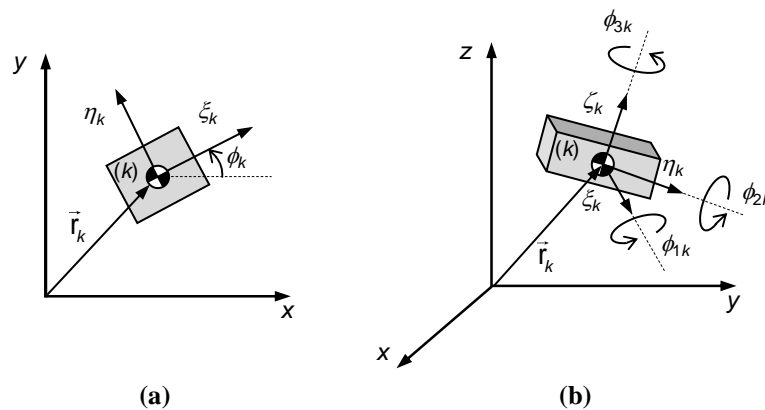

Figure 6.1   Schematic representation of a rigid body: (a) 2D-space; (b) 3D-space. In the 2D-space, 3 independent coordinates are needed to define the location of the body, while in the 3D-space it is required six independent coordinates (Nikravesh, 1988).

The analytical procedure in spatial kinematics is the same as in the planar case however spatial kinematic analysis requires more powerful mathematical techniques than planar kinematics, particularly for describing the angular orientation of a body in a global coordinate system. The angular orientation of a given body-fixed coordinate system can be projected to be the result of three successive rotations. The sequence of rotations used to define the final orientation of the coordinate system is to some extent arbitrary. A total of twelve conventions is possible in a right-hand coordinate system. Both, Euler angles and Bryant angles, are extensively utilized in multibody formulations to describe the orientation of a 3D-body by means of three rotational coordinates. Euler angles used the *x*-convention, while the Bryant angles are associated with the *xyz*-convention. The three angles of rotation can also be expressed in terms of Euler parameters. The Euler parameters are four rotational coordinates (e_0, e_1, e_2, e_3) that describe a finite rotation about an arbitrary axis, $\vec{w}$. According to the Euler's rotation theorem, there exists a unique axis that if the *xyz*-coordinate frame is rotated about it by an angle ϕ it becomes parallel to the $\xi\eta\zeta$-coordinate frame. This axis is called the orientational axis of rotation and is denoted by $\vec{w}$ in Figure 6.2 (Nikravesh, 1988).
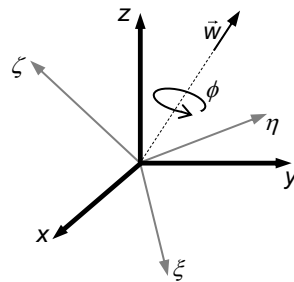

Figure 6.2   Schematic representation of an orientational axis of rotation $\vec{w}$ (Nikravesh, 1988).

The Euler parameters can be written as

$$\mathbf{p} = \begin{bmatrix} e_0 & e_1 & e_2 & e_3 \end{bmatrix}^T \tag{6.1}$$

in which $e_0 \equiv \cos(\phi/2)$ and $\mathbf{e} = \begin{bmatrix} e_1 & e_2 & e_3 \end{bmatrix}^T = \mathbf{w}\sin(\phi/2)$. Because Euler's theorem states that an arbitrary rotation may be described by only three parameters, a relation must exist between the four Euler parameters, that is

$$e_0^2 + e_1^2 + e_2^2 + e_3^2 = 1 \tag{6.2}$$

Using Euler parameters, the rotational transformation matrix of a body *k* is

$$\mathbf{A}_k = \begin{bmatrix} e_0^2 + e_1^2 - \dfrac{1}{2} & e_1 e_2 - e_0 e_3 & e_1 e_3 + e_0 e_2 \\[2mm] e_1 e_2 + e_0 e_3 & e_0^2 + e_2^2 - \dfrac{1}{2} & e_2 e_3 - e_0 e_1 \\[2mm] e_1 e_3 - e_0 e_2 & e_2 e_3 + e_0 e_1 & e_0^2 + e_3^2 - \dfrac{1}{2} \end{bmatrix} \tag{6.3}$$

Let now consider a body k to which a body-fixed $(\xi\eta\zeta)_k$ frame is attached at its center of mass, as depicted in Figure 6.1b. The position of the body with respect to global xyz coordinate system is defined by the position vector $\mathbf{r}_k = \begin{bmatrix} x & y & z \end{bmatrix}_{k}^{T}$ that represents the location on the body-fixed $(\xi\eta\zeta)_k$ frame The orientation of the body is described by means of Euler parameters, given by Equation 6.1. Thus, the vector of generalized coordinates $\mathbf{q}_k$ that completely describes the 3D-body position is given by

$$\mathbf{q}_k = \begin{bmatrix} \mathbf{r}_k^T & \mathbf{p}_k^T \end{bmatrix}_{k}^{T} \tag{6.4}$$

Regarding the velocities and accelerations of body k, the angular velocities ω'_k and accelerations $\dot{\omega}'_k$ are utilized instead of the time derivatives of the Euler parameters. This procedure simplifies the mathematical formulation and does not require the use of mathematical constraints for Euler parameters. The relation between the Euler parameters $\dot{e}_0 + \dot{e}_1 + \dot{e}_2 + \dot{e}_3 = 0$ is implied in the angular velocity and, therefore, is not used explicitly (Nikravesh and Chung, 1982). When Euler parameters are employed as rotational coordinates, the relation between their time derivatives and the angular velocities is expressed by

$$\dot{\mathbf{p}}_k = \frac{1}{2}\mathbf{L}^T \omega'_k \tag{6.5}$$

where the auxiliary 3×4 matrix $\mathbf{L}$ is a function of Euler parameters (Nikravesh, 1988)

$$\mathbf{L}_k = \begin{bmatrix} -e_1 & e_0 & e_3 & -e_2 \\ -e_2 & -e_3 & e_0 & e_1 \\ -e_3 & e_2 & -e_1 & e_0 \end{bmatrix} \tag{6.6}$$

The velocities and accelerations of body k are given by (Nikravesh, 1988)

$$\dot{\mathbf{q}}_k = \begin{bmatrix} \dot{\mathbf{r}}_k^T & \omega'^{T}_k \end{bmatrix}_{k}^{T} \tag{6.7}$$

$$\ddot{\mathbf{q}}_k = \begin{bmatrix} \ddot{\mathbf{r}}_k^T & \dot{\omega}_k'^T \end{bmatrix}_k^T \tag{6.8}$$

In this work, Euler parameters are utilized to define the angular orientation of bodies. The quadratic nature of the transformation matrix, the absence of trigonometric functions, and the singularity-free aspect of the Euler parameters make them more attractive than other sets of rotational coordinates. Another advantage of Euler parameters formulation is that it allows kinematic relationships for different pairs to be written in compact matrix form, so that compact and efficient computational algorithms can be developed. Though, it is worth noting that the methodology remains the same if other sets of rotational coordinates are applied (Nikravesh, 1988). The interested reader in the details on the spatial formulation for kinematic and dynamic analysis of general multibody systems is referred to the work by Nikravesh (1988).

6.2   Geometric modeling of contacting surfaces

The efficiency of a contact detection process relies upon the geometric description of the contact surfaces, which can be represented by means of polygonal or non-polygonal models (Ericson, 2005). Polygonal models are frequently applied to model complex shapes. Nonetheless, when the contact detection method demands a continuous representation, non-polygonal models are utilized. The non-polygonal models can be classified into three main groups, namely constructive solid geometry (CSG), implicit methods and parametric functions.

The use of CSG models is easy and straightforward, but it is restricted because the CSG representations have to be described by a set of Boolean operations instead of a mathematical expression. Regarding the implicit method, a generic 3D surface is represented by an implicit mathematical function that defines the location of the points belonging to a surface, and can be written as

$$f(x, y, z) = 0 \tag{6.9}$$

where x, y and z are the Cartesian coordinates of a generic point located on the surface. By analyzing Equation (6.9), it can be stated that within an implicit function the three Cartesian coordinates are not independent. This is a disadvantage of the implicit method because it does not allow for generating, in a systematic manner, a set of consecutive points located on a surface. Furthermore, efficient rendering and accurate modeling of

sharp edges is usually a hard task whenever implicit representations are utilized (Pauly *et al.*, 2003). Finally, the parametric surface representation can be expressed as

$$\mathbf{s}(u,v) = \begin{cases} x = x(u,v) \\ y = y(u,v) \\ z = z(u,v) \end{cases}$$

(6.10)

in which *x*, *y* and *z* are the Cartesian coordinates of a generic surface point and *u* and *v* denote the corresponding parametric coordinates. In other words, $\mathbf{s}(u,v)$ represents the parametric position vector of a surface. The major advantage of parametric representation is that it allows for the reduction of a three-dimensional problem to the bi-dimensional domain, avoiding the use of complex and timing consuming numerical solutions. Nevertheless, a parametric surface is difficult to ray-trace in the sense that there is no direct and appropriate approach to check if a given point in the 3D-space belongs to a surface. Even so, parametric representations have been broadly utilized in computer-aided design (CAD) for surface modeling purposes. Farin *et al.* (2002) pointed out two main reasons for the wide application of the parametric representations: (*i*) parametric surface patches can be pieced together with any desired degree of continuity and (*ii*) there are many intuitively meaningful techniques for controlling their shape. A comparison between implicit and parametric surface functions is offered in Table 6.1 (Campbell and Flynn, 2001).

Table 6.1   Comparison between the geometrical properties of implicit and parametric surface functions (Campbell and Flynn, 2001).

Property	Implicit Surface	Parametric Surface
General expression	$f(x,y,z)=0$	$\mathbf{s}=f(u,v)$
Accuracy	yes	yes
Intuitive specification	no	yes
Local support	no	yes
Arbitrary topology	yes	no
Guaranteed continuity	yes	yes
Efficient display	no	yes
Efficient intersections	yes	no
Efficient rendering	no	yes

In the present work, parametric functions are used to represent freeform contact surfaces like, for instance, the articular surfaces of the human knee. A freeform surface can be described parametrically by a single patch, such as in the case of a spherical surface, or by an assembly of multiple patches, as for instance those used to define ship

hulls. For contact analysis purposes, it is crucial and desirable to have continuity between adjacent patches (*i.e.*, the patches have to be fitted in such way that their boundaries are imperceptible) in order to ensure numerical stability and computational efficiency to the contact algorithm. From the mathematical point of view, these properties are related to the concept of geometric continuity (G) at different levels, namely positional (G^0), tangential (G^1) and curvature (G^2) (Lai and Ueng, 2001).

In the particular case of parametric surface representation, the derivatives of the surface with respect to the parametric coordinates can be easily studied. This mathematical procedure is usually denominated as parametric continuity. The parametric continuity of first and second levels, C^0 and C^1, can be considered as identical to the positional and tangential continuities. In turn, the third level of parametric continuity, C^2, differs from the curvature continuity in the measure that its parameterization is also continuous (Hohmeyer and Barsky, 1989). In short, the parametric method allows for efficient contact search algorithm for generating and representing arbitrary surfaces which offers great flexibility and precision for handling freeform shapes. It should be highlighted that the implicit and parametric approaches can exhibit complementary characteristics and it may be convenient to convert from one form to another or combined both representations in a hybrid surface model (Pauly *et al.*, 2003). The conversion from parametric to implicit form, known as implicitization, is in general feasible. In turn, the parameterization is not always possible because the class of implicit surfaces is much larger than those of parametric surfaces. The interested reader in the details on the implicit and parametric surface representations is referred to the works by Barr (1981) and Velho *et al.* (2002).

6.2.1 Surface generation and representation

In the parametric method, the points that belong to a surface are given by a collection of mappings, which relate the space parameters to the object surface. As mentioned before, a parametric surface maps a 2D-domain that contains a 3D-space. With the purpose to better understand how the fundamental ingredients necessary to generate and represent a surface by parametric method are handled, consider one eighth of a spherical surface, as shown in Figure 6.3. This surface can be described by a single patch and the spherical polar coordinates can be considered to be the *u* and *v* parameters. The surface radius is denoted by *R*. A surface-fixed coordinate system is

attached at the surface geometric center. The normal, tangent and binormal vectors to the surface at points P_{32}, P_{42}, P_{43} and P_{33} are also depicted in Figure 6.3.

The parametric surface of Figure 6.3 can be expressed as a *u-v* mapping as follows

$$\mathbf{s}(u,v) = \begin{cases} x = R\sqrt{\cos^2 u \cos^2 v} & 0 \le u \le \dfrac{\pi}{2} \quad [\text{rad}] \\ y = R\sqrt{\cos^2 u \sin^2 v} & \\ z = R\sqrt{\sin^2 u} & 0 \le v < \dfrac{\pi}{2} \quad [\text{rad}] \end{cases} \tag{6.11}$$

which allows for the determination of the Cartesian coordinates of the points located on the spherical surface. A dataset with a total of fourteen quantities is necessary to fully characterize each point located on this surface, namely the parametric point coordinates (u, v), the Cartesian coordinates (x, y, z), the Cartesian components of the normal vector $(\mathbf{n}_x, \mathbf{n}_y, \mathbf{n}_z)$, and the Cartesian components of the tangent and binormal vectors ($\mathbf{t}_x^u, \mathbf{t}_y^u,$ $\mathbf{t}_z^u, \mathbf{t}_x^v, \mathbf{t}_y^v, \mathbf{t}_z^v$). This geometric information plays a key role in the contact detection algorithm, because the contact between two generic convex surfaces can be established by solving a set of nonlinear equations that represent the collinear orthogonality between the normal and the distance vectors (Pombo and Ambrósio, 2008).
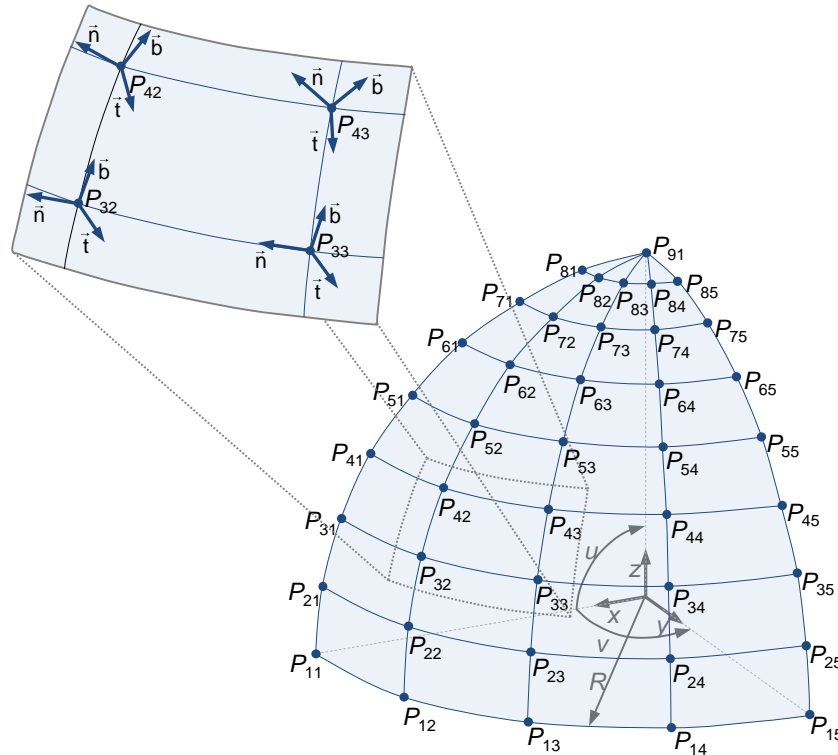

Figure 6.3   Representation of one eighth of a spherical surface using the parametric method.

After describing the contact surface by parametric functions, it is necessary to store this geometric representation into a file. Some of the most common formats of geometry files, such as STEP (standard for the exchange of product), IGES (initial graphics exchange specification) and STL (stereolithography), require large memory size at central processing unit (CPU) for storage. As a result, the reading procedure of these files is memory consuming and, hence, significantly penalizes the computational efficiency of a contact algorithm. This drawback is even more evident in contact analysis that usually requires the computation of normal, tangent and binormal vectors in each instant of simulation. In order to overcome these difficulties and achieve reasonable computation times, a surface preparation is proposed. This is a preprocessing procedure and it can be condensed in the following steps:

1. A regular and representative surface collection of points is extracted from the 3D-parametric surface that has been generated analytically, or modeled in appropriate CAD software. This step is usually denominated as regular surface sampling and is schematically represented in Figure 6.4.

2. For each point surface, the tangent vectors (tangent and binormal) to the u and v directions, and the normal vector are evaluated according to the following mathematical relations

$$\mathbf{t} = \mathbf{t}^u \equiv \mathbf{t}^u(u,v) = \frac{\partial \mathbf{s}(u,v)}{\partial u} \tag{6.12}$$

$$\mathbf{b} = \mathbf{t}^v \equiv \mathbf{t}^v(u,v) = \frac{\partial \mathbf{s}(u,v)}{\partial v} \tag{6.13}$$

$$\mathbf{n} \equiv \mathbf{n}(u,v) = \frac{\tilde{\mathbf{t}}^u \mathbf{t}^v}{\left\| \tilde{\mathbf{t}}^u \mathbf{t}^v \right\|} \tag{6.14}$$

where the tilde (~) placed over a vector indicates that the components of the vector are used to generate the skew-symmetric matrix (Nikravesh, 1988).

3. Once the regular 3D-points surface collection has been established, the geometric information on each point is saved in the form of a lookup table organized as Table 6.2 shows. This lookup table is composed by fourteen columns, being the number of rows equal to the number of points utilized to represent the surface. The information considered here includes the

parametric point coordinates, the corresponding Cartesian coordinates and the Cartesian components of the normal, tangent and binormal vectors. It is important to note that extra columns can be easily added to the lookup table to include, for instance, local geometric and material properties necessary to the evaluation of the contact forces, such as the curvature radius, the generalized stiffness and the coefficient of restitution.

4. The last step of the surface preparation, named lookup table reshuffle, deals with the rearrangement of the lookup table in which the *u-v* mapping is transformed into a 3D-matrix form, as depicted in Figure 6.5. In this process, the surface data is split in equal-sized record elements and saved as a direct access file. In contrast to the sequential file, the direct file permits to read the surface information in any order, which is quite convenient for contact point searching. It is worth noting that line and record are the reading units of the sequential and direct access files, respectively.
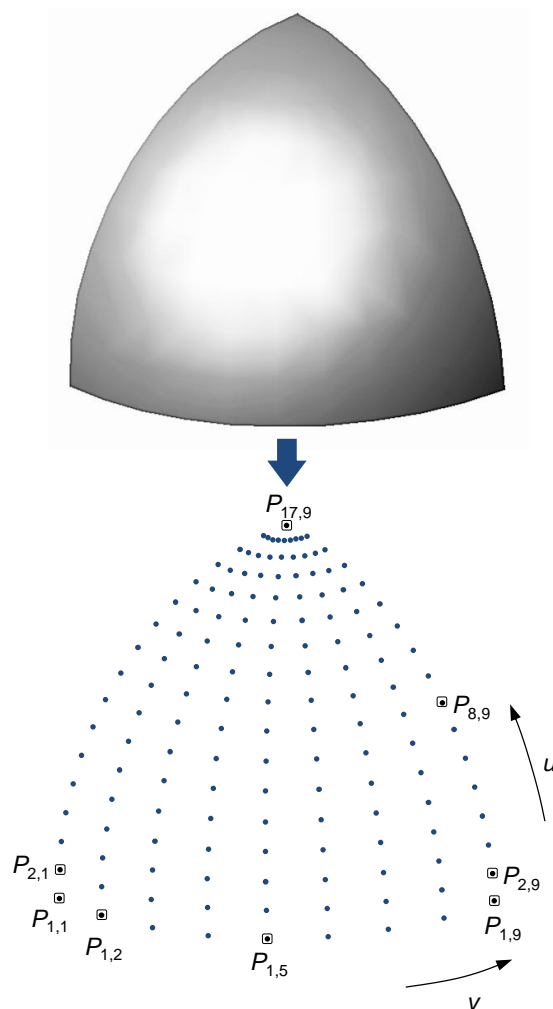

Figure 6.4 Schematic representation of the regular surface sampling.

Table 6.2 Lookup table of the surface represented in Figure 6.4, which contains geometric data relative to the 3D-point sample extracted from the surface, namely parametric coordinates (u, v), Cartesian coordinates (x, y, z), Cartesian components of normal vector (n_x, n_y, n_z), Cartesian components of tangent vector (t_x, t_y, t_z), Cartesian components of binormal vector (b_x, b_y, b_z). This lookup table is presented in its sequential access form and the listed points are the ones bordered by a square in Figure 6.4.

| $P_{i,j}$	u	v	x	Y	z	n_x	n_y	n_z	t_x	t_y	t_z	b_x	b_y	b_z
$P_{1,1}$	0.000	-3.142	-0.006	0.000	0.000	1.000	0.000	0.000	0.000	0.907	0.421	0.000	0.421	-0.907
$P_{2,1}$	0.098	-3.142	-0.006	0.000	0.001	0.995	0.000	-0.098	0.000	1.000	0.000	-0.098	0.000	-0.995
(...)	(...)	(...)	(...)	(...)	(...)	(...)	(...)	(...)	(...)	(...)	(...)	(...)	(...)	(...)
$P_{1,2}$	0.000	-2.945	-0.006	-0.001	0.000	0.981	0.195	0.000	0.195	-0.981	0.000	0.000	0.000	1.000
(...)	(...)	(...)	(...)	(...)	(...)	(...)	(...)	(...)	(...)	(...)	(...)	(...)	(...)	(...)
$P_{1,5}$	0.000	-2.356	-0.004	-0.004	0.000	0.707	0.707	0.000	0.707	-0.707	0.000	0.000	0.000	1.000
(...)	(...)	(...)	(...)	(...)	(...)	(...)	(...)	(...)	(...)	(...)	(...)	(...)	(...)	(...)
$P_{1,9}$	0.000	-1.571	0.000	-0.006	0.000	0.000	1.000	0.000	1.000	0.000	0.000	0.000	0.000	1.000
$P_{2,9}$	0.098	-1.571	0.000	-0.006	0.001	0.000	0.995	-0.098	0.995	0.010	0.098	-0.098	0.098	0.990
(...)	(...)	(...)	(...)	(...)	(...)	(...)	(...)	(...)	(...)	(...)	(...)	(...)	(...)	(...)
$P_{8,9}$	0.687	-1.571	0.000	-0.005	0.004	0.000	0.773	-0.634	0.773	0.402	0.490	-0.634	0.490	0.598
(...)	(...)	(...)	(...)	(...)	(...)	(...)	(...)	(...)	(...)	(...)	(...)	(...)	(...)	(...)
$P_{17,9}$	1.571	-1.571	0.000	0.000	0.006	0.000	0.000	-1.000	0.000	1.000	0.000	-1.000	0.000	0.000
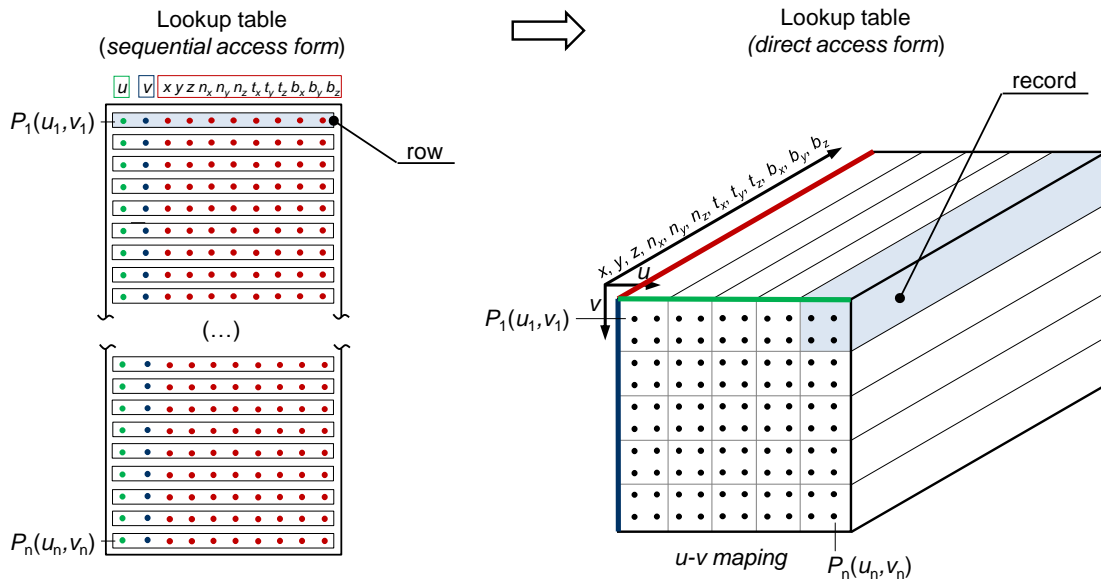
Figure 6.5 Schematic representation of the lookup table reshuffle of a surface defined with 100 points that is stored in 25 equal-sized records.

In short, the proposed methodology to generate and represent a freeform surface is quite straightforward and simple to implement in any general-purpose multibody code. Moreover, the way how the surface data is organized and stored in the preprocessing scheme allows for reading partially the surface data, *i.e.*, only the surface data correspondent to the contact region is read and stored in CPU memory. This surface portion is named storage window and is discussed in detail in Section 6.3. It is worth mentioning that density of the points considered during sampling is arbitrary and, therefore, a user-decision based on the geometry that is being represented.

6.2.2 Knee contact geometries

The knee joint presents a complex shape that involves the distal femur, the proximal tibia and the patella. The distal femur comprises two large and asymmetric convex surfaces named femoral condyles. The proximal tibia has two tibial plateaus, distinct in shape and in conformality. The medial plateau is nearly flat, while the lateral side is convex. For sake of simplicity, several authors modeled the femoral condyles as spheres and fit the tibial plateaus to planes (Abdel-Rahman and Hefzy, 1998; Martelli *et al.*, 2006; Koo and Andriacchi, 2007). This assumption is adopted in this work with the intention to validate the proposed contact methodology. The medial and femoral condyles were modeled as spheres with radius equal to 21 mm and 20 mm, respectively. In turn, the tibial plateaus were fitted to square planar surfaces with area equal to 5535.36 mm^2. The femoral contact surfaces were represented using Equation (6.11), while the tibial contact surfaces were described using a parametric function as follows

$$\mathbf{s}(u,v) = \begin{cases} x = u \\ y = v \\ z = 0 \end{cases} \quad \begin{array}{l} 0 \le u \le x_{max} \quad [\text{m}] \\ 0 \le v \le y_{max} \quad [\text{m}] \end{array} \tag{6.15}$$

where x_{max} and y_{max} are the edge size of the plane on the x and y directions, respectively. Figure 6.6 shows a schematic representation of the knee contact surfaces, namely the spherical femoral condyles and the planar tibial plateaus. It is important to mention that the geometric data used to describe these contact surfaces (radii and edge size) were adapted from the work done by Abdel-Rahman and Hefzy (1998), who also modeled the tibiofemoral joint as a sphere-plane contact system.

After the geometrical description of the contact surfaces using parametric functions, the pre-processing task is initiated. Firstly, a regular and representative collection of points is extracted from each surface of 110889 points (333 points in u-direction and 333 points in v-direction). Then, for each collected point, the tangent vectors to the u and v directions, and the normal vector are computed. In third place, the geometric data relevant for the contact detection process, this is, parametric point-coordinates, Cartesian point-coordinates, normal vector, tangent vector and binormal vector, is stored into the lookup table. Finally, the u-v mapping form of the lookup table is rearranged into a 3D-matrix, being the lookup table saved as a direct access file (Metcalf and Reid, 1999).
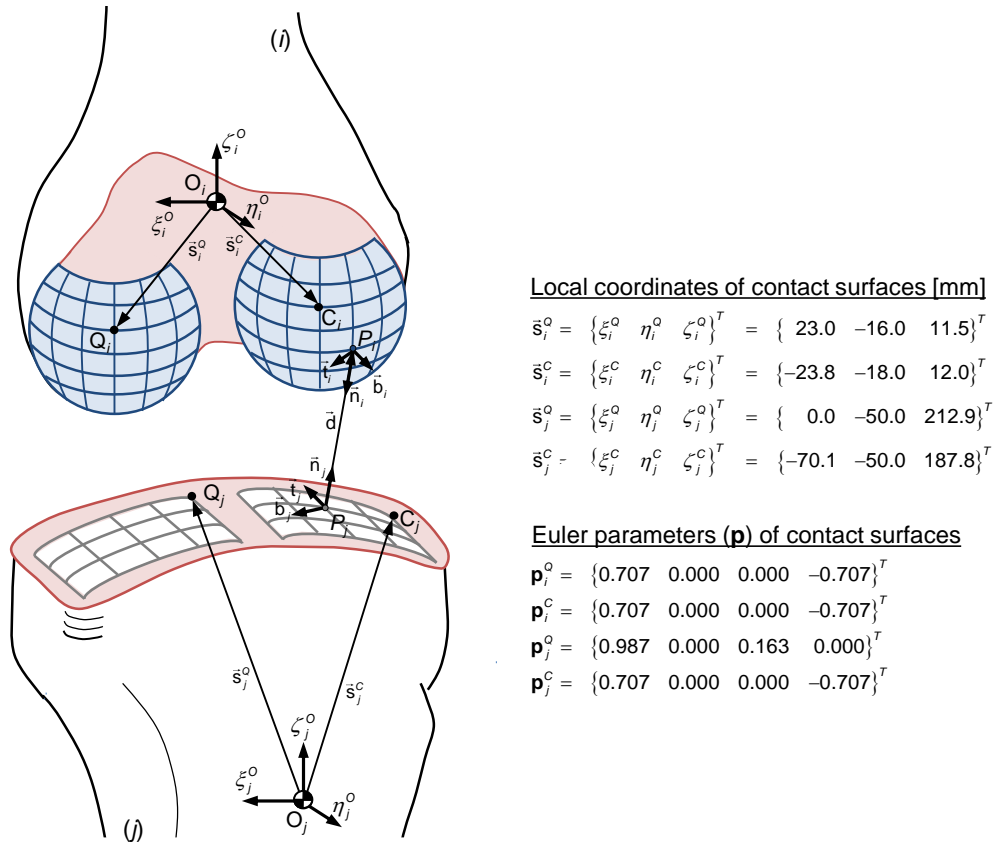
Local coordinates of contact surfaces [mm]

$$\vec{s}_i^Q = \{\xi_i^Q \quad \eta_i^Q \quad \zeta_i^Q\}^T = \{ \ 23.0 \ \ -16.0 \ \ 11.5\}^T$$

$$\vec{s}_i^C = \{\xi_i^C \quad \eta_i^C \quad \zeta_i^C\}^T = \{-23.8 \ \ -18.0 \ \ 12.0\}^T$$

$$\vec{s}_j^Q = \{\xi_j^Q \quad \eta_j^Q \quad \zeta_j^Q\}^T = \{ \ \ 0.0 \ \ -50.0 \ \ 212.9\}^T$$

$$\vec{s}_j^C = \{\xi_j^C \quad \eta_j^C \quad \zeta_j^C\}^T = \{-70.1 \ \ -50.0 \ \ 187.8\}^T$$

Euler parameters (p) of contact surfaces

$$\mathbf{p}_i^Q = \{0.707 \ \ 0.000 \ \ 0.000 \ \ -0.707\}^T$$

$$\mathbf{p}_i^C = \{0.707 \ \ 0.000 \ \ 0.000 \ \ -0.707\}^T$$

$$\mathbf{p}_j^Q = \{0.987 \ \ 0.000 \ \ 0.163 \ \ 0.000\}^T$$

$$\mathbf{p}_j^C = \{0.707 \ \ 0.000 \ \ 0.000 \ \ -0.707\}^T$$

Figure 6.6 Representation of the contact surfaces and ligaments included within the 3D-knee model.

In this work, spheres and planes are employed to define the geometry of the knee articular surfaces. Nonetheless, sophisticated CAD models can be used within the proposed contact methodology as long they have been modeled with parametric functions. Figure 6.7 shows examples of CAD models of natural and artificial knees that have been represented by non-uniform rational B-splines (NURBS) surfaces. The modeling procedure of these CAD models can be summarized in four general steps: (*i*) image data acquisition, such as magnetic resonance imaging (MRI) and computer tomography (CT) scan data from a subject and laser scans from the implants; (*ii*) image segmentation using an image processing software, for instance the sliceOmatic™ (Tomovision, Montreal, Canada); (*iii*) conversion of MRI and CT point cloud data into polygonal models using a reverse engineering software, such as Geomagic Studio® (Geomagic, Inc., Durham, NC); (*iv*) fit the polygonal models into parametric surfaces (e.g. NURBS surfaces) using a surface modeling software, for instance Rhinoceros® (Robert McNeel & Associates, Seattle, WA). In the case of artificial knee models, it is normally required to align the bone surface with the implant, which can be performed in Geomagic Studio® (Geomagic, Inc., Durham, NC). Then, the procedure of transforming the CAD models into a lookup table as direct access file is identical to the described for the sphere and the plane (Bei and Fregly, 2004; Fregly *et al.*, 2012).
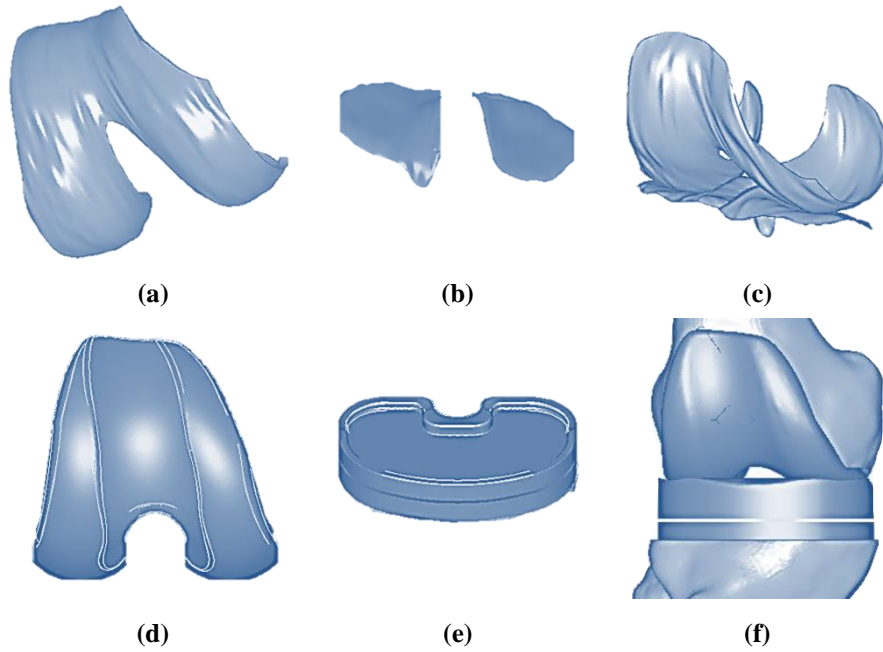
Figure 6.7   Examples of CAD models of knee contact surfaces: (a) femoral articular cartilage; (b) tibial articular cartilage; (c) tibiofemoral articular cartilage; (d) femoral component; (e) tibial insert; (f) tibiofemoral artificial joint (Fregly *et al.*, 2012).

6.3   Methodology for contact detection

A general methodology to deal with 3D-impact problems within multibody systems is described, giving a special attention to the detection and location of the contact point. The key task of a contact methodology is to check whether a potential contact pair of points is in contact or not. When the contact surfaces include simple and regular geometries, such as planes, spheres or cylinders, the actual contact pair of points can be determined analytically (Tian *et al.*, 2011). Nonetheless, when the contact surfaces present complex shapes, a more sophisticated numerical procedure to determine the contact pair of points is required (Bei and Fregly, 2004).

In what follows, a straightforward formulation for the contact detection of generalized surfaces is presented. For this purpose, let consider two moving surfaces belonging to bodies i and j that move with absolute velocities $\dot{\mathbf{r}}_i$ and $\dot{\mathbf{r}}_j$, respectively. Figure 6.8 shows these two moving surfaces, which are represented by means of parametric functions. Both contacting surfaces are assumed to be convex at least in the neighborhood of the potential contact points. The surface parameters u and v are ordered such that the vector **n** becomes the outward normal. The center of mass of bodies i and j are O_i and O_j, while the origin of the surfaces are denoted by Q_i and Q_j. Local coordinate systems $\xi^O\eta^O\zeta^O$ and $\xi^Q\eta^Q\zeta^Q$ are attached at the center of mass of each body and to the origin of each surface, respectively. P_i and P_j represent the potential

contact points. The geometric and positional vectors relevant for the contact detection process are depicted in Figure 6.8.
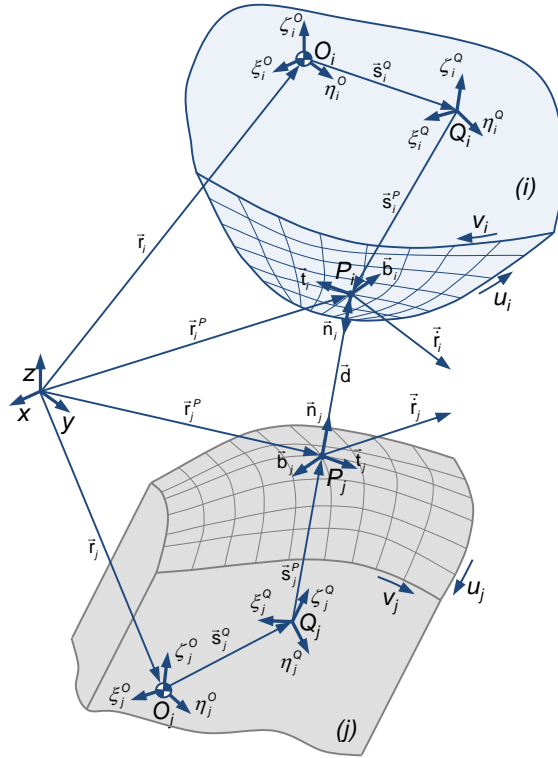

Figure 6.8 Representation of two generalized contact surfaces (Glocker, 1999).

With reference to Figure 6.8, the minimum distance vector **d**, which connects the potential contact points, is calculated as

$$\mathbf{d} = \mathbf{r}_j^P - \mathbf{r}_i^P \tag{6.16}$$

where both $\mathbf{r}_i^P$ and $\mathbf{r}_j^P$ are described in global coordinates with respect to the inertial reference frame (Nikravesh, 1988)

$$\mathbf{r}_k^P = \mathbf{r}_k + \mathbf{A}_k^O (\mathbf{s}_k'^Q + \mathbf{A}_k^Q \mathbf{s}_k''^P), \quad (k=i, j) \tag{6.17}$$

in which $\mathbf{r}_k$ is the global position vector of body k, $\mathbf{s}_k'^Q$ is the local component of Q_k with respect to body reference frame $\xi_k^O \eta_k^O \zeta_k^O$, and $\mathbf{s}_k''^P$ is the local component of P_k with respect to the surface reference frame $\xi_k^Q \eta_k^Q \zeta_k^Q$. The rotational transformation matrices $\mathbf{A}_k^O$ and $\mathbf{A}_k^Q$ ($k = i, j$) are given by Equation (6.3). It is worth mentioning that the transformation matrices $\mathbf{A}_k^O$ ($k = i, j$) vary with the dynamics of the system, while $\mathbf{A}_k^Q$ ($k = i, j$) remain constant because the position of the surface with respect to the

body-reference frame does not change during the analysis. The magnitude of the distance vector is evaluated as

$$\delta = \sqrt{\mathbf{d}^T \mathbf{d}} \tag{6.18}$$

Similarly to the 2D-contact case, the minimum distance condition is not enough to guarantee that a pair of points is effectively the actual contact pair of points. In order to ensure that P_i and P_j are the actual contact points, the surface normal vectors, $\mathbf{n}_i$ and $\mathbf{n}_j$, have to be collinear with the distance vector, $\mathbf{d}$, as Figure 6.8 depicts. These geometric conditions can be expressed by two cross-products between vectors $\mathbf{d}$ and $\mathbf{n}_i$, and $\mathbf{d}$ and $\mathbf{n}_j$. Because the dot products are more convenient for computations, the collinear geometric conditions previously described can be written by a set of dot-products as

$$\mathbf{d} \times \mathbf{n}_i = \mathbf{0} \equiv \begin{cases} \mathbf{d}^T \mathbf{t}_i = 0 \\ \mathbf{d}^T \mathbf{b}_i = 0 \end{cases} \tag{6.19}$$

$$\mathbf{d} \times \mathbf{n}_j = \mathbf{0} \equiv \begin{cases} \mathbf{d}^T \mathbf{t}_j = 0 \\ \mathbf{d}^T \mathbf{b}_j = 0 \end{cases} \tag{6.20}$$

where $\mathbf{t}_k$ and $\mathbf{b}_k$ ($k=i, j$) denote the tangent and binormal vectors illustrated in Figure 6.8. The geometric conditions given by Equations (6.19) and (6.20) constitute four nonlinear equations with four unknowns, *i.e.*, the parametric coordinates u_i, v_i, u_j and v_j. This system of nonlinear equations, which can be solved using an iterative method such as the Newton-Raphson method (Atkinson, 1989), provides the solution for the location of the potential contact points. Once the potential contact points are determined, the next step deals with the evaluation of their relative distance using Equation (6.18). Finally, it is necessary to verify the indentation condition, which ensures that contact exists, *i.e.*, the potential contact points are actual contact points. This conditions is given by

$$\mathbf{d}^T \mathbf{n}_j \leq 0 \tag{6.21}$$

In short, the positions of an actual contact pair of points between two freeform surfaces cannot be predicted *a priori* due to the influence of the kinematic constraints and other interactions on the bodies of the complete system. Therefore, during dynamic simulation the evaluation of the actual contact pair of points requires the resolution of the system of nonlinear equations, given by (6.19) and (6.20). For this purpose, an

initial estimate of the contact points on both surfaces needed to be provided. Then, the information obtained from the previous time step is used as initial guess to find the actual contact point at the current instant of time. With this procedure, only a few iterations are required to achieve the desired solution.

Within the proposed contact approach, the contacting surfaces are described by a set of points that is stored into a lookup table. As a result, geometric data of the actual contact point has to be evaluated whenever this point does not belong to the regular sample of points stored into the lookup table during pre-processing. The geometric data that need to be computed is the data relevant for the contact detection process, that is, Cartesian point-coordinates, normal vector, tangent vector and binormal vector. The evaluation of this geometric data is carried out by means of bilinear interpolation, which is depicted in Figure 6.9 and can be expressed as (Gribbon and Bailey, 2004)

$$
\begin{aligned}
f(u,v) = & \frac{f(u_1,v_1)}{(u_2-u_1)(v_2-v_1)}(u_2-u)(v_2-v) + \frac{f(u_2,v_1)}{(u_2-u_1)(v_2-v_1)}(u-u_1)(v_2-v) + \\
& \frac{f(u_1,v_2)}{(u_2-u_1)(v_2-v_1)}(u_2-u)(v-v_1) + \frac{f(u_2,v_2)}{(u_2-u_1)(v_2-v_1)}(u-u_1)(v-v_1)
\end{aligned}
\tag{6.22}
$$

where u and v are the parametric coordinates of the interpolating point, and $f(u_1,v_1)$, $f(u_2,v_1)$, $f(u_1,v_2)$ and $f(u_2,v_2)$ denote the interpolating functions.
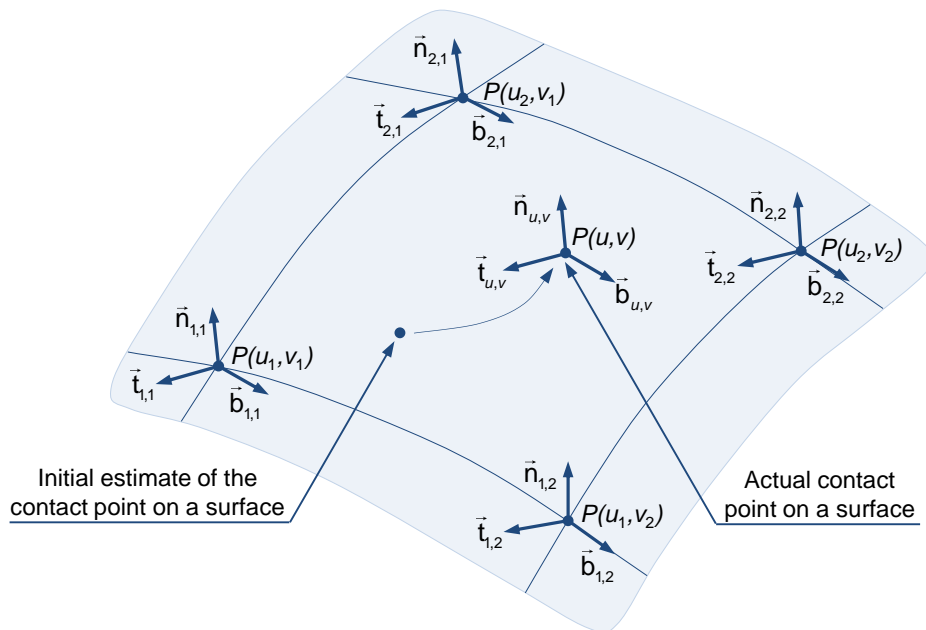
Figure 6.9 Graphical representation of the bilinear interpolation for a surface described by four points.

A total of twelve bilinear interpolations are performed in each instant of simulation in order to evaluate all the relevant geometric information for the contact detection process. Since the bilinear interpolation is an extension of linear case for interpolating functions of two variables on a regular grid, it is considered that this numerical procedure does not penalize the computational efficiency of the proposed contact approach (Gribbon and Bailey, 2004). It is worth mentioning that a more accurate solution for the location of the contact points is achieved when a higher surface discretization is utilized, *i.e.* a higher number of points are used to describe the surfaces.

During the pre-processing, the geometric data of each surface are organized and stored into a direct access file. Within a direct access file, the dataset is organized and divided into equal-sized records, as Figure 6.10 illustrates. Each record is identified by an index number and all records have the same length, which is defined when the file is opened. As the name suggests, the direct access files permit a direct access to a particular record of the file and facilitate the operations of reading, deleting, updating and inserting records into the file. The main differences of a direct access file and a sequential access file are illustrated in Figure 6.10. The direct access files allow for a partial reading of the surface data, *i.e.*, the reading of only a surface portion that includes the potential contact point and some points nearby. This characteristic avoids storing the complete surface data into CPU memory and, hence contributes to the computational efficiency of the proposed contact methodology.
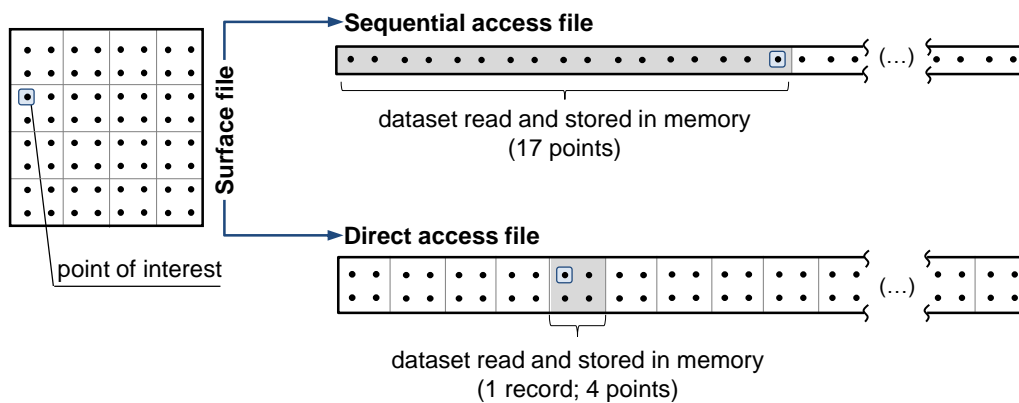

Figure 6.10   Illustration of the main differences between a sequential access file and a direct access file.

Figure 6.11 shows how the dataset of a parametric representation of a contact surface is organized and stored into a direct access file. The point dataset is saved in the record number two and subsequent records. The record number one stores some properties of the surface file, namely the number of point per surface on u-direction

(*u*-Npts), the number of points per surface on *v*-direction (*v*-Npts), the number of point per record on *u*-direction (*u*-pts), the number of points per record on *v*-direction (*v*-pts), the lower bound of surface on *u*-direction (*u*0), the lower bound of surface on *v*-direction (*v*0), the *u*-increment (Δu), the *v*-increment (Δv) and the record length (l_{record}). The record length l_{record} is given by

$$l_{record} = n_{pr} \times n_d \times n_{bit} \tag{6.23}$$

where n_{pr} is the number of points per record (*i.e.*, *u*-points × *v*-points), n_d is equal to 14 that corresponds to the number of surface data associated with a point that is stored into the lookup table, and n_{bit} is assigned to 8 and is associated with the memory space required to store each value (datum size).
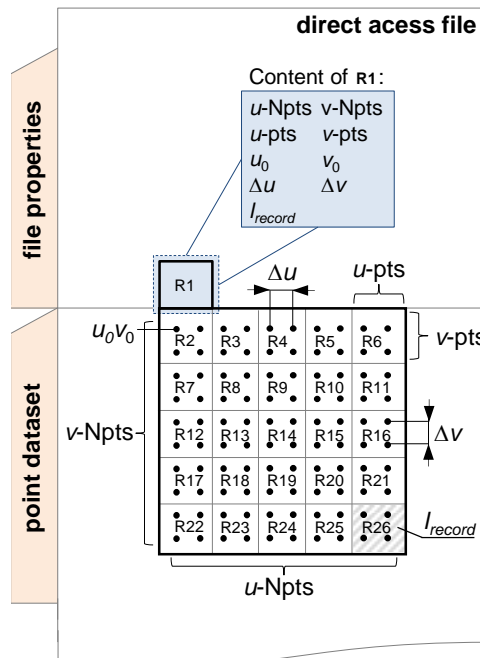
Figure 6.11 Structure of a direct access file of a parametric representation of a surface with 100 points.

The partial reading of a surface file is suitable for contact point searching, in particular when the surface file is very large. In these cases, the storage window must be located at the potential contact zone, that is, it should contain the records to which the potential contact points belong. Figure 6.12a shows one eighth of a spherical surface, previously illustrated in Figure 6.3, with a storage window that includes the contact point at the instant of time *t*. If at the next instant of time, *t*+Δt, the contact point remains in a region close to the previous contact point, the storage window does not need to be updated. In contrast, when the next contact point is distant from the previous contact point, the storage window has to be updated, as Figure 6.12b depicts.
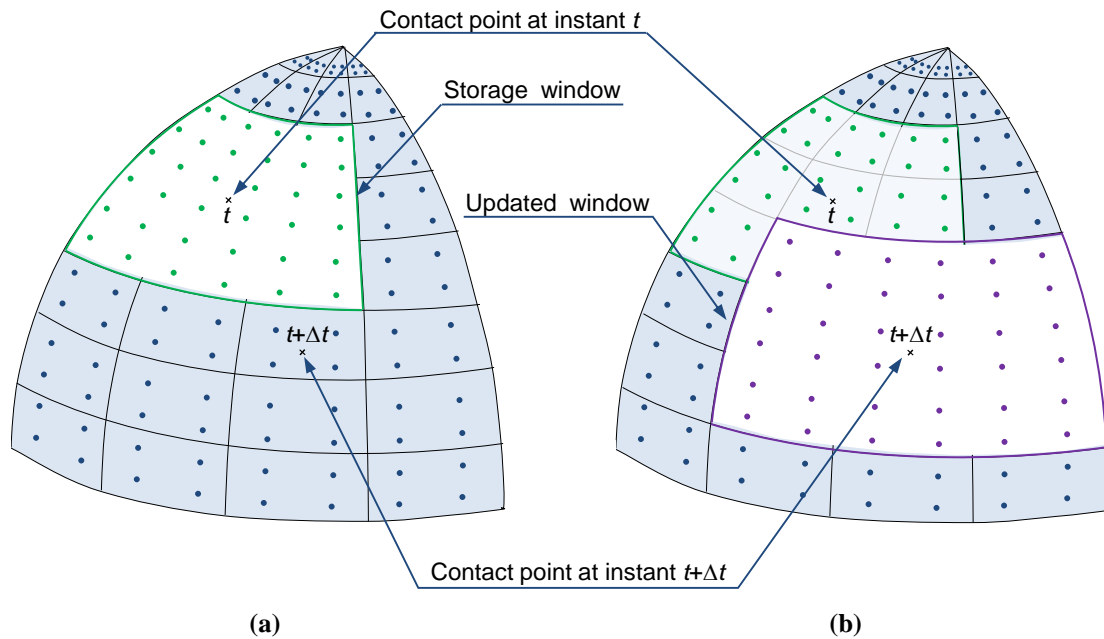
Figure 6.12   Schematic representation of an update of a storage window.

The necessity for updating the storage window is checked in each contact calculation. This process can be summarized and condensed by the following steps:

1. Locate contact record, *i.e.*, the record that contains the initial guess (u_0, v_0);
2. Check if contact record belongs to storage window. If not, go to step (4);
3. Check if contact record is a border record. If not, go to step (7);
4. Locate storage window considering the contact record the center of the new storage window;
5. Store the index of the records of the new storage window, namely the first record and the border records;
6. Read and store the data of the records that belong to the new window;
7. Proceed with the contact computation.

With the purpose to better understand the advantages of the proposed approach, let take a closer look at the surface represented in Figure 6.13. During the first eight impacts, the storage window does not need to be updated, because the contact record belongs to the storage window and is not a border record. In the ninth impact, the contact record still belongs to the storage window, but is now a border record. As a result, the storage window is updated for the next instant of contact, considering the current contact record as center record of the new window. After that, the contact calculations proceed for at least more three impacts without needing a window update.
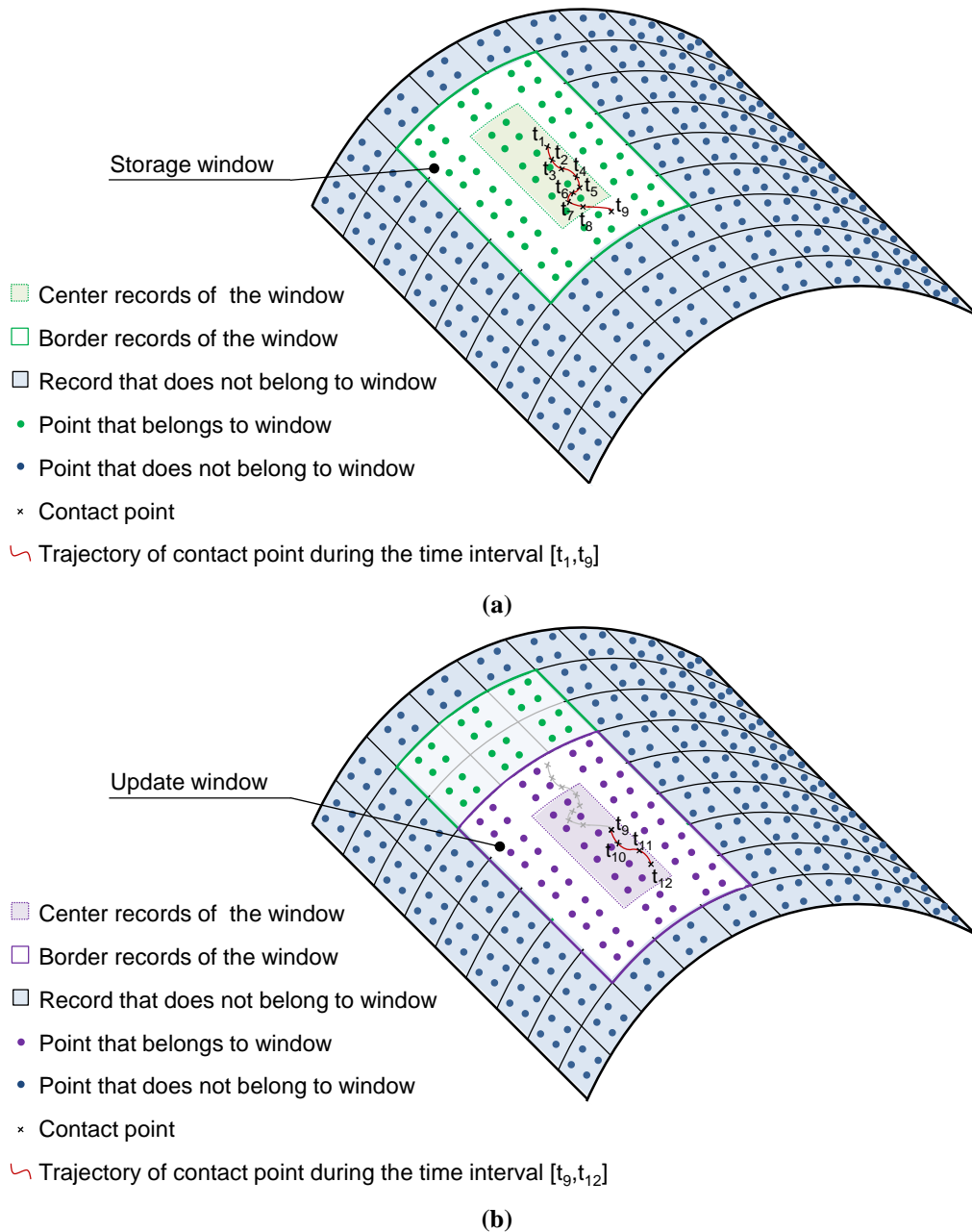
Storage window

☐ Center records of the window
☐ Border records of the window
☐ Record that does not belong to window
• Point that belongs to window
• Point that does not belong to window
× Contact point
↳ Trajectory of contact point during the time interval [t_1,t_9]

(a)

Update window

☐ Center records of the window
☐ Border records of the window
☐ Record that does not belong to window
• Point that belongs to window
• Point that does not belong to window
× Contact point
↳ Trajectory of contact point during the time interval [t_9,t_{12}]

(b)

Figure 6.13   Schematic representation of a contact surface with a storage window: (a) Eight impacts without needing a window update; (b) Update of the storage window in the ninth impact.

The possibility to read partially the surface is useful in the cases where the contact point moves slightly and smoothly and, therefore, it remains in the vicinity of the previous contact point, as Figure 6.13a shows. Thus, the amount of memory used is significantly reduced and the contact detection process is more efficient. The presented methodology is recommended for analyzing continuous contact scenarios that are characterized by smooth variations in the location of the contact points, because it implies only a limited number of window updating operations.

6.4   Computational algorithm for contact in multibody dynamics

As presented in Chapter 3, the equations of motion for a dynamic multibody system can be written in the Hessenberg matrix form as (Nikravesh, 1988)

$$\begin{bmatrix} \mathbf{M} & \mathbf{\Phi}_\mathbf{q}^T \\ \mathbf{\Phi}_\mathbf{q} & \mathbf{0} \end{bmatrix} \begin{Bmatrix} \ddot{\mathbf{q}} \\ \lambda \end{Bmatrix} = \begin{Bmatrix} \mathbf{g} \\ \gamma \end{Bmatrix} \tag{6.24}$$

where $\mathbf{M}$ is the system mass matrix, $\mathbf{\Phi}_\mathbf{q}$ is the Jacobian matrix of the constraint equations, the vector $\ddot{\mathbf{q}}$ contains the generalized state accelerations, λ is the vector that contains the Lagrange multipliers, $\mathbf{g}$ is the vector of generalized forces that contains all external forces and moments applied on the system (including contact forces) and γ is the vector of quadratic velocity terms that is used to describe Coriolis and centrifugal terms in the acceleration equations (Nikravesh, 1988).

During a dynamic simulation of a multibody system, when a contact event is detected, the force produced at the contact interface has to be computed. For this purpose, a continuous contact force (such as Hertz contact law) is utilized, being the normal contact forces evaluated as a function of the relative indentation between the two contacting bodies. Then, the contact forces, together with other applied forces, are introduced into the system of equations of motion as generalized forces.

Figure 6.14 presents the flowchart of the computational algorithm of multibody approach proposed here for analysis of contact problems with 3D-freeform surfaces. This computational algorithm can be summarized and condensed by the following steps:

1. Run the pre-processing unit, which corresponds to the surface generation and preparation described in Section 6.2.1.
2. Set the initial conditions of the system: initial time t^0, initial positions $\mathbf{q}^0$, initial velocities $\dot{\mathbf{q}}^0$, storage window dimensions and initial guesses for surface contact point $u_i^0, v_i^0, u_j^0, v_j^0$.
3. Load window: read and store surface data.
4. Check if the surface point $u_i^0, v_i^0, u_j^0, v_j^0$ belongs to the lookup table; if it does not belong, a bilinear interpolation is performed to determine its geometric properties.

5. Solve the system of nonlinear equations (6.19) and (6.20) that expresses the geometric conditions that a surface point has to fulfill to be considered a potential contact point.

6. Store the parametric coordinates of the potential contact points $(u_i^t, v_i^t, u_j^t, v_j^t)$ as initial guesses $(u_i^0, v_i^0, u_j^0, v_j^0)$ of the next time step.

7. Evaluate indentation condition (6.21) and check for contact; if there is contact, evaluate contact forces using a continuous contact force law.

8. Add contact forces to the vector of generalized forces.

9. Apply a multibody formulation in order to obtain the new generalized positions and velocities of the system for time step $t+\Delta t$.

10. Increment the system time variable.

11. Check if the storage window needs to be updated. If so, go to step (3).

12. Go to step (4) and proceed with the whole process for the new time step, until the final time of the analysis is reached.
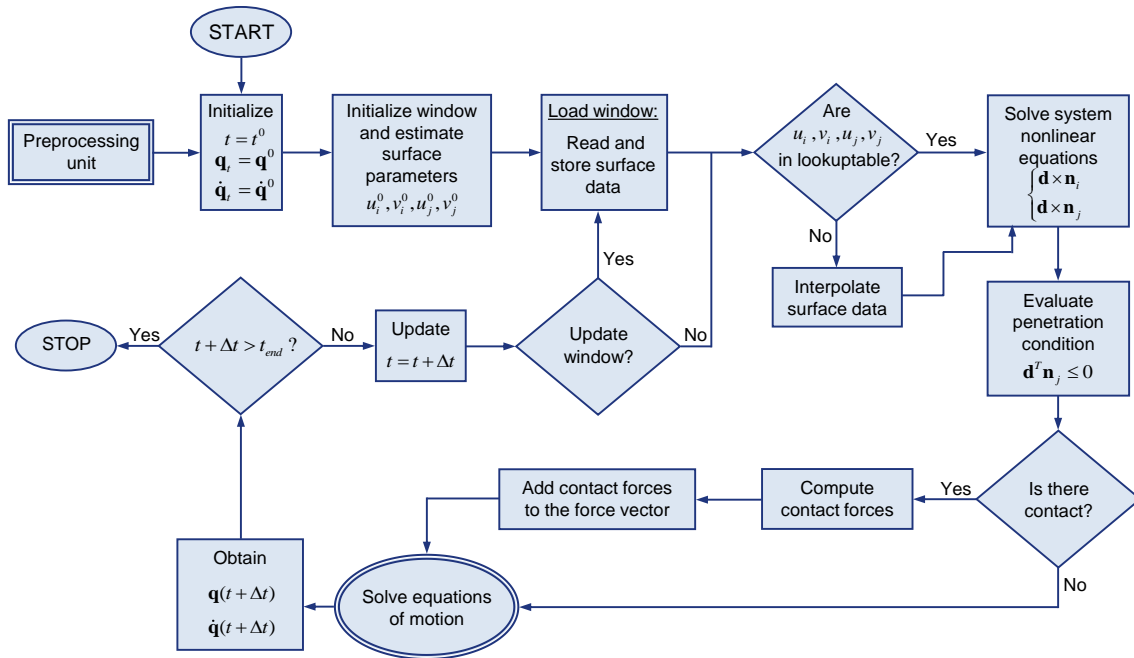
Figure 6.14 Algorithm proposed to deal with 3D-contact problems in multibody systems.

6.5 Dynamic simulations of 3D-contact problems

With the intention of validating the presented contact methodology, several computational simulations were performed using a bouncing ball example. The first set of simulations was aimed to assess the accuracy of the contact response of the proposed approach. Following, a study on the influence of the surface discretization on the

contact response was carried out. The advantage of using a storage window in terms of computational efficiency was also investigated by using the bouncing ball model. Finally, the proposed contact approach was utilized to evaluate the dynamic response of the knee joint, which was modeled as a simple sphere-plane system.

6.5.1 Bouncing ball demonstration example

Figure 6.15 shows the bouncing ball model, which consists of a ball with a mass of 0.092 kg, a moment of inertia equal to 1.472×10^{-4} kgm^2, a radius of 20 mm, animated by an initial horizontal velocity of 0.15 m/s and acted upon by gravitational force. The motion of the ball is such that during its falling trajectory it strikes the ground. The ground was modeled as a plane with 200 mm length and 100 mm width.
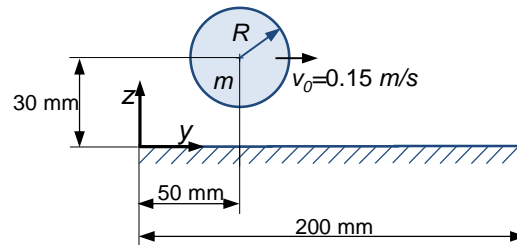
Figure 6.15 Schematic representation of the bouncing ball model.

The contacting surfaces, sphere and plane, are described by a set of points extracted from the corresponding parametric representation, as Figure 6.4 shows. A total of 333 points in u-direction and 333 points in v-direction were considered to represent both contacting surfaces, the sphere and the plane. Regarding the organization of the two data sets, direct access files with a record length of 9072 ($81 \times 14 \times 8$) are used. Therefore, each record includes 81 points.

In these simulations, the Hertz contact law is utilized to evaluate the normal contact forces, being the relative contact stiffness parameter equal to 5.5×10^9 N/m$^{3/2}$. The obtained results were compared with those obtained by using MUBODYNA code (Flores, 2010). Within MUBODYNA code, the sphere is defined by the center point and the radius, while the plane is described by a point and a vector. In contrast, the proposed methodology uses always a set of points extracted from a parametric representation to describe each contact surface independently of its shape. Figure 6.16 depicts the obtained results in both simulations.

By analyzing Figure 6.16, it can be observed that the bouncing ball hits the ground four times in the 0.4 s of simulation, reaching always the same value of maximal indentation because no energy dissipation is accounted in the contact process. As expected, the behavior of the bouncing ball is the same in both approaches. This observation confirms the accuracy of the proposed contact methodology on predicting the dynamic response of multibody systems with 3D contact problems.
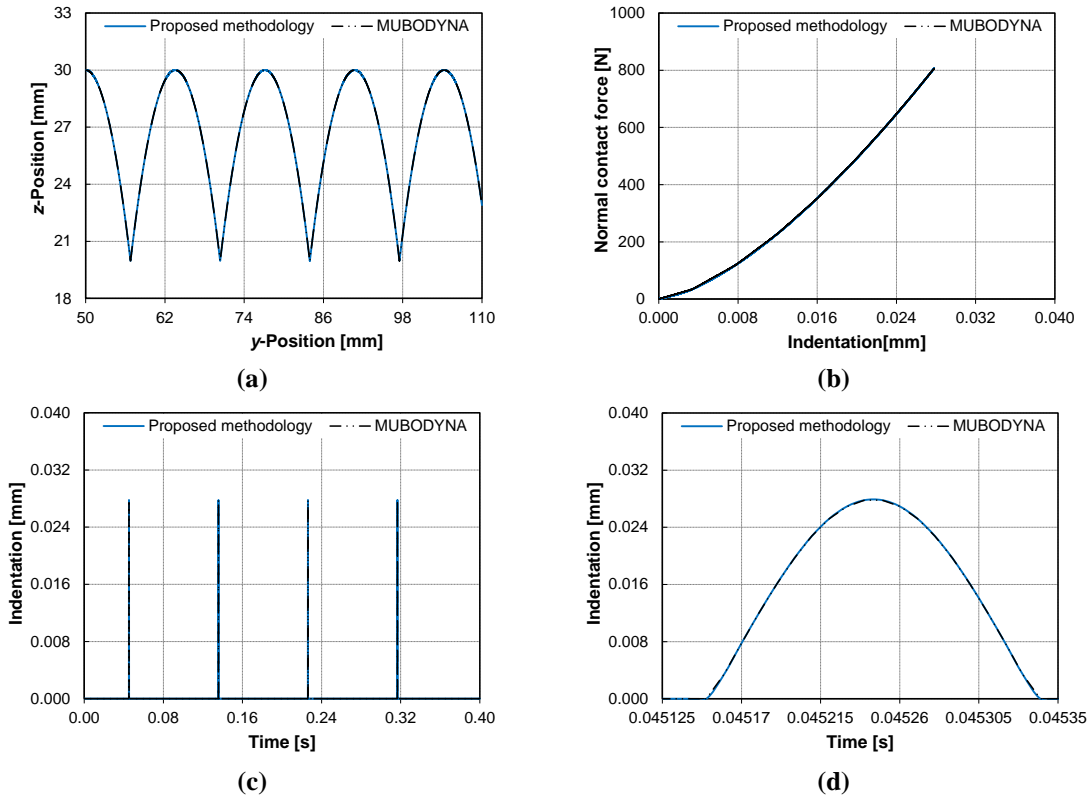

(a)

(b)

(c)

(d)

Figure 6.16 Bouncing ball response using different contact approaches: (a) ball position on *zOy* plane; (b) normal contact force *versus* contact indentation; (c) contact indentation *versus* time; (d) contact indentation *versus* time for the first impact.

In order to study the influence of the level of surface discretization on the contact response of a 3D-multibody system, additional simulations were carried out. Besides the parametric model of the sphere described above and represented by 110889 points (333 points in both directions, *u* and *v*), three other models were considered, namely parametric spheres discretized in (*i*) 81 points (9 points in both directions, *u* and *v*), (*ii*) 1089 points (33 points in both directions, *u* and *v*) and (*iii*) 998001 points (999 points in both directions, *u* and *v*). Figure 6.17 illustrates of these four parametric models.

The dynamic results of computational simulations using different parametric representations for the sphere are plotted in Figure 6.18 where it can be observed that the level of surface discretization does not affect the dynamic response of the bouncing

ball system. Hence, it can be concluded that the level of surface discretization should not be a concern when the contacting surfaces present regular geometries similar to primitive shapes, such as spheres, planes, etc. Regarding contacting surfaces with non-regular shapes, no conclusions can be drawn from this set of simulations. However, a similar study on the influence of the level of surface discretization can be performed whenever complex contact surfaces are used.
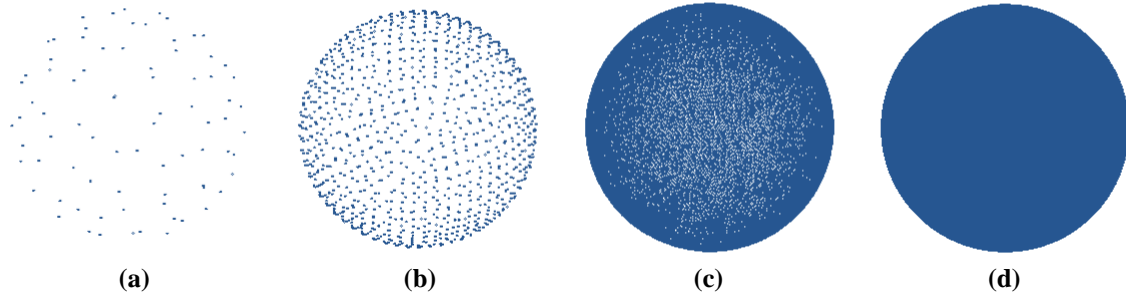

(a)   **(b)**   **(c)**   **(d)**

Figure 6.17 Schematic representation of four models of spheres discretized in: (a) 81 points; (b) 1089 points; (c) 110889 points; (d) 998001 points.
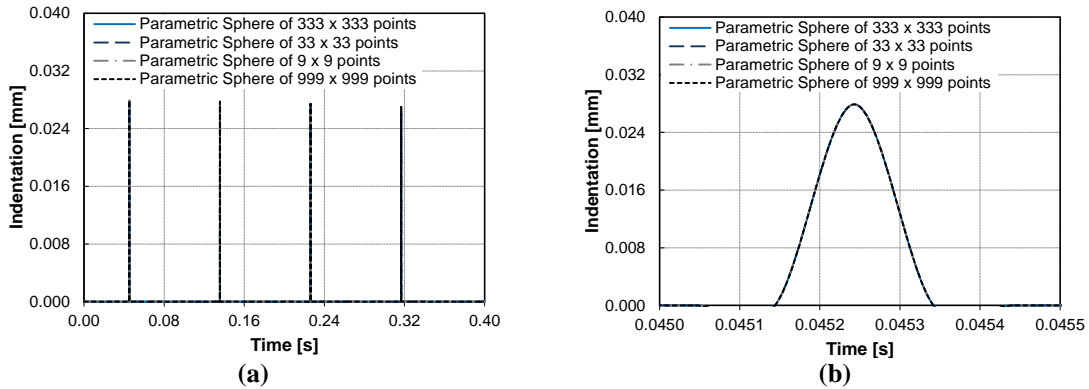
Figure 6.18 Bouncing ball response using different levels of surface discretization: (a) contact indentation for whole simulation; (b) contact indentation for the first impact.
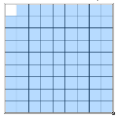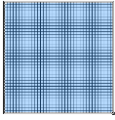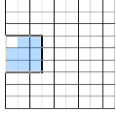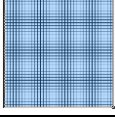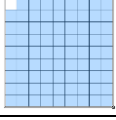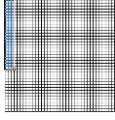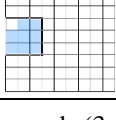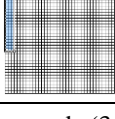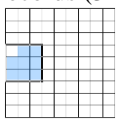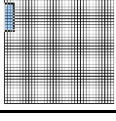
With the intent of checking if the use of a storage window speeds up the simulation, additional set of simulations was performed. Within these simulations, the parametric model of the sphere with the highest level of surface discretization (with 998001 points stored in 81 records) is considered. Storage windows with different sizes were utilized throughout this set of simulations. The size, shape and location of the storage windows used in each simulation are depicted in Table 6.3. The size of a window is indicated in number of records, since the record is the smallest reading unit of a direct access file. It is worth mentioning that a 100 percent storage window corresponds to a storage window that has the same size of the surface file.

In order to evaluate the advantage of using a storage window, a ratio of the obtained CPU times with and without storage window ($ratio_{CPU}$) is calculated by

$$ratio_{CPU} = t_{CPU}^w / t_{CPU} \qquad (6.25)$$

where t_{CPU} and t_{CPU}^w are the computational time consumed without and with storage window, respectively. The computational time consumed to run each simulation together with the $ratio_{CPU}$ are presented in Table 6.3.

Table 6.3 Dimensions of the storage windows and respective t_{CPU}^w and ratio$_{CPU}$.

	Storage window (u_record × v_record)		t_{CPU}^w [s]	ratio$_{CPU}$ (%)
	Sphere (*i*)	Plane (*j*)		
1	81 records (9×9)	1369 records (37×37)	397	100.00
2	9 records (3×3)	1369 records (37×37)	390	98.34
3	81 records (9×9)	69 records (3×23)	369	93.02
4	9 records (3×3)	69 records (3×23)	362	91.20
5	9 records (3×3)	27 records (3×9)	357	89.93

The storage window of the sphere did not need to be updated in either of the five simulations, because the spherical contact point (P_k) is the same for the four impacts ($P_k=\{0,0,-R\}$) and, hence, is located always in the same record.

Regarding the storage window of the plane, the storage window utilized in the fifth simulation (3×9 records) is too small and does not encompass all the records of the contact points of the four impacts. Therefore, an update of this storage window is performed during the fifth simulation. Figure 6.19 illustrates the update of storage window of the contact plane during a bouncing ball simulation.

By analyzing Table 6.3, it can be concluded that the use of a storage window increases the computational efficiency even when an update of the storage window during the simulation is required. The computational time consumed in each simulation is not significantly different. However, small differences can be decisive in long-time simulations. Moreover, the use of the storage window is more appropriate for continuous contact scenarios that are characterized by smooth variations in the location of the contact points, which means that the contact is confined to a small area.
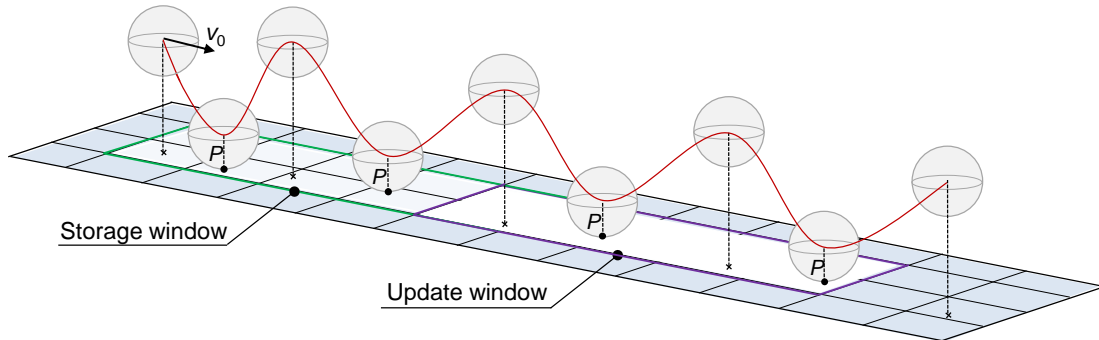

Figure 6.19   Illustration of the update of the storage window during a bouncing ball simulation.

6.5.2   Human knee model demonstration example

A simple 3D-model of the human knee joint is also used to attest the proposed contact methodology. Figure 6.20 illustrates the initial configuration of this biomechanical multibody system, which consists of two bodies i and j that represent the femur and tibia, respectively. Body-fixed coordinate systems $\xi\eta\zeta$ are attached to each body, while *XYZ*-coordinate frame represents the global coordinate system.
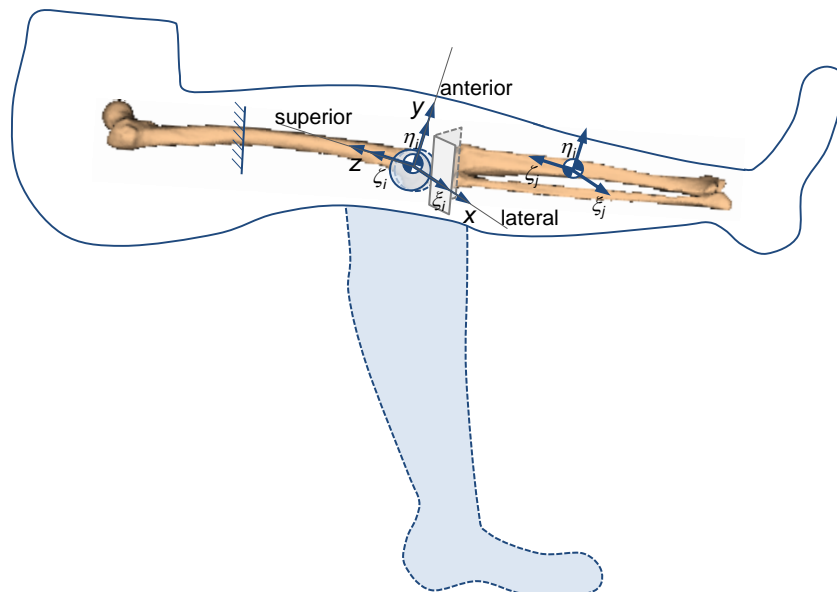

Figure 6.20   Initial configuration of the three-dimensional model of the knee joint.

The femur coordinate system is located at the femoral intercondylar notch and it is coincident with the global reference frame. The tibia coordinate system is located at the center of mass of the tibia, with the local ξ-axis directed laterally, η-axis directed anteriorly and ζ-axis directed superiorly. The coordinates of centers of mass and inertia properties of the bodies are listed in Table 6.4. These properties were derived from literature data of a similar model of a male subject with 76 kg and 1.8 m tall (Yamaguchi, 2001). The femur and tibia are modeled as two free contacting bodies, in which their dynamics is controlled by contact forces, together with ligament and gravitational forces. The equations of motion that govern the dynamic response of this multibody system incorporate these forces. The femur is fixed, while the tibia is considered to move relative to the femur. The tibia is connected to the femur by eight nonlinear springs (Abdel-Rahman and Hefzy, 1998), which represent the main ligament fibers that surround the knee. The local attachment coordinates of the knee ligament, the respective strain at full extension and ligament stiffness are listed in Table 6.5. The ligament fibers included in this knee model are represented in Figure 6.21.
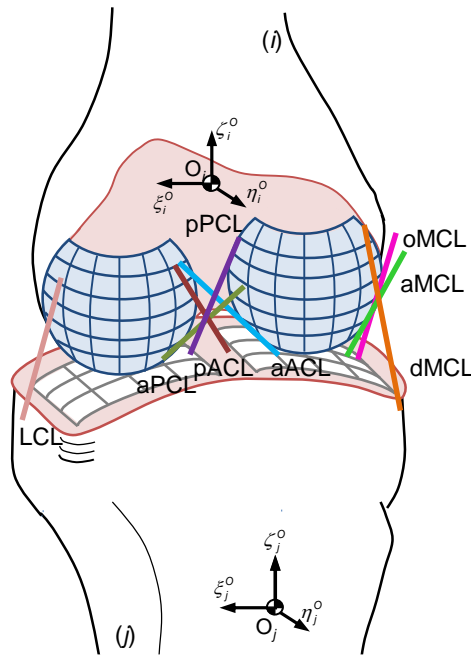

Figure 6.21   Representation of the eight ligament fibers on the knee joint model.

Table 6.4   Global coordinates and inertia properties of the femur and tibia bodies.

Body name	Cartesian coordinates [mm]			Euler parameters			Mass [kg]	Moment of inertia [kg.m^2]		
	x	y	z	e_1	e_2	e_3	m	I_x	I_y	I_z
Femur	0.0	0.0	0.0	0.0	0.0	0.0	11.1836	0.2250	0.2250	0.0462
Tibia	0.0	0.0	-213.5	0.0	0.0	0.0	3.3794	0.0412	0.0432	0.0070

Table 6.5 Local attachment coordinates, strain at full extension and stiffness of the knee ligaments.

Ligament	Femur [mm]			Tibia [mm]			Strain (full extension)	Stiffness [N/mm²]
	ξ_f	η_f	ζ_f	ξ_t	η_t	ζ_t	ε_l	k_l
1. ACL, ant. fibers	7.3	-15.6	21.3	-7.0	5.0	211.3	1.000	83.15
2. ACL, post. fibers	7.3	-20.3	19.6	2.0	2.0	212.3	1.051	83.15
3. PCL, ant. fibers	-4.8	-11.2	14.1	5.0	-30.0	206.3	1.004	125.00
4. PCL, post. fibers	-4.8	-23.2	15.7	-5.0	-30.0	206.3	1.050	60.00
5. MCL, ant. fibers	-34.8	-1.0	26.3	-20.0	4.0	171.3	0.940	91.25
6. MCL, obl. fibers	-34.8	-8.0	24.3	-35.0	-30.0	199.3	1.031	27.86
7. MCL, deep fibers	-34.8	-5.0	21.3	-35.0	0.0	199.3	1.049	21.07
8. LCL	35.3	-15.0	21.3	45.0	-25.0	176.3	1.050	72.22

The acceleration due to gravity is taken as acting on the posterior direction (negative *y*-direction), in order to provide the knee motion from an initial position of knee extension to a final position of knee flexion. The bone portions of the distal femur and proximal tibia are considered as perfectly rigid, due to their higher stiffness when compared to the articular cartilage, which is modeled as a deformable material (Machado *et al*, 2010). The cartilage of the knee is considered to be linear elastic and isotropic with a Young's modulus equal to 24 MPa and a Poisson's ratio equal to 0.38 (Herman, 2007). The coefficient of restitution for the cartilage is set to 0.616 (Burgin and Aspen, 2008). Two sphere-plane contact pairs were considered to represent the medial and lateral contact at the knee joint, as previously described in Section 6.2.2. The location and orientation of each contact surface are depicted in Figure 6.6.

Within the 3D knee model, computational simulations were performed using an integration step equal to 10^{-5} s and the Gear multistep integration method. For sake of simplicity, the Hertz contact law is applied to evaluate the normal contact forces at the medial and lateral compartment of the knee joint. During the simulation, the knee joint flexes by the action of the gravity, which affects the stability of the biomechanical system and promotes the tibia posterior motion. Figure 6.22 shows the contact indentations and forces of each side of the knee along its flexion angle. By observing Figure 6.22, it can be drawn that the first contact occurs at the medial condyle (that has a larger radius), and then jump to the lateral side. Afterwards, femoral and tibial articular surfaces remain in contact during the whole simulation. Note that, a loading phase occurs at the lateral side of the knee whenever an unloading phase occurs at the medial compartment, and vice versa. With the increase of the knee flexion angle, the magnitude of contact forces raises as the system becomes more instable.
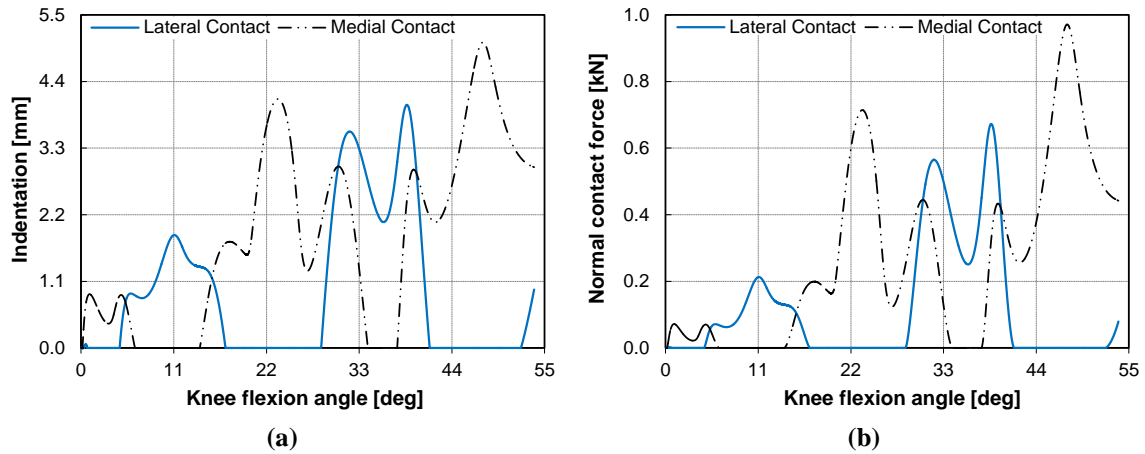
Figure 6.22 Contact response of the 3D-model of the knee joint using the Hertz contact law: (a) indentation *versus* knee flexion angle; (b) normal contact force *versus* knee flexion angle.

Figure 6.23a plots the 3D-trajectory of the center of mass of the tibia along time. The medial and lateral contact points are illustrated in Figure 6.23b at the corresponding femoral surfaces for 9 positions of knee (from 0 to 80 degrees of flexion in intervals of 10 degrees). From Figure 6.23, it can also be observed an internal rotation of the tibia with the increase of the flexion angle. The internal rotation of the tibia was expected, because it is the natural response of this bone segment whenever the knee flects under non-weight bearing conditions (Hamill and Knutzen, 2009). Figure 6.23a shows that the maximal tibia internal rotation, *i.e.* the maximal displacement of the tibia center of mass for the lateral side, is reached when the knee is in 70 degrees of flexion. This outcome is also visible in Figure 6.23, where the highest peak of the lateral contact forces occurs at 70 degrees of flexion. Figure 6.24 shows the dynamic response of the knee ligaments.
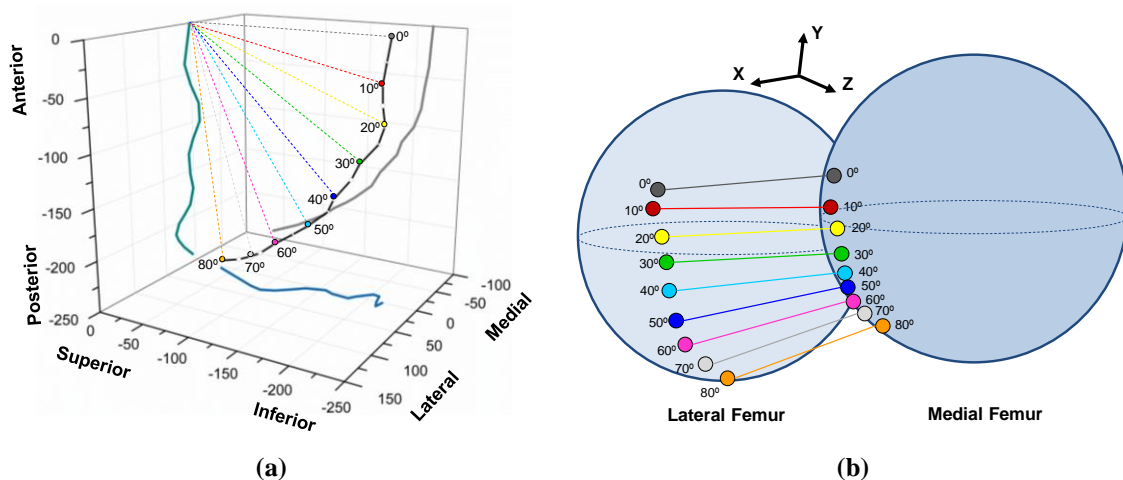

Figure 6.23 Kinematic response of the 3D-model of the knee joint using the Hertz contact law: (a) 3D-Position of tibia center-of-mass (in mm); (b) Femur contact points for 9 different positions of the tibia, namely 0, 10, 20, 30, 40, 50, 60, 70 and 80 degrees of knee flexion.
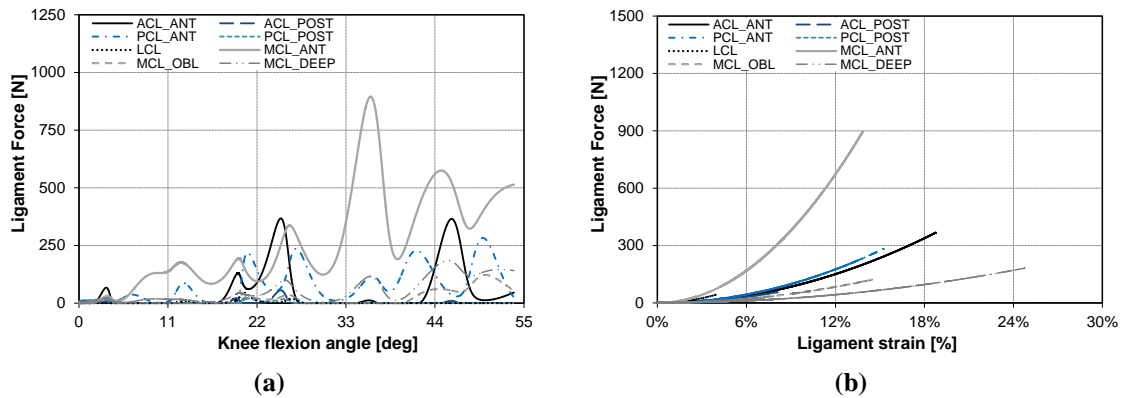
Figure 6.24 Dynamic response of the knee ligaments using the Hertz contact law: (a) Ligament force *versus* knee flexion angle; (b) Ligament force *versus* ligament strain.

The anterior fibers of MCL produce the higher forces, especially when the knee flexion angle is superior to 30 degrees and the knee internal rotation begins. This outcome can be explained by the biomechanical role of the MCL on restraining the internal rotation of the knee joint. PCL (anterior fibers) reports also high ligament forces, which is an acceptable result because PCL limits 95 percent of posterior movement of the tibia. Figure 6.24 shows also that both collateral ligaments are taut in full extension (Hamill and Knutzen, 2009).

6.6   Summary and discussion

With the purpose of predicting the dynamic response of contact at the human knee, a multibody approach to deal with 3D contact problems was presented. This approach includes four main steps: (*i*) surface generation and representation, (*ii*) contact detection, (*iii*) contact forces evaluation and, (*iv*) solution of the dynamic equations of motion.

A generic methodology to generate and represent freeform contact surfaces was introduced. This approach utilizes parametric functions to define the contact geometries, which allow for the reduction of a three-dimensional problem to a bi-dimensional domain and comprises a set of suitable properties for geometric modeling, such as accuracy, local support, guaranteed continuity and efficient rendering. The computational efficiency is of paramount importance on dynamic analysis of multibody system with 3D contact problems. A modeling strategy to reduce the CPU time was outlined. This strategy consisted in developing a preprocessing technique to prepare contact surfaces for dynamic contact simulations. The application of this pre-processor unit allows for reading only the surface portion in the vicinity of the contact area, which was denominated as storage window. This approach avoids the necessity of reading all

surface data to the CPU memory and, hence, speeds up the contact simulations. The storage window is suitable for contact point searching, in particular when the surface file is very large and the contact point moves slightly and smoothly in the same area.

A mathematical formulation for contact detection based on the common-normal concept was presented. This method states that two points in space, belonging to different surfaces, are potential contact points if the normal vectors at these points are collinear to each other and perpendicular to the tangential vectors. This evaluation requires the resolution of a system of nonlinear equations. To check if a pair of points is an actual contact pair, an indentation condition has also to be verified. When contact is detected and a relative indentation greater than zero is reported, a continuous contact force law is applied to evaluate the contact forces.

In order to verify the accuracy and efficiency of the proposed contact approach, three sets of computational simulations were performed using a bouncing ball system as application example. The first set of simulations aimed to check the accuracy of the contact formulation presented on estimating the dynamic response of multibody systems with contact. The obtained results were corroborated by those obtained in MUBODYNA. In second place, the influence of the surface discretization on the contact response of the bouncing-ball system was studied. Within this set of simulations, surfaces with different levels of surface discretization were utilized, being the dynamic behaviors resultant of its application compared. None significant differences were reported, which mean that the level of surface discretization does not affect the dynamic response of the bouncing ball system. This outcome suggests that the level of surface discretization should not be a concern when the contacting surfaces present regular geometries similar to primitive shapes, such as spheres, planes, etc. As far as the contacting surfaces with non-regular shapes are concerned, no conclusions are taken. A third set of simulations was performed in order to check the advantage of using an updatable storage window. The obtained results depict that the use of the storage window speeds up the simulation, even when an update of the storage window is required.

With the intent to study the dynamic behavior of the human knee joint, computational simulations using a simple 3D-model of the knee joint were carried out. This biomechanical model is composed by two contacting bodies, the femur and the tibia, which are connected by eight nonlinear springs that represent some of the ligament fibers that surround the human knee. Two sphere-plane contact pairs were

considered to model the medial and lateral contact at the knee joint, being the contact loads evaluated by using the Hertz contact force law. The dynamic motion considered for simulation was the knee flexion from 0 to 80 degrees of flexion. During this simulation, six articular contacts were detected, three on the lateral side and other three on the medial compartment. The first impact occurs at the medial condyle and then jump to the lateral side. Afterwards, the tibia remains in contact with femur during the whole simulation, or at lateral compartment, or at medial side or at both. An internal rotation of the tibia was also depicted, which is typical of a non-weight bearing situation of knee flexion such as the scenario of the simulation. Regarding the dynamic response of the knee ligaments, the outcomes depicted that the anterior fibers of the MCL produce high forces, especially when the knee internal rotation begins. This can be explained by the biomechanical role of MCL that consists in restraining the internal rotation of the knee joint. Moreover, the anterior fibers of PCL reported also high forces. This result was expected because at the human knee the PCL limits the movement of the tibia in the posterior direction in 95%.

References

Abdel-Rahman, E., Hefzy, M.S. (1998) Three-dimensional dynamic behaviour of the human knee joint under impact loading. *Medical Engineering & Physics*, 20(4), pp. 276-290.

Atkinson, K.A. (1989) *An introduction to numerical analysis*. John Wiley & Sons: New York (NY).

Barr, A.H. (1981) Superquadrics and angle-preserving transformations. *IEEE Computer Graphics and Applications*, 1(1), pp. 11-23.

Bei, Y., Fregly, B.J. (2004) Multibody dynamic simulation of knee contact mechanics. *Medical Engineering & Physics*, 26(9), pp. 777-789.

Burgin, L.V., Aspen, R.M. (2008) Impact testing to determine the mechanical properties of articular cartilage in isolation and on bone. *Journal of Materials Science: Materials in Medicine*, 19(2), pp. 703-711.

Campbell, R.J., Flynn, P.J. (2001) A survey of free-form object representation and recognition techniques. *Computer Vision and Image Understanding*, 81(2), pp. 166-210.

Ericson, C. (2005) *Real-time collision detection*. Morgan Kaufmann Publishers: San Francisco (CA).

Farin, G.E., Hoschek, J., Kim, M.-S. (2002) *Handbook of computer aided geometric design*. North-Holland: Amsterdam, Netherlands.

Flores, P. (2010) *MUBODYNA - A FORTRAN program for dynamic analysis of planar multibody systems*. University of Minho, Guimarães, Portugal.

Fregly, B.J., Besier, T.F., Lloyd, D.G., Delp, S.L., Banks, S.A., Pandy, M.G., D'Lima, D.D. (2012) Grand challenge competition to predict in vivo knee loads. *Journal of Orthopaedic Research*, 30(4), pp. 503-513.

Glocker, C. (1999) Formulation of spatial contact situations in rigid multibody systems. *Computer methods in applied mechanics and engineering*, 177 (3-4), pp. 199-214.

Gribbon, K.T., Bailey, D.G. (2004) A novel approach to real-time bilinear interpolation. *2nd IEEE International Workshop on Electronic Design, Test and Applications*, (pp. 126-131). Perth, Australia.

Hamill, J., Knutzen, K.M. (2009) *Biomechanical Basis of Human Movement*. Lippincott Williams & Wilkins: Philadelphia (PA).

Herman, I.P. (2007) *Physics of the human body*. Springer-Verlag: New York (NY).

Hohmeyer, M.E., Barsky, B.A. (1989) Rational continuity: Parametric, geometric, and Frenet frame continuity of rational curves. *ACM Transactions on Graphics*, 8(4), pp. 335-359.

Koo, S., Andriacchi, T.P. (2007) A comparison of the influence of global functional loads vs. local contact anatomy on articular cartilage thickness at the knee. *Journal of Biomechanics*, 40(13), pp. 2961-2966.

Lai, J-Y., Ueng, W-D. (2001) G2 continuity for multiple surfaces fitting. *The International Journal of Advanced Manufacturing Technology*, 17(8), pp. 575-585.

Lin, Y-C., Haftka, R.T., Queipo, N.V., Fregly, B.J. (2010) Surrogate articular contact models for computationally efficient multibody dynamic simulations. *Medical Engineering & Physics*, 32(6), pp 584-594.

Machado, M., Flores, P., Claro, J.C.P., Ambrósio, J., Silva, M., Completo, A., Lankarani, H.M. (2010) Development of a planar multibody model of the human knee joint. *Nonlinear Dynamics*, 60(3), pp. 459-478.

Martelli, S., Pinskerova, V., Visani, A. (2006) Anatomical investigation on the knee by means of computer-dissection. *Journal of Mechanics in Medicine and Biology*, 6(1), pp. 55-73.

Metcalf, M., Reid, J. (1999) *FORTRAN 90/95 explained*. Oxford University Press: New York (NY).

Nikravesh, P. (1988) *Computer-aided analysis of mechanical systems*. Prentice Hall: Englewood Cliffs (NJ).

Nikravesh, P.E., Chung, I.S. (1982) Application of Euler Parameters to the Dynamic Analysis of Constrained Mechanical Systems. *Journal of Mechanical Design*, 104(4), pp. 785-791.

Pauly, M., Keiser, R., Kobbelt, L.P., Gross M. (2003) Shape modeling with point-sampled geometry. *ACM Transactions on Graphics*, 22(3), pp. 641-650.

Pombo, J., Ambrósio, J. (2008) Application of a wheel-rail contact model to railway dynamics in small radius curved tracks. *Multibody System Dynamics*, 19(1-2), pp. 91-114.

Tian, Q., Liu, C. Machado, M., Flores, P. (2011) A new model for dry and lubricated cylindrical joints with clearance in spatial flexible multibody systems. *Nonlinear Dynamics*, 64(1-2), pp. 25-47.

Velho, L., Gomes, J., Figueiredo, L.H. (2002) *Implicit objects in computer graphics*. Springer-Verlag: New York (NY).

Yamaguchi, G. (2001) *Dynamic modeling of musculoskeletal motion*. Kluwer Academic Publishers: Dordrecht, Netherlands.